Alignment and Imaging of Molecular Complexes Embedded in Helium Nanodroplets

PhD Thesis

James D. Pickering
Department of Chemistry
Aarhus University
September 2018

keep your lamp trimmed and burning

Statistical Analysis

Statistic	Value
Total Pages	188
Total Words	59431
Filesize	28.02 MB
Files in /figures/	1425
Figures in Thesis	60
Cups of Tea Consumed	217
Cups of Coffee Consumed	106
Computer Crashes	17
Computer Crashes Caused by Matlab	15
Computer Crashes Requiring Complete Linux Reinstall	2
Wasps trapped in 1510-411	∼200

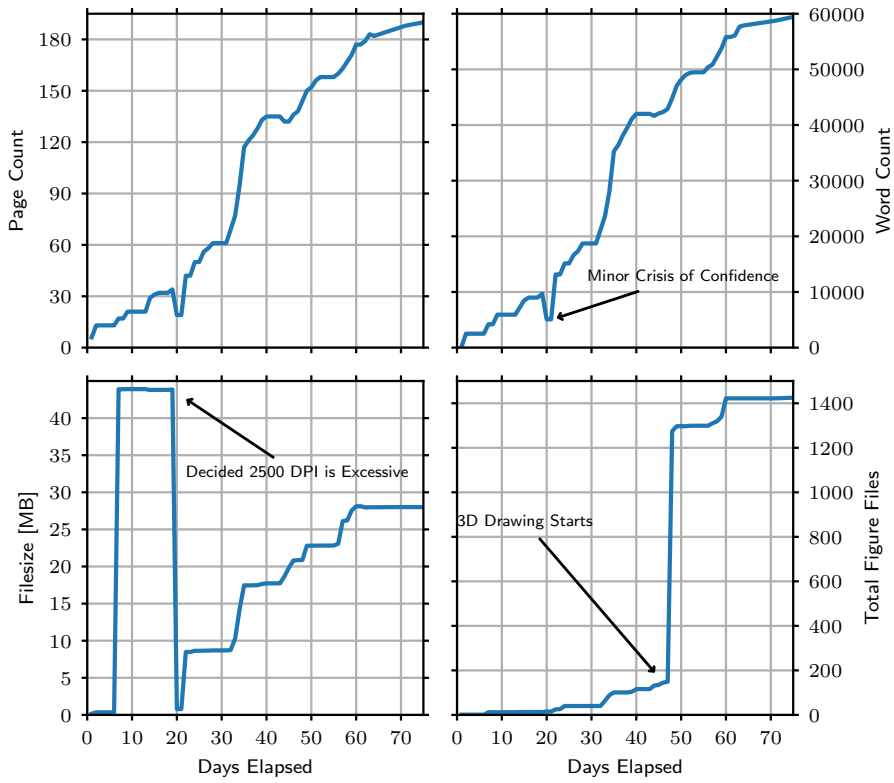

Contents

Contents **iii**
Acknowledgements v
Summary vii
Dansk Resumé viii
Coordinate Conventions xi
Abbreviations xii

1 Introduction **1**

2 Helium Droplets **5**
2.1 Low-Temperature Helium 6
2.2 Superfluid Helium Droplets 8
2.3 Summary 13

3 Molecular Complexes **15**
3.1 Definitions 15
3.2 Studying Molecular Complexes 17
3.3 Summary 25

4 Experimental Techniques **27**
4.1 Laser-Induced Alignment 27
4.2 Coulomb Explosion Imaging 37
4.3 Summary 42

5 Analysis of Ion Imaging Data **43**
5.1 Covariance Analysis 43
5.2 Kinetic Energy Release of Clusters 50
5.3 Projection of Ion Emission Angles 52
5.4 Deconvolution of Non-Axial Recoil 53
5.5 Summary 54

6 Experimental Setup **55**

6.1 Helium Droplet Machine 55
6.2 Laser Systems 64
6.3 Summary 68

7 Structural Imaging of the CS_2 Dimer **71**
7.1 Background 71
7.2 Forming the CS_2 dimer in Helium Droplets 73
7.3 The Structure of $(CS_2)_2$ in Helium Droplets 75
7.4 Imaging the dihedral angle of $(CS_2)_2$ 80
7.5 Summary 88

8 Intensity Dependent Alignment of $(CS_2)_2$ **89**
8.1 Experimental results 89
8.2 Alignment Simulations 92
8.3 Comparison of Simulation and Experiment 96
8.4 Summary 98

9 Alignment and Imaging of OCS Oligomers **99**
9.1 Background 99
9.2 Doping Regimes 100
9.3 OCS Dimer Structure 104
9.4 OCS Trimer Structure 110
9.5 Summary 117

10 Anthracene in Helium Droplets **119**
10.1 Motivations and Background 119
10.2 Experimental Plan 121
10.3 Structural Imaging of $(Anth)_2$ 123
10.4 Photodimerisation of Anthracene 132
10.5 Summary 137

11 Conclusion and Outlook **139**
11.1 Complexes of Small Molecules 139
11.2 Anthracene in Helium Droplets 141
11.3 Outlook 142

A Calibration of the VMI Spectrometer **145**

B Selected Studies of CS_2 Clusters in the Gas Phase **147**
B.1 Background 147
B.2 Results and Discussion 149

Bibliography **157**

Acknowledgements

First and foremost, I would like to thank my supervisor, Henrik Stapelfeldt. Henrik's unrivalled expertise and passion for science made my PhD study wholly enjoyable, and his willingness to engage in scientific discussion meant there was never a shortage of potential avenues to explore. Henrik's door was always open when I wanted to clarify some (often trivial) point, and his good nature means that meetings with him often feel more like a conversation among equals than a meeting of supervisor and students. This made Femtolab a wonderful place to work, and one that has consistently produced excellent science.

Within Femtolab, I would like to thank Lars Christiansen for enabling me to quickly become competent at running the experiments, and for teaching me almost everything I know about optics and lasers. Working with Lars was always fun, despite his awful taste in music. Ben Shepperson also deserves a special mention, as it was me and Ben that undertook almost all of the experiments described in this thesis, and his experience, work ethic, and knowledge of the vacuum systems was second to none. Despite Ben's Stakhanovite work ethic, he was never one to let a trifling experiment get in the way of a trip to the friday bar, and many enjoyable evenings were spent running to the bar from the lab inbetween timescans. I am grateful to both of these men (especially Lars) for proof reading this manuscript.

Elsewhere in Femtolab, Anders Vestergaard Jørgensen, Marlene Møller Madsen, Constant Schouder, Jacqueline Arlt, Mette Heidemann Rasmussen, Anders Aspegren Søndergaard, and Rasmus Ranch Johansen have been great office-mates, and have made the fourth-floor office a pleasant place to work. Outside my office, Adam Chatterley was always a source of insightful discussions at lunch and coffee breaks, and I am grateful to him for proof reading parts of this manuscript. Thanks should also go to Jan Thøgersen, without whom the lab would never function, and his neo-Luddite attitude to emails, smartphones, and the internet does not paint an accurate picture of a man with a world-class knowledge of cutting-edge laser science. Additionally, I would like to thank the many Master's and Bachelor's students we have had over the years for contributing to the enjoyable work atmosphere. Of these students, I would especially like to thank Bjarke Hübschmann and Frederik Thorning, for the stellar work they did in contribution to the CS_2 dimer study.

Outside of Femtolab, I am grateful to the MEDEA network and to Thomas Binhammer and Andy Ellis for allowing me to undertake enjoyable secondments in their labs in Hannover and Leicester. I will especially

remember my time in Leicester, and thank Andy, along with Julia Davies, Martin Mugglestone, Jon Lasham, Leanne Blount, and Tom Beaver for an enjoyable stay there. I am also grateful to Julia and Martin for proof reading parts of this work. I would also like to thank the other MEDEA ESRs, and especially Jan Lahl and Nils Monserud, for making the many meetings and schools so enjoyable. Thanks must also go to Ian MacPhail-Bartley for the weeks he spent here helping with the anthracene experiments, and to Giulio Bertuzzi for helping with the messy wet chemistry involved in the dianthracene synthesis. Frank Jensen also deserves many thanks for the many calculations he has performed for me over the previous three years. As a final work-related acknowledgement, I would like to thank Michael Burt for (almost) four years of top-quality email banter, and for always being on hand whenever I needed to clarify nomenclature. I am especially grateful to Michael for making time to proof read various things over the years I have known him, including many parts of this thesis - and I hope we can continue our work together both over email and in frozen, inaccessible parts of the northern hemisphere.

Aside from work colleagues, I would like to thank my mother, father, and sister - and extended family - for the 25 years of love and encouragement they have given me throughout my education, culminating (in some senses) in the production of this document. I am sure that they are looking forward to my return to the UK (before the borders are all closed), and I will now be able to attend family events again. Finally, I would like to thank Annaliese Deere for her unwavering love and support while I've been writing this thesis, she has made every day worthwhile, and was always ready with encouragement whenever I felt down, despite being almost 900 miles away from me most of the time. My life is enriched with you in it.

Summary

This thesis focuses on generation, manipulation, and characterisation of weakly-bound molecular complexes in superfluid helium nanodroplets. These complexes are created inside the droplets, and are manipulated using laser-induced alignment such that their structures can be elucidated using Coulomb explosion imaging. Importantly, this technique preserves the sub-ps time resolution of the Coulomb explosion process. Prior work in Femtolab has primarily focussed on the manipulation of single molecules in helium droplets, and this thesis represents the first steps towards the study of clusters of molecules.

The majority of the work presented here concerns the study of complexes (n=2,3) of the small triatomic molecules carbon disulphide (CS_2) and carbonyl sulphide (OCS). It is shown that these complexes can be grown inside helium droplets via control of the partial pressure of a specific molecule in the doping cell that the droplet beam passes through. Having established this, it is then shown that it is possible to align these complexes inside helium droplets using an intense, long (160 ps), non-resonant laser field. Coulomb explosion of the aligned complexes then allows their structures to be determined. For CS_2, the structure of the dimer was unambiguously shown to be cross-shaped - in line with previous spectroscopic work. For OCS, the structures of the dimer and trimer were studied, and the dimer was shown to have a slipped-parallel structure (as in the gas-phase), but multiple structures were observed for the trimer. These included a barrel-shaped structure, also observed in the gas phase, and a linear-chain structure, hitherto unobserved in the gas phase. In addition to this, a detailed study of the alignment behaviour of the CS_2 dimer was undertaken.

Having shown that it is possible to form and manipulate these clusters, the first attempts at a more ambitious experiment concerning formation of anthracene dimers was attempted. Anthracene readily photodimerises in UV light to form a covalently-bound dimer, dianthracene. It was shown that it is possible to form anthracene van der Waals dimers, but their structure in helium droplets could not be unambiguously determined using the alignment/imaging technique thus far. It was then shown that the photodimer, dianthracene, could be synthesised on a windowsill and successfully doped into helium droplets, and a dianthracene cation detected. These experiments are ongoing, with the ultimate goal being to perform the photodimerisation in a time-resolved manner inside helium droplets.

Dansk Resumé

Denne afhandling handler om udvikling, manipulering, og karakterisering af svagt-bundne molekylære komplekser inde i superflydende helium nanodråber. Disse komplekser skabes inde i dråberne, og bliver manipuleret med laserinduceret alignment, så deres struktur kan undersøges med Coulombeksplosion imaging. Denne teknik bevarer sub-ps tidsopløsningen af Coulombexplosionen. Tidligere studier i Femtolab fokuserede primært på at studerere af enkelte molekyler opløst i heliumdråber, denne afhandling repræsenterer de første skridt i studiet af molekylære komplekser.

Størstedelen af afhandlingen handler om studiet af komplekser af de små triatomare molekyler carbondisulfid (CS_2) og carbonylsulfid (OCS). Det vises, at disse komplekser kan dannes inde i heliumdråber, via kontrol af damptrykket af molekylerne i dopingcellen, som dråbestrålen passerer igennem. Herefter, vises det at det er muligt at aligne disse komplekser inde i heliumdråberne med en kraftig, 160 ps) lang, ikke-resonant laserpuls. Derved kan strukturen af de alignede molekyler bestemmes. Strukturen af CS_2 dimeren er krydsformet - hvilket er velkendt fra IR spektroskopi. For OCS, blev strukturerne af dimeren og trimeren studieret. Vores målinger viste, at dimeren har en parallel-struktur, hvilket er der samme som dimerer i gas fase, og for trimeren blev flere strukture observeret. Der var en tøndeformet struktur (velkendt i gasfasen), og en lineær-kæde struktur, som ikke er set i gasfasen. Desuden, blev alignment dynamikken af CS_2 dimeren undersøgt.

Med viden om hvordan man kan danne disse komplekser inde i dråberne, blev en mere ambitiøst eksperiment, som handler om antracen dimerer, forsøgt. Under bestråling med UV lys, dimeriserer antracen nemt og danner en fotodimer, diantracen. Det blev vist at det er muligt at danne antracen van der Waals dimer, men strukturerne kunne ikke bestemmes med alignment/imaging teknikken. Dernæst blev det vist, at fotodimeren, diantracen, kunne blive syntetiseret i vindueskarmen ved hjælp af sollys og så opløst i heliumdråber, og moderionen afbilledet. Disse eksperimenter giver håb om, at det vil være muligt at følge fotodimerisation af antracen (og måske andre molekyler) med femtosekund tidsopløsning.

List of Publications

The work presented in this thesis forms the basis of the following publications.

Alignment and Imaging of the CS_2 Dimer inside Helium Nanodroplets.
J. D. Pickering, B. Shepperson, B. A. K. Hübschmann, F. Thorning, and H. Stapelfeldt. March 2018. Physical Review Letters 120, 113202.

Femtosecond Laser-Induced Coulomb Explosion Imaging of Aligned OCS Oligomers inside Helium Nanodroplets.
J. D. Pickering, B. Shepperson, L. Christiansen, and H. Stapelfeldt. Sept 2018. The Journal of Chemical Physics 149. 154306.

Alignment of the CS_2 Dimer Embedded in Helium Droplets Induced by a Circularly Polarized Laser Pulse.
J. D. Pickering, B. Shepperson, L. Christiansen, and H Stapelfeldt. In Prep.

In addition to those mentioned, I have also contributed to the following works during my PhD study.

Gas-phase structural isomer identification by Coulomb explosion of aligned molecules.
M. Burt *et al.* March 2018. The Journal of Chemical Physics 148, 091102.

Coordinate Conventions

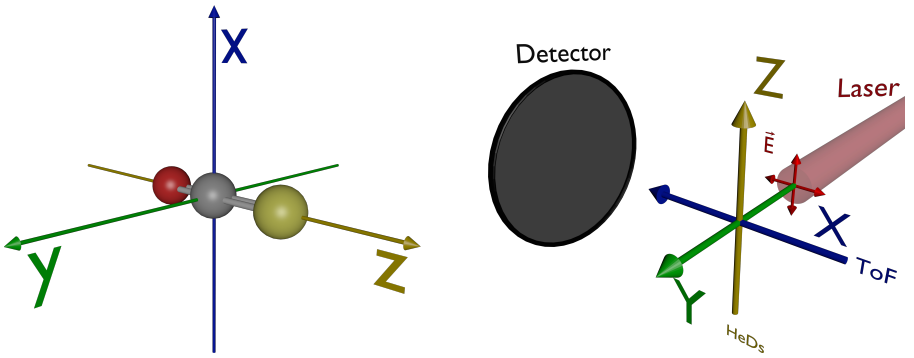

(a) The molecular (xyz) frame. **(b)** The laboratory (XYZ) frame.

Figure 1: Coordinate systems used throughout this thesis, see text for details.

Figure 1 shows the coordinate conventions used throughout this thesis. The notation for the molecule-fixed (molecular) frame is lower case $(\mathrm{x}, \mathrm{y}, \mathrm{z})$. The notation for the space-fixed (laboratory) frame is upper case $(\mathrm{X}, \mathrm{Y}, \mathrm{Z})$.

Figure 1 (a) shows an OCS molecule in the molecular frame. In general, for linear molecules, the most polarisable axis of a molecule is placed along the z axis when defining polarisability elements. For symmetric top molecules, the least polarisable axis is generally placed along the y axis when defining polarisability elements.

Figure 1 (b) shows the laboratory frame together with relevant aspects of the experimental apparatus. The detector is placed in the YZ plane, and the ions are focussed onto it along the ToF (X) axis. The laser beams always propagate along the Y axis, such that the XZ plane is the polarisation plane. The helium droplet beam travels along the Z axis.

Abbreviations

HeD(s)	Helium Droplet(s)
ToF	Time-of-Flight
LPA	Least Polarisable Axis
MPA	Most Polarisable Axis
MPP	Most Polarisable Plane
MDC	Monomer-Doping-Condition
DDC	Dimer-Doping-Condition
TDC	Trimer-Doping-Condition
NAR	Non-Axial Recoil
CEI	Coulomb Explosion Imaging
LIA	Laser-Induced Alignment

CHAPTER 1

Introduction

This thesis represents a summary of the main projects I have worked on during my PhD study. At the start of my PhD, a new helium droplet machine was built, improving experimental conditions and enabling a wider range of experiments to be undertaken. Among the first of these experiments were several alignment experiments that greatly improved understanding of the laser-induced alignment of molecules in helium droplets. With alignment of single molecules becoming more thoroughly understood, our focus turned to more ambitious experiments. An overarching goal within Femtolab is performing a time-resolved bimolecular reaction inside helium droplets. One way to achieve this would start with the creation of weakly-bound complexes of molecules inside helium droplets. Having created a weakly-bound complex, it may then be possible to initate a reaction via photoexcitation and follow the reaction in real time - this has been demonstrated for many unimolecular reactions [1–3]. This is a challenging experiment, thus creation, manipulation, and characterisation of these complexes represents an important first step towards this goal.

All the work presented in the main body of this thesis was performed in helium droplets. Accordingly, chapter 2 presents some properties of low-temperature helium and discusses the generation and use of superfluid helium droplets, especially with regards to complex formation. Following this, chapter 3 presents an introduction to the topic of molecular complexes, and a review of the field (of both isolated complexes and complexes solvated in helium droplets) is also presented. This review shows that the majority of prior work on molecular complexes has been performed in the frequency domain, whereas in this thesis all work is

performed using ultrashort laser pulses as a probe, affording femtosecond time resolution at the expense of frequency resolution. Furthermore, the work presented here is generally performed on aligned molecules, where the alignment is induced by a strong laser field. Chapter 4 presents the theory behind both of these techniques, laser-induced alignment and Coulomb explosion imaging. In addition, an introduction to ion imaging is presented here.

Chapter 6 describes the experimental setup used in experiments throughout this thesis, and includes both a description of the helium droplet machine and a discussion of the laser systems used. Having recorded data on this machine, it is analysed using a number of techniques, and these are detailed in chapter 5. In addition, this chapter details some experimental phenomena are commonly referred to throughout the thesis, so are documented here for reference.

Alignment and Imaging of Complexes of Small Triatomic Molecules

Chapter 7 describes the first experiment on complexes of molecules performed in Femtolab. This was a study of the CS_2 dimer inside helium droplets, where it is demonstrated that it is possible to generate dimers of CS_2 by controlling the partial pressure of CS_2 vapour in the doping cell on the new helium droplet machine. Having established this, the study then focussed on the adiabatic alignment of this dimer with linearly and circularly polarised laser pulses. It was shown that it is possible to align and image the CS_2 dimer, and unambiguously determine its structure. Continuing with the CS_2 dimer, chapter 8 describes a more thorough study of the alignment dynamics of the CS_2 dimer with a circularly polarised laser pulse. The power-dependent degree of alignment of the dimer is measured and compared to simulation. Chapter 9 takes the ideas presented in chapter 7 further, and applies the technique to dimers and trimers of OCS molecules. OCS is a polar molecule, and prior studies of complexes of polar molecules in helium droplets have shown that there is a precedent for helium droplets to anneal exotic non-ground state structures of complexes of polar molecules. The results of this study were somewhat surprising, and show that some hitherto unseen structures of OCS trimers are annealed inside helium droplets.

All the work discussed in the main body of this thesis was undertaken on molecules solvated in helium droplets. Attempts were made to study the CS_2 dimer in the gas phase, to provide a comparison to the work

presented in chapter 7 and chapter 8. These attempts were hampered by unstable experimental conditions so do not form part of the thesis proper, and are not analysed in huge detail. Despite these problems, some potentially interesting phenomena were observed here, so some selected results are presented in appendix B, for interested readers.

Anthracene in Helium Droplets

All of the studies up until this point have been performed in a way that preserves the femtosecond time resolution of the probe technique, but have not actually studied any time-resolved dynamics. In chapter 10, the first attempts at an ambitious experiment on dimers of anthracene molecules was presented. Anthracene is known to readily undergo photodimerisation following irradiation with UV light, and the ultimate goal of this experiment would be to follow this photodimerisation in real time in helium droplets. The study in chapter 10 is divided into two parts - the first part concerns attempts to determine the structure of the anthracene van der Waals dimer, which is the pre-reactive complex that dimerises under UV irradiation. The second part details preliminary efforts to do the photodimerisation, focussing mainly on finding a suitable observable that could be used to follow the photodimerisation in real time.

CHAPTER 2

Helium Droplets

Helium is a noble gas that exists in two stable isotopic forms, ^{4}He and ^{3}He[1]. It is the second most abundant element in the universe after hydrogen. The majority of the helium on earth[2] (99.99987%) exists as ^{4}He, with a very small amount (0.00013%) of the lighter ^{3}He [4]. In this work, when 'He' is used without an isotopic superscript, it refers to ^{4}He. Chemically, He is very inert, with the highest ionisation potential (24.56 eV - 198 120 cm^{-1}) of any element, and it exists as a monatomic gas at room temperature and pressure. It has the lowest boiling point (4.2 K) of any element, and has a very high heat conductivity in the liquid phase [5]. It also has a very low density in the gas phase (several times lighter than air), and diffuses through solids three times faster than air. Its main industrial uses take advantage of these properties, and include cryogenic cooling; use as a purge gas or protective atmosphere; and use in leak detection. It is also used in gas mixtures for diving; as a gain medium for Helium-Neon lasers; and in party balloons[3]. In this chapter a summary of the properties low-temperature helium is given, as well as an overview of the generation of doped helium nanodroplets.

[1] Nine isotopes of helium are known, with only the two listed being stable. The longest lived unstable isotope is ^{6}He, with a half life of 800 ms.

[2] The isotopic abundance varies with provenance - there is around 100 times more ^{3}He in space than on earth.

[3] The reader is left to decide whether this last use should be considered wasteful.

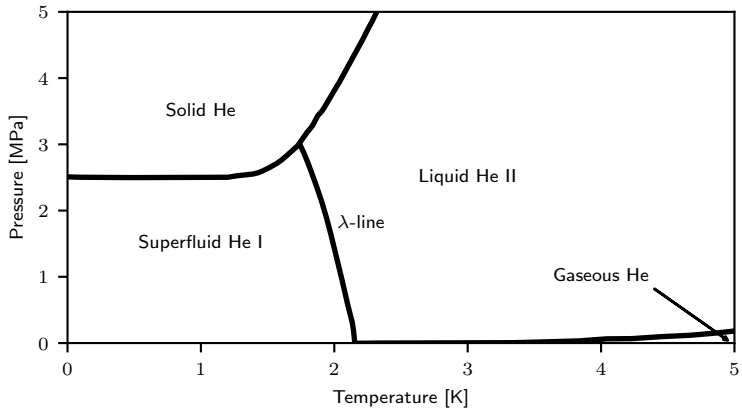

Figure 2.1: Sketch of a pT-phase diagram of ^{4}He. The λ-line, below which liquid helium becomes superfluid helium, is annotated.

2.1 Low-Temperature Helium

A sketch of a low temperature phase diagram of ^{4}He is shown in Fig. 2.1. At atmospheric pressure, below 4.22 K, He gas will condense into the liquid He I phase. Continued cooling at atmospheric pressure will lead to a further phase transition at 2.18 K to the He II phase. The p-T line where this He I to He II transition is observed is called the λ-line. In the He I phase (above the λ-line), He behaves as a normal fluid; whereas in the He II phase (below the λ-line), it behaves as a superfluid. Superfluid He exhibits many remarkable phenomena, including vanishing viscosity; film flow; and a very high heat conductivity, among others. Of these properties, the vanishing viscosity is perhaps the most famous. A particle travelling through superfluid helium will experience zero viscosity (zero friction) at speeds lower than $58\,\mathrm{m\,s^{-1}}$. This velocity was first predicted by Landau [6] and later proven experimentally [7]. This velocity, above which the viscosity is no longer zero, is known as the 'Landau velocity' for this reason.

Many of these properties make superfluid helium an ideal medium to solvate molecules in for spectroscopic interrogation. The high heat conductivity means that any dissolved species will be efficiently cooled to the (very low) temperature of the surrounding helium. Additionally, the dielectric constant $\epsilon = 1.005$, so He is transparent to wavelengths from the far IR to the deep UV, allowing any solvated species to be interrogated using many standard spectroscopic techniques. Other noble gases can be used as media in which to solvate molecules for spectroscopy, usually as

solid cryogenic noble-gas matrices [8]. Compared to other noble-gas matrices, the interaction betweem the He atoms in superfluid He II is much smaller than the interaction between atoms for any other noble-gas, and the interaction between a solute molecule and the matrix is also correspondingly weaker for He. This means that a molecule solvated in superfluid He is less perturbed by the solvation environment than a molecule in a rare-gas matrix, and its behaviour is therefore more similar to that of an isolated molceule. Further insight into the different solvation characteristics of superfluid helium compared to other noble-gas matrices is given by the de Boer parameter, Λ^* [9]:

$$\Lambda^* = \frac{\lambda_{\mathrm{dB}}}{R_0} \tag{2.1}$$

Where λ_{dB} gives the length scale of the interaction between the rare-gas atoms, the subscript dB refers to the fact that this is related to the momentum (and therefore temperature) of the atoms, like a de Broglie wavelength, but it is *not* equivalent to the thermal de Broglie wavelength. R_0 is the classical distance of closest approach of the atoms. As such, Λ^* is effectively a ratio of the quantum-mechanical and classical length scales, and thus provides a measure of how delocalised (and quantum-mechanical in nature) the medium is. A high de Boer parameter signifies a highly delocalised medium, and the de Boer parameter for superfluid ^{4}He is 2.87. In contrast, the de Boer parameter for a Xe matrix it is 0.06, so Xe is a much more classical, crystalline medium. This is consistent with observation, as molecules solvated in a Xe matrix are observed to behave essentially as molecules in a crystal field [8], unlike molecules solvated in superfluid helium [9]. The more delocalised nature of the helium results in behaviour that is much more similar to the behaviour of an isolated molecule in the gas phase, as the size of the cavity in which a solvated molecule resides is flexible and can be tailored to the size of the molecule. These ideas will be explored further in chapter 3.

However, the weak interaction between the He atoms and a solute molecule is also a disadvantage when using bulk superfluid helium as a solvent. Attempting to use bulk superfluid helium (necessarily in a container) to dissolve foreign species will result in rapid aggregation of the solute molecules on the container walls, as the interaction of any dopant with the container will be stronger than the weak interaction with the solvating He. A solution to this is to remove the container walls, by solvating molecules in droplets of superfluid helium.

2.2 Superfluid Helium Droplets

Expansion of cold (10-35 K) ^{4}He at high (20-80 bar) pressure through a small (typically 5 µm) nozzle into vacuum results in a beam of freely-levitating helium nanodroplets (henceforth referred to as simply 'HeDs') propagating through the vacuum chamber. Figure 2.2 is adapted from reference [10], and shows how the droplet size depends on the expansion conditions. Broadly, a lower nozzle temperature and a higher expansion pressure results in larger droplets. The expansion can be divided into supercritical and subcritical regimes, as annotated on the graph. When the expansion is in the subcritical regime, the number of atoms formed per droplet is relatively small ($N \approx 10^4$). At a given pressure, the expansion becomes supercritical as the temperature is lowered below below a certain threshold, and the droplet size increases dramatically ($N > 10^5$). The onset of supercritical expansion occurs at higher temperatures as the expansion pressure increases. At very low temperatures (below 5 K - not depicted in Fig. 2.2), liquid helium expands through the nozzle and very large ($N \approx 10^{10}$) droplets are formed via Rayleigh breakup of the liquid beam.

In Femtolab, work is generally undertaken in the subcritical regime, making droplets of around 5000-10000 He atoms. The distribution of droplet sizes within the expansion is rather broad and fits a log-normal distribution, and becomes increasingly broad as the nozzle temperature drops and the mean droplet size increases. As the droplets are formed, they cool down via helium evaporation as they propagate through the vacuum apparatus, reaching an equilibrium temperature of 380 mK after some µs of flight time. This beam of droplets can then be 'doped' with a foreign species.

2.2.1 Doping of Molecules in Helium Droplets

When a HeD collides with another atom or molecule, that atom or molecule can be solvated by the droplet. As such, passing a droplet beam through an area with a relatively high number density of a certain molecule will result in many of the droplets picking up molecules and becoming doped HeDs. In practice, this is achieved by passing the droplet beam through a gas cell containing some partial pressure of a foreign atom of molecule - the way this is achieved experimentally is presented in chapter 6.

The doping of atoms and molecules into HeDs is governed by Poisson statistics, with the probability of picking up k molecules P_k being

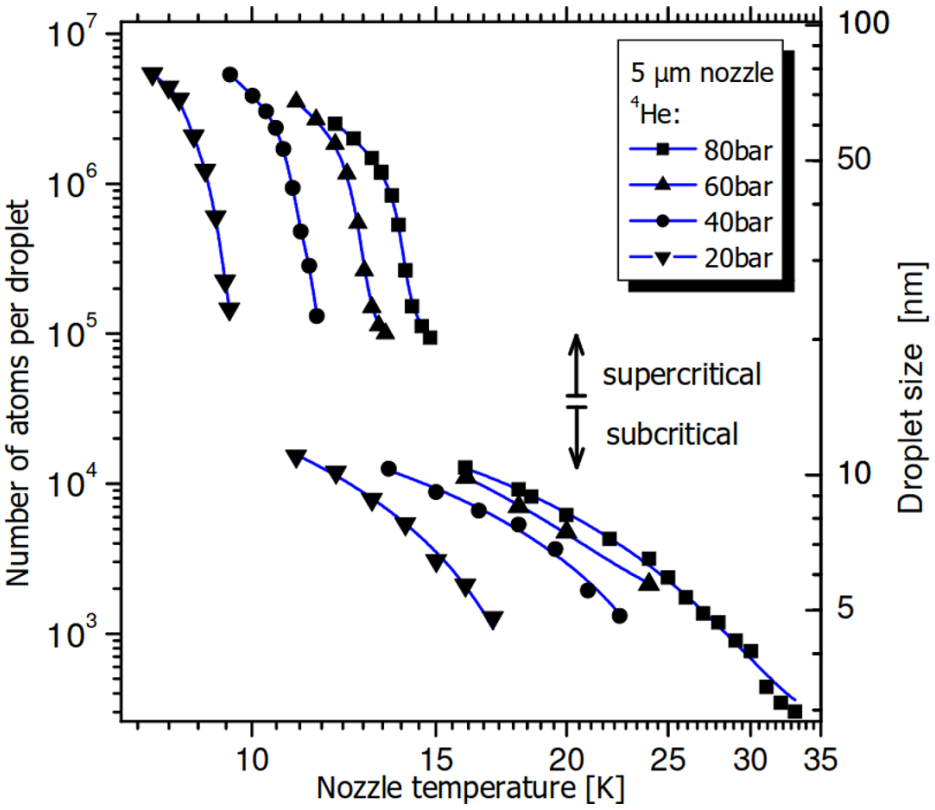

Figure 2.2: Mean droplet size plotted as a function of nozzle temperature for a variety of different expansion pressures of ^{4}He, expanding through a 5 µm nozzle. This figure was adapted from [10].

given by Eq. 2.2 [11].

$$P_k(n) = \frac{(\sigma n L)^k}{k!} \mathrm{e}^{-(\sigma n L)} \tag{2.2}$$

Where σ is the pickup cross-section of the droplet, and was simply assumed to be the cross-sectional area of a droplet (see later); n is the number density of dopant molecules in the cell; and L is the length of the pickup cell. This relation is plotted as a function of pressure[4] for $k = 1 - 4$ in Fig. 2.3 for droplets consisting of 10000 atoms in a pickup cell of length 7 cm. Strictly speaking, this relation is only true if the pickup cross-section σ is negligibly reduced following the solvation of each successive molecule (see later). As this thesis primarily concerns the study of clusters of

[4]The pressure and number density are linked via the ideal gas equation.

molecules in HeDs ($k = 2, 3$), it is informative to consider the doping process in some detail.

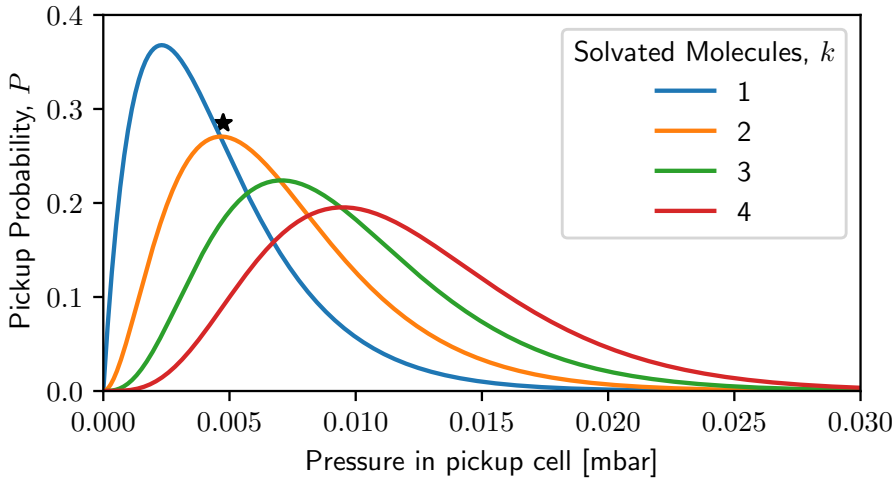

Figure 2.3: Probability of solvating k molecules, P_k, plotted for $k = 1-4$ as a function of pickup cell pressure. The star shows the point at which the most dimers ($k = 2$) are doped into the droplet beam (see text).

It is immediately clear from Fig. 2.3 that, except for at low pressures, it is not possible to isolate one single cluster size for study. More specifically, we cannot enter a region where there are substantial amounts of doubly- or triply-doped droplets (dimers or trimers) and negligible amounts of all other cluster sizes. It is possible to enter a region where there are more dimers than any other cluster size (shown with a star on Fig. 2.3), but there will be substantial amounts of trimers and tetramers here. For the techniques used in this work (detailed in later sections), contributions from cluster sizes other than the one desired for study have the potential to contaminate experimental results and make analysis difficult. For this reason, doping pressures are kept as low as feasibly possible while retaining enough of the desired signal to facilitate study. In practice, this means that when study of doubly doped droplets is desired, there are always substantially more singly-doped droplets than doubly doped droplets (with a minimal amount of triply-doped droplets). The contributions from different cluster sizes can sometimes be separated relatively easily (see section 5.2), but it is still best to try to maintain clean conditions producing as few different cluster sizes as realistically possible.

When a molecule is doped into a HeD, it is rapidly cooled down

to the equilibrium temperature of 380 mK of the droplet via helium atom evaporation, with each helium atom carrying away approximately $5\,\mathrm{cm}^{-1}$ (0.6 meV) of energy. Considering a small molecule such as CS_2, at room temperature the total energy deposited into the droplet is roughly equal to $9/2kT$, leading to a total energy of around $900\,\mathrm{cm}^{-1}$ (0.11 eV) being deposited into the droplet. This will result in the evaporation of 180 He atoms from the droplet per CS_2 molecule solvated. This means that the droplet will shrink as each molecule is solvated, which might be expected to affect the pickup-cross section defined in Eq. 2.2, reducing it for each successively solvated molecule. In practice, for small molecules, this effect is negligible provided that the size of the droplet is large enough. The radius R_0 of a ^{4}He droplet consisting of N atoms is given by [12]:

$$R_0(\text{Å}) = 2.22N^{1/3} \tag{2.3}$$

Accordingly the pickup cross section, σ, can be defined simply as the area of a circle with radius R_0, such that:

$$\sigma(\text{Å}^2) = \pi R_0^2 \tag{2.4}$$

The pickup cross section of a droplet consisting of 10000 atoms is therefore around $7100\,\text{Å}^2$. Following solvation of a CS_2 molecule, this cross-section will be reduced to $7050\,\text{Å}^2$, a negligible decrease. Concluding, providing that the number of evaporated helium atoms is small compared to the total droplet size, the change in pickup cross-section on solvation of a molecule is negligible.

An obvious question to ask following this discussion is: where does the dopant actually reside in the droplet? It might seem intuitive that it will be solvated in the center of the droplet, but in fact a more delicate balance of forces is at play. When a molecule is solvated in a HeD, energy is required to create a cavity inside the droplet (breaking the surface tension of the droplet), but energy will also be released by the solvation of the dopant by the He atoms. Ancilotto *et al.* derived a relation taking these forces into account, resulting in the Ancilotto parameter, λ, given by Eq. 2.5 [13]:

$$\lambda = \frac{\rho\epsilon r_{\text{min.}}}{\sigma 2^{1/6}} \tag{2.5}$$

where ρ is the density of the droplet, σ is the surface tension, and ϵ and $r_{\text{min.}}$ are the Lennard-Jones parameters for the interaction of the dopant with a helium atom. This is very simply derived by considering that the net energy cost of solvating a molecule in helium is approximately equal to $\sigma r_{\text{min.}}^2$ - the energy required to break the surface tension and create a cavity of radius $r_{\text{min.}}$. The net energy gain can be estimated as $\epsilon\rho r_{\text{min.}}^3$, the total

interaction of the dopant with the surrounding helium atoms. The ratio of these two parameters (gain/cost) gives the Ancilotto parameter[5]. When $\lambda > 1.9$, the dopant is solvated inside the droplet as the interaction with He overcomes the surface tension. When $\lambda < 1.9$, the dopant will reside on the surface. In practice, all closed-shell organic molecules are solvated inside the droplet, with any species containing unpaired electrons residing on the surface (such as alkali metal atoms or dimers). Additionally, electrons are known to be strongly heliophobic, so radicals generated in the center of the droplet (e.g. via photoexcitation of a closed-shell molecule) are ejected due to this repulsive interaction [14], while a free electron created in a droplet will create a 'bubble' inside the droplet [15].

A final consideration which has not yet been mentioned, is whether or not the superfluid properties evident in bulk superfluid helium are also exhibited in superfluid HeDs. This was most beautifully demonstrated by Grebenev *et al.*, who performed the 'Microscopic Andronikashvili Experiment' [16].

The original Andronikashvili experiment was perfomed in bulk superfluid helium, by Elephter Andronikashvili [17]. The crux of the experiment was the immersion of two rotating discs into a bath of liquid helium, and observing the sharp decrease in the moment of inertia of the discs as the helium was cooled to below 2.18 K. This was powerful evidence for the superfluidity of the He II phase. The Microscopic Andronikashvili experiment was performed by rotationally exciting OCS molecules inside both ^{4}He droplets (superfluid) and ^{3}He droplets (normal fluid). The rotational spectrum was recorded and is shown in Fig. 2.4. The spectrum is completely broad and featureless in the normal fluid ^{3}He droplets (panel (a)), but sharp rotational structure was observed in the superfluid ^{4}He droplets (panel (b)), as the OCS molecules were free to rotate in the frictionless medium. This sharp rotational structure is very reminiscent of a gas-phase OCS spectrum, and the main difference observed between the spectrum observed in superfluid ^{4}He and the spectrum recorded for isolated (gas-phase) OCS in molecular beams is the spacing of the rotational lines. The rotational lines are more closely spaced in the droplets than in the gas phase, indicative of the rotational constant being reduced, or the moment of inertia being increased. This increase in the moment of inertia was ascribed to the OCS 'dragging' a helium solvation shell with it as it rotates. This experiment confirms that the droplets exhibit the same superfluidity as is known to exist in the gas-phase.

[5]The additional factor of $2^{1/6}$ arises from the Lennard-Jones potential.

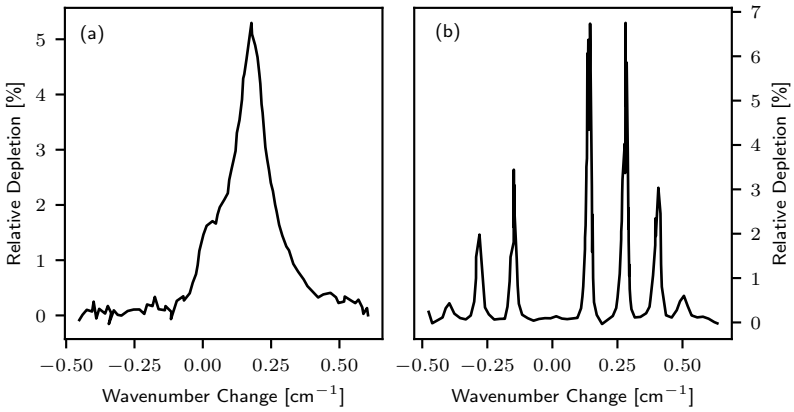

Figure 2.4: Rotationally resolved IR spectra of OCS in (a) ^{3}He droplets and (b) ^{4}He droplets. Figure adapted from reference [16].

2.3 Summary

Here some basic properties of low-temperature helium and HeDs have been discussed. A discussion of doping molecules into HeDs was presented, which is central to this work, and this discussion will be referred back to throughout the thesis. The following chapters build on this by discussing the nature of weakly-bound molecular complexes, and then considering the creation of such species inside HeDs. In addition to this, the effect of HeDs in ion imaging experiments, and especially the effect of non-axial recoil, will be explored in subsection 4.2.3.

CHAPTER 3

Molecular Complexes

Complexes of molecules bound by non-covalent interactions are central to this work. Some defintions will be provided, followed by a discussion of the relevance of molecular complexes to the natural sciences and an overview of current work. Finally, the use of HeDs in studying such complexes will be explored and reviewed.

3.1 Definitions

A molecular complex is broadly defined as a structure consisting of two (or more) individual molecules, bound by *non-covalent* interactions. The subsequent discussion draws much on the definitions of Hobza and Dethlefs-Müller [18,19], and Israelachvili [20]. A *covalent* interaction is one in which the (unfilled) orbitals of two molecules overlap. The electron density in the area where the orbitals overlap increases, which creates the strength in the bond. As covalent interactions rely on orbital overlap, the effective range of them is generally less than 4 Å. Conversely, *non-covalent* interactions can be observed to act over larger distances, and sometimes over very large distances (>10 Å [21]), so orbital overlap cannot be the primary mechanism for their binding strength. Over these distances, electrostatic interactions between multipoles (permanent, induced, or instantaneous) are the dominant interactions that give non-covalent interactions their binding strength.

Non-covalent interactions can be further subdivided into three categories: permanent multipole - permanent multipole (PM-PM) interactions; permanent multipole - induced multipole (PM-IM) interactions; and

induced multipole - induced multipole (IM-IM) interactions. The nomenclature surrounding this topic is often somewhat unclear, so the following discussion aims to be as general as possible.

PM-PM interactions are interactions between *permanent* multipoles, such as between permanent dipoles, or between two ions (monopoles). They are highly directional and can be very strong, generally dominating non-covalent interactions where present. PM-IM interactions are interactions between a permanent multipole and an *induced* multipole. An induced multipole is one that is induced in a polarisable molecule by the electric field of a permanent multipole. For example, the strength of the induced dipole μ_{ind} is related to the polarisability α of the molecule it is induced in, and the field strength E of the field inducing the dipole by Eq. 3.1. The polarisability α can be thought of as a measure of how easily the electrons in the molecule can be 'driven' by an external electric field. PM-IM interactions are generally weaker than PM-PM interactions[1], and are generally less directional.

$$\mu_{ind} = \alpha E \tag{3.1}$$

IM-IM interactions, are the interaction between two induced multipoles, and are commonly referred to as Dispersion interactions when they exist between two induced dipoles. In this case, an instantaneous dipole (formed via random movement of electrons) induces another instantaneous dipole in a neighbouring atom/molecule, which leads to electrostatic attraction between the two dipoles. Accordingly, Dispersion interactions are fundamentally quantum mechanical in origin. This generally results in a weak interaction which is highly-non directional, but the interaction can become substantial where large, delocalised, highly polarisable electron clouds are present (such as in large aromatic systems).

In most cases, all the interactions described above will be attractive due to the attraction between opposite charges. Of the three interactions mentioned, only PM-PM interactions can be repulsive (repulsion between two like charges), as a permanent multipole cannot induce a multipole that it would be repelled from (as in a PM-IM or a IM-IM interaction). Additionally, we will generally refer to interactions between permanent dipoles when referring to PM-PM interactions, and these are unlikely to be repulsive provided that each dipole is free to move into a geometry where the interaction is attractive. Accordingly, these forces must be balanced by some repulsive effect. This repulsive effect, referred to as 'exchange-repulsion' energy, can be imagined simply as the repulsion of electron

[1]Except for higher order multipoles in highly symmetric systems, where the permanent multipole interaction can be very weak.

clouds in two occupied orbitals. More precisely, it can be considered as the interaction between two occupied orbitals resulting in the increase of electron density in an anti-bonding orbital (c.f. the interaction between two partially occupied orbitals increasing the electron density in a bonding orbital).

The term *van der Waals interaction* is generally used by chemists to refer to any non-covalent interaction generally, or is taught (wrongly) to be a synonym of 'dispersion force' [22, 23]. Neither of these terms are precise. In the first case, metallic and ionic bonding are both non-covalent interactions, but would not generally be thought of as van der Waals (vdW) interactions. In the second case, dispersion forces are only attractive, yet repulsions (and other, attractive, forces) are an important part of vdW forces. More precisely, vdW interactions can be considered as the net effect of all of the aforementioned (PM-PM, PM-IM, IM-IM, exchange-repulsion) non-covalent forces, and this is what will be meant the term 'vdW force' or 'vdW interaction' throughout this thesis. As such, in this work a molecular complex is defined as a structure of two or more molecules bound by vdW interactions[2].

3.2 Studying Molecular Complexes

Here the motivation for studying molecular complexes, together with a brief overview of the field, is presented.

3.2.1 Motivation

Molecular complexes and vdW interactions are ubiquitous in the natural sciences. They play an important role in a large number of different phenomena, including bimolecular reactions [24], exciplex formation [25], and chiral recognition [26]. The structure of supramolecular assemblies is dictated by them [19, 27, 28], as are the structures of large biomolecules [29]. Chemical interactions fundamental to industry and medicine, such as the binding of proteins and drugs [30–32], the binding of molecules to catalysts [33, 34], and the self-assembly of nanoparticles [35, 36], are also governed by such forces.

From a more fundamental perspective, molecular complexes provide an important insight into pre-reactive complexes, and their creation is a prerequisite of the holy grail for time-resolved dynamicists: making the 'molecular movie'. Additionally, all bimolecular reactions proceed

[2]Strictly, the complex need not be constructed entirely of neutral molecules, however this is what it is taken to mean in this work

through some high-energy complex, the transition state, as the reaction progresses. Understanding these metastable complexes is a fundamental building block of understanding chemical reactivity. Intramolecular dynamics of complexes have also been studied [37,38], providing deep insight into the fundamental physics of the processes involved. At a more abstract level, complexes of simple molecules are often very thoroughly understood, and can provide important benchmarks for computational chemists and theorists [39].

In addition to this, small complexes can be viewed as 'building blocks' of larger (often macromolecular) systems. This 'bottom-up' approach allows large systems to be broken into simpler subsystems, with the idea that a thorough understanding of the subsystems leads to a better understanding of the large system as a whole [40]. Controlling the formation such that systems are built up molecule-by-molecule allows an understanding of the intermolecular and intramolecular forces to be gained as the system grows in size [41]. Moving further into the condensed phase, forming complexes in dissipative media, or forming complexes of molecules with multiple solvent molecules, can allow detailed understanding of different solvation and energy dissipation processes.

In the following sections, an overview of the study of molecular complexes in the gas phase is presented. Following this, we shall see some of the limitations of gas phase work, and explore the utility of HeDs as a tool for studying molecular complexes.

3.2.2 Molecular Complexes in the Gas Phase

Gas-phase study of molecular complexes is an extensive field; a thorough review of which is beyond the scope of the work presented here. An overview of cluster formation is provided, together with a review of conventional experimental techniques. Before considering this, it is useful to understand the physics of complex formation. The binding energy of a typical vdW complex is low, on the order of $500\,\mathrm{cm}^{-1}$ ($60\,\mathrm{meV}$). The collision that must occur for the complex to be formed must therefore occur at low energies, and a collision with a third body (if not more molecules) is required to carry away kinetic energy and prevent immediate breakup of the complex.

In a gaseous sample at equilibrium the number of vdW complexes is low, as the high energy of the molecules prevents the low energy collisions required to form weakly-bound clusters. As the temperature drops, the number of complexes increases, until the condensation point is reached and the vapour pressure of the sample dramatically drops, reducing the

absolute numbers of clusters. Even under the most favourable conditions, the number of molecular complexes in a gas under equilibrium conditions is never greater than a few percent [42][3]. Moving to non-equilibrium conditions (e.g. expansion in a supersonic jet) can greatly increase the concentration of clusters. High-pressure expansion of molecules (with a carrier gas) into vacuum results in a highly directional beam, where the relative velocities of the molecules in the beam are very low and the rotational (and to some extent vibrational) degrees of freedom are also effectively cooled. This results in a beam of internally cold and translationally (relatively) cold molecules. Collision energies are therefore lower, and carrier gas molecules are present to remove the binding energy from nascent complexes such that they remain in a bound state. This is the standard method by which cold gas-phase molecular complexes are formed, and the low internal temperatures mean that the density of populated states is low, making spectroscopic analysis more insightful.

High resolution spectroscopy across a wide range of frequencies has been the standard technique for the analysis of gas-phase molecular complexes. Microwave spectroscopy has been applied to the study of molecular complexes [27, 43, 44], and the high sensitivity of Fourier-transform microwave (FTMW) techniques make it a very useful for probing rotations and deriving rotational constants, leading to high precision structural determination. However, for non-rigid systems, these techniques can only provide information about vibrationally averaged structures [19], but dynamical information can be extracted from the rotational linewidths. Measurements of dipole moments can also be used to find information about the distribution of charges in a complex, which can be a complementary technique to high-resolution MW spectroscopy [45].

Infrared spectroscopy has also been applied to the study of gas-phase molecular complexes [46, 47]. Rovibrational spectroscopy can provide detailed structural information like pure rotational (microwave) spectroscopy, but the rotational spectrum associated with a specific vibrational state can be measured. This can be challenging, as IR sources that are narrowband enough to resolve rotational structure often have very low power, which can be problematic when combined with low concentrations of complexes, or have poor wavelength tunability (making spectral acquisition cumbersome). However the (relatively recent) development of tabletop, high power, easily-tunable cw OPO systems [48] has enabled such experiments to be done in conventional university laboratories. Al-

[3]Except in extreme cases where very strong intermolecular forces cause extensive clustering, such as in acetic or formic acid.

ternatively, large external facilities such as FELIX (Free Electron Laser for Infrared eXperiments) can be used. IR spectroscopy has been used to determine structures of complexes of a wide range of systems. From complexes of small triatomics like N_2O [49,50], CO_2 [51], and CS_2 [52,53], to metal-acetylene clusters [54], to clusters of noble gases with aromatic systems [47]. These techniques rely on high-quality theoretical calculation to compare experimental results with, and there are a large number of diagnostic tools available to aid the spectroscopist in interpreting the data. This is a very widely used technique, and one which is often very decisive.

There are, however, limitations of frequency resolved techniques, and of studying complexes in the gas phase. For example, a high-resolution frequency resolved technique necessarily has low temporal resolution. This means that to undertake time-resolved studies either means that the timescale of the processes involved must be very long (ns or longer), or the frequency resolution must be compromised. Additionally, jet expansion of molecules into the gas phase limits the size of the complex that can be studied. Larger molecules have higher vapour pressures and are harder to get into the gas phase, and when complexes form they are often less efficiently cooled by the expansion process than complexes of smaller molecules. This results in a warmer complex, meaning that the resulting spectra are broadened, hindering interpretation [27].

It is a consequence of fundamental Fourier theory that high frequency resolution necessarily means low temporal resolution and vice-versa. To study time-resolved nuclear motion (fs timescale) using typical laboratory radiation sources ($\lambda_0 = 400\,\text{nm-}10\,\mu\text{m}$), the required bandwidth ($\Delta\lambda$) ranges from 5 nm to 5 µm. Therefore, techniques with high time resolution, such as Coulomb Explosion Imaging, or ultrafast ionisation, in general do not provide the high frequency resolution that spectroscopic techniques do[4]. Coulomb explosion imaging has been used to image the structures of small vdW complexes [55, 56], and has been used to study time-resolved torsion of a substituted biphenyl molecule [57]. While the structural probe is not as decisive as that given by frequency-resolved techniques, monitoring the time evolution of states in real time can be a powerful complement to frequency resolved techniques.

The problems inherent in making complexes via jet expansion can

[4] A possible exception to this rule is femtosecond transient-absorption spectroscopy, where the spectral width of an ultrashort probe pulse is used to measure an absorption spectrum of the system in question, whilst retaining the time resolution. However, if a fast transition is measured, then the linewidth is broad anyway. The limitations of this technique are low sensitivity, which is often a problem with low concentrations of complexes.

be circumvented by finding alternate ways to make the complex. As briefly mentioned previously, complexes can be made in cryogenic rare-gas matrices [8, 58–60]. Use of such matrices is advantageous, as they provide low (typically 4-10 K but sub-1 K is possible) temperatures, and prevent highly reactive complexes from undergoing further reactive collisions. The long lifetime of trapped complexes means that many optical spectroscopic techniques can be used. Rare-gas matrices also provide a way to create large concentrations of such complexes, and materials with a much higher boiling point to be studied than is possible in a supersonic jet. The downside of using rare-gas matrices is that the matrix has a crystalline structure, which places a hard limit on the size of the complex that can be solvated, as it cannot be bigger than the interstitial sites in the matrix. Another consequence of this is that resulting spectra are often highly shifted due to crystal-field splitting and interaction with the rigid matrix. An ideal solution would therefore be a non-rigid cryogenic matrix, where the cavity size is tailored exactly to the size of the solvated complex, and the interaction with the matrix is weak. Such a solution is found by using HeDs as a matrix.

3.2.3 Molecular Complexes in Helium Droplets

As discussed in chapter 2, HeDs are characterised by a very low temperature (380 mK), very high heat conductivity (30 times higher than Cu), and vanishing viscosity [9]. This makes them an ideal medium for the creation of molecular complexes, as the superfluidity means that the droplet will form a solvation shell that is exactly tailored to the size of the dopant. In contrast to rare-gas matrices, the HeD forms a 'personalised nano-cryostat' for the dopant molecule/complex [9]. A consequence of this flexiblity in the solvation environment (and the weak interaction) is that spectra of molecules solvated in HeDs are much less shifted away from the corresponding gas-phase spectra, rendering comparison with calculations (on isolated molecules) easier.

Any molecule that can be bought into the gas phase can be solvated in a HeD, ranging from H_2 to large biomolecules or salt molecules [61], and will be efficiently cooled via helium evaporation. When forming a complex inside a droplet, the molecules are solvated and cooled individually, and will bind inside the droplet itself. Any energy that is released as the molecules approach each other will be evaporated away by the He environment (each He atom carrying away $5\,\mathrm{cm}^{-1}$ (0.6 meV)), such that the molecules meet each other with minimal extra energy available to rearrange, and the resultant complex is in equilibrium with the droplet at

380 mK. The sequential pickup process also gives more control of the clustering process, as the order in which molecules are added to the complex will influence the ultimate structure. This effect has been used to grow specific nanoparticles, and has been observed for Ar_n–HF complexes [62,63]. A more detailed description of the solvation process was given in chapter 2.

In a supersonic jet expansion, when a cluster is formed under collision-free conditions, it tends to anneal to the global minimum structure on the potential energy surface (PES). This occurs as there is residual internal energy in the cluster that allows it to rearrange from the geometry it was in at the point of collision, to the ground state geometry. However, a small proportion of the complexes may become trapped in local minima, especially if they are close in energy to the ground state [41, 46]. In contrast, in HeDs, complexes can be frozen into non-ground state structures that reflect the long-range forces that guide the molecules together. This occurs as the molecules in the complex approach each other along an attractive potential, and the binding energy that is released is continuously evaporated away via helium atom boiloff. The result of this is that when the molecules meet, they have little or no excess energy available to rearrange, so are frozen into a structure defined by the long-range attractive forces. This has been observed for HCN and HCCCN oligomers in HeDs, where dipole-directed linear chains of molecules not present in the gas phase are observed [64]. However, there is also some precedent for rearrangment of complexes inside HeDs, as short-range forces come into play once the molecules are close inside the droplet [65]. The very rapid cooling of the complex when solvated into the HeD can also cause the system to become trapped in local minima, which are normally inaccessible in the gas phase. This has been observed for complexes of HF–HCN [66], acetic acid [67], and H_2O [68].

Frequency Resolved Techniques

High resolution spectroscopy on complexes solvated in HeDs has so far been by the most common technique for their study. HeDs are transparent from the far IR to the deep UV, but low densities of doped droplets in a typical experiment makes standard optical spectroscopic techniques based on directly detecting the change in photon flux challenging [10], and highly sensitive techniques are needed. Emitted light from electronically excited dopants can be detected, and as such Laser Induced Fluorescence (LIF) has been extensively used. LIF can be a very sensitive technique when continuous wave (cw) laser sources are used in combination with bright transitions [69–71], but is limited to probing electronic transitions. Excitation of vibrational or rotational (and some electronic) transitions

does not lead to observable fluorescence. However, in this case, the energy from the radiation source can be deposited into the dopant which subsequently becomes excited. This excitation is rapidly dissipated by the surrounding droplet via helium atom evaporation, with each helium atom carrying away approximately $5\,\mathrm{cm}^{-1}$ of energy. This results in a shrinkage of the droplet after the radiation is absorbed. Detection of this reduction in droplet size is the basis for one of the fundamental HeD techniques, depletion spectroscopy [9–11, 72, 73].

The reduction in droplet size can be measured in two ways, using a bolometer, or via mass spectrometry. A bolometer is essentially a very sensitive temperature-dependent resistor, and when a droplet is incident on the bolometer surface, the temperature increases, which then changes the resistance. A smaller droplet will result in a smaller temperature increase, so the depletion can be monitored in this way. Electron impact mass spectrometry is another method, where high energy ($\sim$70 eV) electrons are used to ionise the He atoms in the droplet. There is then charge transfer from an ionised He atom through the droplet to the dopant molecule. The ionisation cross-section is directly proportional to the droplet size, so a reduction in droplet size due to helium evaporation is measurable as a reduction in ion signal in the mass spectrum. The advantage of mass spectroscopic detection is that the electron impact ionisation also ionises and fragments the dopant molecule, which can allow the depletion of specific cluster sizes to be monitored selectively by gating on a specific mass peak [72, 73].

Depletion techniques can be used with a very wide range of radiation sources, ranging from microwave [74] to electronic [75] excitation. Microwave spectroscopy is challenging as the energy deposited by a single microwave photon (often $<1\,\mathrm{cm}^{-1}$) is insufficient to remove a helium atom via evaporation. However, this can be overcome by successive excitation and de-excitation of a sample [74, 76, 77], and measuring the total depletion from many excitation events. Electronic depletion spectroscopy is also possible [75,78], and is useful where fluorescence is not detectable, but the transfer of electronic energy into the droplet is often slower (compared to vibrational energy transfer), making the depletion method less efficient. IR probing of vibrational transitions is where depletion is most efficient, as the relaxation of vibrational energy into the surrounding droplet is normally very efficient, resulting in large depletion signals [72, 73]. A specific form of (ro)vibrational spectroscopy that has been especially powerful is pendular state spectroscopy. In this case, a strong DC electric field is used to align polar molecules inside the droplets. This can lead to a collapse of the rotational fine structure of a rovibrational band into a single peak at

the band origin (not unlike a Q-branch). The intensity of this peak is very high, and as such this technique dramatically increases sensitivity and resolution, and has been extensively used for a variety of systems [73, 79, 80].

These techniques have been used to study a wide variety of systems, including many that would normally be inaccessible in a supersonic jet expansion. In addition to those already mentioned, some others have been observed: Entrance and exit channel complexes, such as OH – CH_4, HF – Br and CH_3 – H_2O [81–83] have been studied, providing a direct insight into chemical reactivity. Isomers of Mg – HCN, Al – HCN, and Ga – HCN, systems that have relevance for surface science, catalysis and chemisorption, have been studied [84, 85]. Complexes of salts with simple solvent molecules have also been studied, the resulting 'ionic hydrogen bonds' play a role in electrolytes, ion solvation and acid-base chemistry [86], such as complexes of NaCl-Methanol [61]. However, frequency resolved techniques still suffer from the same shortcomings as in the gas phase when observation of time-resolved dynamics is desired.

Time Resolved Techniques

Time resolved techniques have also been used in HeDs, albeit much less extensively than frequency resolved techniques. For long time dynamics (>ns), LIF can be used to study the fate of electronically excited states [10]; and dissociation of alkyl halides has been studied via ns excitation followed by fs ionisation [87–89]. Fast dynamics have also been studied using time-correlated photon counting [10], and via femtosecond pump/probe experiments using ultrafast laser sources. The latter technique has been used to study alkali metal dimers on the surface of HeDs, including studying of fragmentation dynamics [90–94]. More recently, the creation of a helium 'bubble' following electronic excitation of In atoms has been followed using time-resolved photoelectron spectroscopy [95]. This result potentially paves the way for many exciting experiments within Femtolab, as prior attempts at using photoelectrons as an observable were poorly understood [96] - this will be discussed in greater detail in chapter 11.

However, the majority of the time-resolved work on HeDs to date has focussed on electronic excitation of the droplet itself using EUV radiation sources [97–100]. Imaging of ejected atoms and electrons from electronically excited droplets has revealed much about the dynamics of excited droplet states [101]. Diffractive imaging of HeDs has also been used to image the droplet, and recent development in this field has enabled diffractive imaging of HeDs using tabletop laser systems [102]. This

provides a potential route to ultrafast diffractive imaging, which has so far not been observed.

Time-resolved experiments on complexes in HeDs have been much more limited in scope than conventional frequency resolved spectroscopic techniques (as is also the case in the gas phase). The structural probe afforded by time-resolved techniques is generally much less decisive than that given by frequency-resolved methods, so when structural determination is required, frequency resolved techniques are clearly superior. The strength of time-resolved techniques lies in their time resolution, so the majority of ultrafast imaging experiments have been limited to proof-of-principle experiments, illustrating the potential utility if the ultrafast pump/probe could be realised. Unfortunately, there are many difficulties in performing such experiments. These difficulties include low concentrations of excited molecules following photoexcitation (resulting in high background signals) and need for rigorous control of the molecular frame (especially in imaging), amongst others.

3.3 Summary

This chapter has provided an introduction to molecular complexes, and provided a brief review of prior work in the field, together with some of the common experimental techniques used. The following chapter will detail the main experimental techniques used within Femtolab (and throughout the work described in this thesis) - laser-induced alignment, and Coulomb explosion imaging.

CHAPTER 4

Experimental Techniques

This chapter details the theory behind the two experimental techniques used to acquire the vast majority of data presented in this thesis. These are Laser-Induced Alignment (LIA) and Coulomb Explosion Imaging (CEI), relevant details of the theory behind these techniques is presented here for reference.

4.1 Laser-Induced Alignment

Alignment of molecules refers to the alignment of one (or more) molecular axes to one (or more) space-fixed axes. This is a desirable ability to have for a chemist. Many chemical reactions start with a collision between at least two molecules. This collision must occur with sufficient energy to overcome any reaction barrier, but the collision must also be between the correct parts of the molecules involved for reaction to occur. Considering perhaps the archetypal bimolecular organic reaction, the S_N2 reaction (shown in Fig. 4.1). For reaction to occur the nucleophile (Nu^-) must collide with the central carbon at an angle of 180° to the leaving group (LG). This maximises the electronic overlap between the lone pair on the nucleophile with the σ^* orbital of the C–LG bond. Nucleophilic attack at other angles than this will not result in a reactive collision, and therefore no reaction.

Realistically, an organic chemist is performing experiments in the solution phase at (relatively) high temperatures, so the random motion of molecules in solution ensures that reaction will occur *eventually*. However, this serves to illustrate that the alignment and orientation of molecules rel-

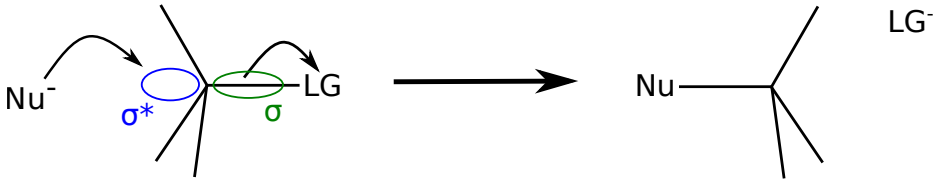

Figure 4.1: General S_N2 reaction mechanism. The nucleophile Nu^- must attack the σ^* orbital of the C–LG bond.

ative to one another is important in chemistry. There are also techniques in which having an aligned ensemble of molecules would be a great advantage to the scientist, such as crossed molecular beam scattering [103, 104], photoelectron spectroscopy [105,106], high-harmonic generation [107–110], and charged particle imaging [111–113]. Ultimately, having *more* control over your molecular sample is always better than having *less* control - and control of the spatial alignment of molecules is often especially useful.

Before discussing the ways in which alignment can be induced, it is useful to define some terminology. Considering an ensemble of iodobenzene (IPh) molecules in the gas phase, their normal state of existence is defined as 'unaligned', as the molecules all point in random directions. Confinement of one molecular axis to the polarisation axis of a linearly polarised laser field results in an ensemble that is '1D-aligned'. IPh is an asymmetric top[1] molecule, thus it can be confined about more axes than one, if it is confined about two molecular axes (and the third by extension), the ensemble is '3D-aligned'. This is illustrated in Fig. 4.2. Note that in all cases the molecules are free to point in either direction (up or down). To break this head-to-tail symmetry ('orienting' the molecules) usually requires another electric field (either a DC field or another laser field), in addition to the alignment laser. Orientation, therefore, implies alignment. Orientation is not used in this work, but is included here for completeness.

Alignment can be induced by a number of methods. These include: stretching molecules on a polymer film [114, 115]; via quantum-state selection in hexapole focusers [116, 117]; via 'brute-force' orientation using strong DC fields [118]; or via the application of strong or weak AC fields from a laser [119–121]. Techniques that rely on DC fields require that the molecule in question is polar, whereas using an AC laser field requires that the polarisability of the molecule is anisotropic. LIA can be induced using tabletop ns or fs laser systems [122–125], and alignment using strong laser

[1] All three moments of inertia $I_a \neq I_b \neq I_c$.

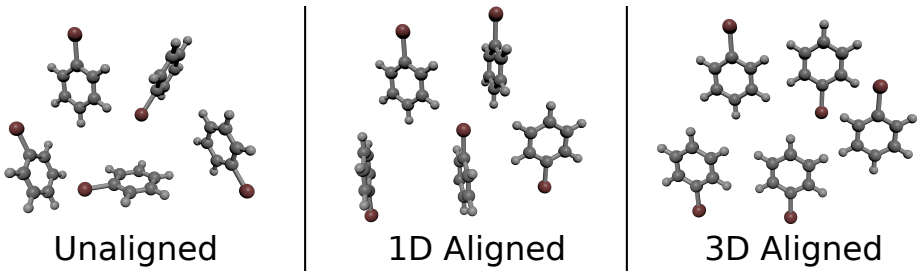

Figure 4.2: Different possible alignment schemes, using iodobenzene (IPh) as an example. See text for details.

fields is the technique used throughout this thesis. Broadly, LIA refers to the alignment of one (or more) molecular axes to one (or more) of the polarisation axes of a laser field. A detailed theoretical description is given below, and a thorough review of LIA theory and techniques is given by Stapelfeldt and Seideman [126].

4.1.1 Theory of Laser-Induced Alignment

The theoretical basis for LIA presented here follows the description of Friedrich and Herschbach [127, 128], drawing on ideas from Atkins and Friedman [129]. The following derivation first examines rotational dynamics in the absence of an external field, then derives expressions for the alignment of a linear molecule in a linearly polarised field, and for a symmetric top molecule in a circularly polarised field.

Rotational Dynamics in the absence of an external field

Under the Born-Oppenheimer and rigid-rotor approximations, the total Hamiltonian $\hat{H}$ can be written as a combination of rotational, vibrational, and electronic parts:

$$\hat{H} = \hat{H}_{\text{rot.}} + \hat{H}_{\text{vib.}} + \hat{H}_{\text{el.}} \tag{4.1}$$

Alignment is a rotational phenomenon, and generally a laser field used for alignment will not induce vibrations or electronic excitation in a molecule, thus we only consider the rotational Hamiltonian, $\hat{H}_{\text{rot.}}$, for the remainder of this derivation:

$$\hat{H}_{\text{rot.}} = \frac{\hat{J}_x^2}{2I_x} + \frac{\hat{J}_y^2}{2I_y} + \frac{\hat{J}_z^2}{2I_z} \tag{4.2}$$

Where $\hat{J}_i$ is the total angular momentum operator on the i^{th} axis of the molecule, and I_i is the moment of inertia around the i^{th} axis of the

molecule. Here the moments of inertia are defined on the molecule-fixed (x, y, z) axes (see page xi). For a linear molecule[2], the eigenstates $|\Psi\rangle$ that solve:

$$\hat{H}_{\text{rot.}} |\Psi\rangle = E_{\text{rot.}} |\Psi\rangle \tag{4.3}$$

are the spherical harmonics, $|\Psi\rangle = |JM\rangle$, where J is the total angular momentum, and M is the projection of the angular momentum onto the space-fixed Z axis. The energy $E_{\text{rot.}}$ of a specific rotational state is given by;

$$E_{\text{rot.}} = \boldsymbol{B} J(J+1) \tag{4.4}$$

Where the rotational constant $\boldsymbol{B}$ is defined as $\hbar^2/2I$. The above equations give a picture of rotational dynamics in the absence of any external electric field.

Molecules in Electric Fields

We now consider the interaction of molecule with an electric field $\boldsymbol{E(t)}$. Defining the interaction with the field as $\hat{H}_{\text{field}}$, the total Hamiltonian $\hat{H}$ can be written as:

$$\hat{H} = \hat{H}_{\text{rot.}} + \hat{H}_{\text{field}} \tag{4.5}$$

Where $\hat{H}_{\text{field}}$ is defined as the response of the molecule to the electric field (dropping the time dependence of the field for clarity), given by :

$$\hat{H}_{\text{field}} = -\boldsymbol{\mu} \cdot \boldsymbol{E} \tag{4.6}$$

Where $\boldsymbol{\mu}$ is the total electric dipole moment. Neglecting hyperpolarisability and higher order interactions, this consists of both permanent and induced dipole terms:

$$\boldsymbol{\mu} = \boldsymbol{\mu_0} + \underline{\boldsymbol{\alpha}}_{\text{XYZ}} \cdot \boldsymbol{E} \tag{4.7}$$

Here $\boldsymbol{\mu_0}$ is the permanent dipole moment, and $\underline{\boldsymbol{\alpha}}_{XYZ}$ is the polarisability tensor of the molecule defined in the space-fixed coordinate system. Consider now the Hellman-Feynman equation (given by Eq. 4.8) linking the derivative of the energy of the system U with respect to a parameter P to the expectation value of the partial derivative of the Hamiltonian $\hat{H}$ with respect to P.

$$\frac{dU}{dP} = \left\langle \frac{\partial \hat{H}}{\partial P} \right\rangle \tag{4.8}$$

[2]Moments of inertia, $I_{\text{xx}} = I_{\text{yy}} = I$, $I_{\text{zz}} = 0$.

In our case, the parameter of interest is the electric field $\boldsymbol{E}$, and we can define $\hat{H}_{\text{field}}$ as the effective Hamiltonian. Differentiating Eq. 4.6, we can write:

$$\frac{dU}{d\boldsymbol{E}} = -\langle \boldsymbol{\mu} \rangle \tag{4.9}$$

If we now consider the Taylor expansion of the total energy U in the field around the the energy in the absence of the field U_0, we can write the following expression for the total energy U:

$$U = U_0 + \left(\frac{dU}{d\boldsymbol{E}}\right)_0 \boldsymbol{E} + \frac{1}{2}\left(\frac{d^2U}{d\boldsymbol{E}^2}\right)_0 \boldsymbol{E}^2 \tag{4.10}$$

Where third and higher order derivatives have been neglected. Comparing Eq. 4.9 and the derivative of Eq. 4.10, it is clear that:

$$\frac{dU}{d\boldsymbol{E}} = \left(\frac{dU}{d\boldsymbol{E}}\right)_0 + \left(\frac{d^2U}{d\boldsymbol{E}^2}\right)_0 \boldsymbol{E} = -\langle \boldsymbol{\mu} \rangle \tag{4.11}$$

Comparing Eq. 4.11 with Eq. 4.7, the terms in Eq. 4.11 can be written as:

$$\left(\frac{dU}{d\boldsymbol{E}}\right)_0 = -\boldsymbol{\mu_0} \qquad\qquad \left(\frac{d^2U}{d\boldsymbol{E}^2}\right)_0 = -\boldsymbol{\alpha} \tag{4.12}$$

The total energy of the system U (given by Eq. 4.10) can then be written as:

$$U = U_0 - \boldsymbol{\mu_0} \cdot \boldsymbol{E} - \frac{1}{2} \cdot \boldsymbol{E} \cdot \underline{\boldsymbol{\alpha}}_{\text{XYZ}} \cdot \boldsymbol{E} \tag{4.13}$$

Where U_0 is the energy of the molecule in the absence of a field; and $\boldsymbol{\mu_0}$ and $\underline{\boldsymbol{\alpha}}_{\text{XYZ}}$ are defined as in Eq. 4.7. The polarisability tensor $\underline{\boldsymbol{\alpha}}_{\text{XYZ}}$ is defined in the space-fixed frame, however it is more natural to define the polarisability tensor in molecule-fixed coordinates, $\underline{\boldsymbol{\alpha}}_{\text{xyz}}$. The two can be related via transformation with the direction cosine matrix $\boldsymbol{\Phi}$ [130]. The transformation from the molecular to the space-fixed frame is given by:

$$\underline{\boldsymbol{\alpha}}_{\text{XYZ}} = \boldsymbol{\Phi^{-1}} \cdot \underline{\boldsymbol{\alpha}}_{\text{xyz}} \cdot \boldsymbol{\Phi} \tag{4.14}$$

The total energy can therefore be written as:

$$U = U_0 - \boldsymbol{\mu_0} \cdot \boldsymbol{E} - \frac{1}{2} \cdot \boldsymbol{E} \cdot \boldsymbol{\Phi^{-1}} \cdot \underline{\boldsymbol{\alpha}}_{\text{xyz}} \cdot \boldsymbol{\Phi} \cdot \boldsymbol{E} \tag{4.15}$$

This expression can now be divided into the energy in the absence of a field U_0, which is simply the rotational energy $U_0 = E_{\text{rot.}} = \boldsymbol{B}J(J+1)$. The remaining two terms arise from interaction with the field, so can both

be treated as arising from the $\hat{H}_{\text{field}}$ term. The energy resulting from this term, V, is therefore given by:

$$V = -\boldsymbol{\mu_0} \cdot \boldsymbol{E} - \frac{1}{2} \cdot \boldsymbol{E} \cdot \boldsymbol{\Phi^{-1}} \cdot \underline{\boldsymbol{\alpha}}_{\text{xyz}} \cdot \boldsymbol{\Phi} \cdot \boldsymbol{E} \tag{4.16}$$

If we consider that $\boldsymbol{E}$ is the electric field of an arbitrarily polarised laser pulse, defined as propagating along the space-fixed Y axis, such that:

$$\boldsymbol{E(t)} = \mathrm{e}^{(i2\pi ft)}[E_{\text{Z}}(t)\hat{\mathbf{Z}} + E_{\text{X}}(t)\hat{\mathbf{X}}\mathrm{e}^{i\psi}] \tag{4.17}$$

Where f is the frequency of the carrier wave, $E_{\text{i}}(t)$ is the envelope of the field along axis i, ψ is the phase between the two components of the field, and $\hat{\mathbf{Z}}$ and $\hat{\mathbf{X}}$ are unit vectors along the X and Z axes respectively. Provided that the carrier wave varies much faster than the field envelope ('slowly-varying envelope approximation'), then the first term in Eq. 4.16 averages out to zero over many optical cycles. This is true for all alignment laser fields used in this work. Now including the time dependence of the field, we are left with the time-dependent interaction with the field $V(t)$:

$$V(t) = -\frac{1}{2} \cdot \boldsymbol{E(t)} \cdot \boldsymbol{\Phi^{-1}} \cdot \boldsymbol{\alpha}_{\text{xyz}} \cdot \boldsymbol{\Phi} \cdot \boldsymbol{E(t)} \tag{4.18}$$

Up until now the discussion of the interaction with the molecular field has been entirely general. However, we will restrict analysis to two cases: firstly, a linear molecule in a linearly polarised field; and secondly, a symmetric top molecule in a circularly polarised field.

Linear Molecule, Linearly Polarised Field

We now consider the case where the applied laser field is linearly polarised and the molecule is linear. Under the coordinate system defined on page xi, this corresponds to a molecule with polarisability elements[3] parallel and perpendicular to the molecule-fixed z axis: $\alpha_{\text{zz}} = \alpha_{\parallel}$, and $\alpha_{\text{xx}} = \alpha_{\text{yy}} = \alpha_{\perp}$. The laser field defined in Eq. 4.17 is linearly polarised along Z and thus has parameters $E_{\text{X}}(t) = 0$, $E_{\text{Z}}(t) = E_0(t)$, such that it can be expressed as:

$$E(t) = E_0(t)\cos(2\pi ft)\hat{\mathbf{Z}} \tag{4.19}$$

The space-fixed and molecule-fixed coordinate systems are shown in Fig. 4.3. The direction cosine matrix $\boldsymbol{\Phi}$ depends on the three Euler angles

[3]The full polarisability of a molecule is given by a tensor, $\underline{\boldsymbol{\alpha}}$, where each element α_{ij} refers to the polarisability of the medium along i by a field polarised along j. The non-diagonal terms of the tensor (where $i \neq j$) are zero for all cases considered here.

(ϕ, θ, χ). The whole matrix is composed of three separate rotations such that:

$$\mathbf{\Phi}(\phi, \theta, \chi) = \mathrm{R_Z}(\phi)\mathrm{R_N}(\theta)\mathrm{R_z}(\chi) \tag{4.20}$$

Where each matrix $\mathrm{R_I}(i)$ refers to a rotation around axis I by angle i. The axis N is defined as the 'line of nodes', and refers to the common perpendicular of z and Z (such that $\mathrm{N} = \mathrm{z} \times \mathrm{Z}$). For a linear molecule, rotation around the axis of the molecule z doesn't change the polarisability, and we can therefore neglect the angle χ. Thus, our direction cosine matrix $\mathbf{\Phi}$ depends only on the angles ϕ and θ, where θ is defined as the angle between the z and Z axis, and ϕ is defined as the angle from the X axis to the projection of the z axis on the XY plane.

Applying these rotations to the polarisability tensor $\underline{\boldsymbol{\alpha}}_{\mathrm{xyz}}$ and working through the algebra results in the following expression for the potential energy of the molecule in the electric field.

$$V(t) = -\frac{1}{4}E_0^2(t)[(\alpha_\parallel - \alpha_\perp)\cos^2(\theta) + \alpha_\perp] \tag{4.21}$$

The resultant potential only depends on the angle between the space-fixed Z axis and molecule-fixed z axis, θ, and the polarisability anisotropy $(\alpha_\parallel - \alpha_\perp)$. An additional factor of $1/2$ has been introduced due to averaging over the electric field[4]. The resultant potential is plotted next to the coordinate system in Fig. 4.3. It is clear from Fig. 4.3 that the minimum energy is reached at $\theta = (0, \pi)$. Therefore the molecular z axis will become aligned to the polarisation axis. This is true provided that $\alpha_\parallel > \alpha_\perp$, which is true for all linear molecules.

The above derivation is only strictly valid for linear molecules in linearly polarised laser fields, which can be used to confine the most polarisable molecular axis (MPA) of a linear molecule, as seen. However, analogous arguments apply to non-linear molecules, as the laser field will always align the MPA to the polarisation direction. In the case where there are multiple axes that are equally polarisable (multiple MPAs), and one LPA (e.g. in benzene), then provided that at least one of the MPAs is parallel to the polarisation direction, then the potential is at a minimum.

Symmetric Top Molecule, Circularly Polarised Field

We now consider the case of a symmetric top molecule in a circularly polarised laser field. The molecule is defined as having its symmetric top axis (unique moment of inertia) as being aligned along y, resulting

[4]The RMS value of $A\cos^2(x)$ is $A/2$.

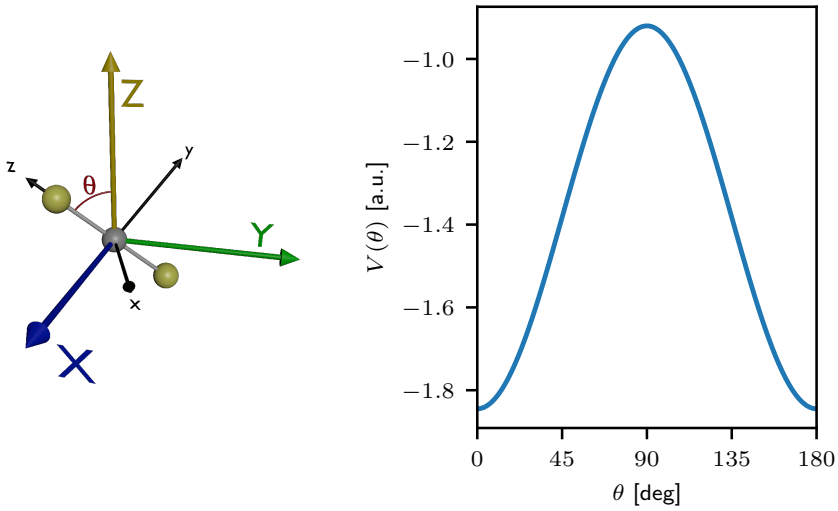

Figure 4.3: Left: Schematic of the coordinate systems used in the above derivation. Space-fixed (X, Y, Z) are shown in colour, with molecule-fixed (x, y, z) coordinates shown in black. The angle θ between the z and the Z axis is illustrated. Right: an example potential $\hat{V}(\theta)$ plotted for an OCS molecule with typical laser parameters. The alignment field is polarised along Z.

in polarisability elements $\alpha_{yy} = \alpha_{\parallel}$, and $\alpha_{xx} = \alpha_{zz} = \alpha_{\perp}$. In keeping with the coordinate systems defined on page xi, we define our laser field as being circularly polarised in the XZ plane. This gives the parameters $E_Z(t) = E_X(t) = E_0(t)$, and the phase between the two components $\psi = \pi/2$. This allows the electric field to be written as:

$$\boldsymbol{E(t)} = \mathrm{e}^{(i2\pi ft)}[E_0(t)\hat{\mathbf{Z}} + E_0(t)\hat{\mathbf{X}}\mathrm{e}^{(i\pi/2)}] \tag{4.22}$$

The space-fixed and molecule-fixed coordinate systems are shown in Fig. 4.4. The direction cosine matrix is now defined as $\mathbf{\Phi} = \mathrm{R_Y}(\phi)\mathrm{R_N}(\theta)\mathrm{R_y}(\chi)$, and the line of nodes N is now defined as the common perpendicular of y and Y ($\mathrm{N} = \mathrm{y} \times \mathrm{N}$). As before, the rotation around the y axis will not change the polarisability of the molecule, so rotation around χ can be discounted. This leaves the matrix $\mathbf{\Phi}$ again dependent only on ϕ and θ, where now θ is defined as the angle between the y and Y axes, and ϕ is defined as the angle from the X axis to the projection of the y axis on the XZ plane.

Applying these rotations as previously results in the following ex-

pression for the potential energy $V(t)$:

$$\hat{V}_{\text{circ.}}(t) = -\frac{1}{8}E_0^2(t)[(\alpha_\perp - \alpha_\parallel)\cos^2(\theta) + \alpha_\parallel + \alpha_\perp] \tag{4.23}$$

Again we see that the potential only depends on the angle θ between the space-fixed Y axis and the molecule-fixed y axis. The polarisability anisotropy $\Delta\alpha_{\text{circ.}} = \alpha_\perp - \alpha_\parallel$. There is an additional factor of $1/2$ as the circularity of the field must be averaged over[5]. This expression is consistent with that derived by Larsen *et al.* [131]. The resultant potential is plotted next to the coordinate system in Fig. 4.4. That this case of alignment in a circularly polarised field reduces to a 1D problem (only depending on θ) with a symmetric top molecule is very convenient, as it means that the alignment in a circularly polarised field can be simulated using the same programs that simulate 1D alignment of linear molecules in linear fields (see chapter 8). It is clear from Fig. 4.4 that the potential

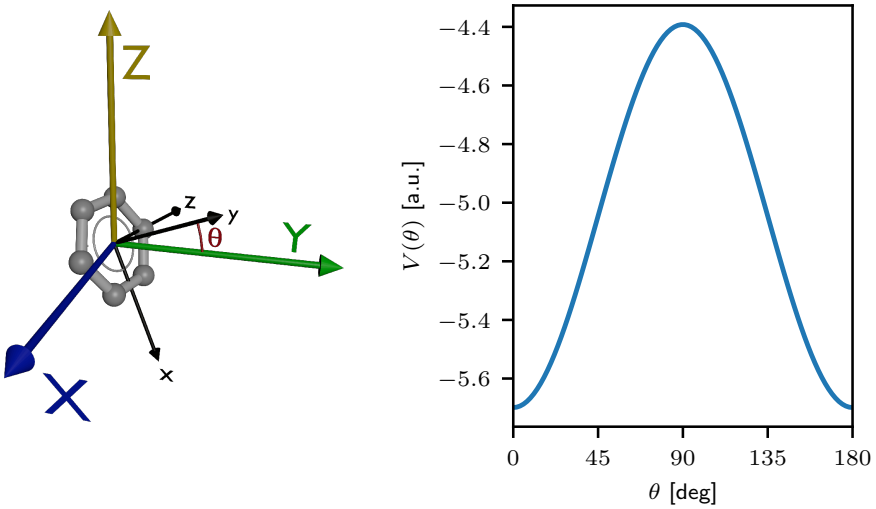

Figure 4.4: Left: Schematic of the coordinate systems used in the above derivation, with the space-fixed frame shown in colour and the molecular frame axes shown in black. The angle θ between the y and the Y axis is illustrated. Right: $\hat{V}(\theta)$ plotted for the benzene molecule with typical laser parameters. The alignment field is circularly polarised in the XZ plane.

is at a minimum when $\theta = (0, \pi)$. This can be interpreted as either the

[5]This can naively be imagined as the spreading of available electric field strength over two polarisation axes.

most polarisable plane (MPP) of the molecule aligning to the polarisation plane; or equivalently as the LPA aligning to the propagation direction of the laser field. Aligning a linear molecule with a circularly polarised field will result the MPA freely spinning in the polarisation plane.

It should be noted that this extension to symmetric top molecules where the resultant potential is dependent only on one angle (θ) is a special case that only applies for circularly polarised fields. In an elliptically polarised field, the alignment will depend on two angles, so cannot be reduced to the 1D problem as shown here.

4.1.2 Adiabatic Alignment

Until now we have not considered the specifics of the pulse envelope $E_0(t)$. In practice, it will (generally) be a Gaussian pulse envelope, and the pulse duration τ_{Align} (FWHM of the intensity $I(t)$, defined as $I(t) = E(t)^2$) will affect the alignment dynamics. Alignment can either be induced by a long or a short (relative to the rotational period $\tau_{\text{Rot.}}$ of the molecule being aligned) laser pulse. Alignment induced by a long pulse ($\tau_{\text{Align}} > \tau_{\text{Rot.}}$) is referred to as 'adiabatic alignment'; whereas alignment induced by a short pulse ($\tau_{\text{Align}} < \tau_{\text{Rot.}}$) is referred to as 'impulsive alignment' or 'non-adiabatic alignment'. All the work described in this thesis was done using adiabatic alignment, so impulsive alignment is not discussed further here.

Adiabatic alignment is achieved using a laser field that turns on much more slowly than the characteristic rotational period of the molecule. Simplistically, this can be thought of as 'dragging' the molecule into alignment as the field grows in intensity, with the best alignment achieved at the peak of the field, followed by a decrease in alignment as the field turns off. There is no persistent alignment after the field has passed.

Quantum mechanically, the eigenstates of the field-free Hamiltonian $|JM\rangle$ (see Eq. 4.3) are adiabatically transferred to a series of aligned pendular states $|\tilde{J}M\rangle$. The M quantum number is preserved during interaction with the laser, but J is not. However, if the laser field is turned on smoothly and slowly, then the energy ordering of the states $|\tilde{J}M\rangle$ is the same as the ordering of the field-free states $|JM\rangle$. Therefore, the lowest energy field-free states will be transferred to the lowest energy pendular states. The best alignment is observed when the lowest energy pendular states are occupied, which can be seen on Fig. 4.3 and Fig. 4.4 - lower energies mean the molecule resides deeper in potential minima, and is therefore more well aligned. Thus, it is imperative to have a cold ($T < 1\,\text{K}$) ensemble of molecules to get the strongest alignment. In this work, strongly chirped 800 nm pulses with $\tau_{\text{Align}} = 160\,\text{ps}$ are used to reach the adiabatic

regime.

4.1.3 Measuring Alignment

As may be expected based on the preceding discussion, a convenient observable for characterising the degree of alignment is the angle θ, the angle between a space-fixed axis and the molecule-fixed axis. Specifically, the observable used is $\langle \cos^2 \theta_{2D} \rangle$; that is, the expectation value of $\cos^2(\theta_{2D})$, where θ_{2D} is the projection of the angle θ onto a 2D imaging detector, as the full 3D ion distribution is typically not measured. A perfectly aligned ensemble of molecules ($\theta_{2D} = (0, \pi)$), gives a value of $\langle \cos^2 \theta_{2D} \rangle = 1$. A perfectly anti-aligned ensemble of molecules ($\theta_{2D} = \pi/2$) gives a value of $\langle \cos^2 \theta_{2D} \rangle = 0$. An unaligned ensemble of molecules (θ_{2D} is randomly distributed) gives $\langle \cos^2 \theta_{2D} \rangle = 0.5$.

Practically, this angle is measured via Coulomb Explosion Imaging, and projecting the resulting ion fragments onto the 2D detector. This is explored in detail in the following section.

4.2 Coulomb Explosion Imaging

Coulomb Explosion Imaging (CEI) is a standard technique by which we probe aligned molecules in Femtolab. It can be subdivided into two parts: the Coulomb explosion itself, and the imaging of the resulting fragments.

4.2.1 Coulomb Explosion

Coulomb explosion is the process that occurs when a molecule is rapidly (relative to the timescale of nuclear motion - so in $<$1 ps) multiply ionised, such that a highly charged molecular cation is produced. This cation rapidly fragments due to the Coulombic repulsion, and this fragmentation is referred to as a 'Coulomb explosion'. Coulomb explosion was first achieved using thin foils, where a beam of molecular ions are fired at a thin foil at high speed. The impact of the ion with the foil strips off the valence electrons of the ion [132, 133]. The nascent (multiply charged) molecular ion then undergoes Coulomb explosion. Coulomb explosion can also be induced by intense radiation sources; for example via Auger cascades [134], or using strong-field ionisation [111, 135]. Methods using such radiation sources are also advantageous as experiments can be easily synchronised to the arrival time of the radiation, allowing control of timing. Coulomb explosion induced by strong-field ionisation is the method most commonly used in Femtolab as a probe, and will be discussed further

here. A recent review of Coulomb explosion techniques was provided by Yatsuhashi and Yakashima, and provides more detail and many different possible applications [136].

Coulomb Explosion via Strong Field Ionisation

When a molecule is exposed to very intense ($I \sim 1 \times 10^{14}\,\mathrm{W/cm^2}$) laser radiation, the electric field strength becomes comparable to the Coulomb force binding the nuclei and electrons. This can result in rapid multiple ionisation of the molecule, creating a highly charged cation of the parent molecule. The typical pulse duration used to induce Coulomb explosion is around 40 fs, which produces the very high intensity required. A pulse this short ensures that the explosion takes place on a timescale that is faster than that over which the nuclei in a molecule will typically move. A detailed discussion of the ionisation process is beyond the scope of this work, but an basic outline will be given here.

In the case where the energy of the ionising photons is much lower than the ionisation potential I_P of the molecule (i.e. the ionisation is non-resonant), there are three main mechanisms by which such strong-field ionisation can occur. These are illustrated in Fig. 4.5, and are (a) multiphoton ionisation, (b) tunnelling ionisation, and (c) over-the-barrier ionisation. In the 'weak-field limit' of strong field ionisation, simultaneous absorption of multiple photons overcomes the ionisation barrier (multiphoton ionisation - (a)). As the electric field strength increases, the molecular potential is distorted such that an electron can tunnel through the ionisation barrier (tunnelling ionisation - (b)). At very high field strengths, the molecular potential is so distorted that the electron is completely unbound and so escapes into the continuum (over-the-barrier ionisation - (c)). Which of these regimes dominate depends largely on the parameters of the electric field. For slowly oscillating strong fields (long wavelengths), the electron has time to tunnel through the barrier, so regimes (b) and (c) dominate. At shorter wavelengths and weaker fields, the field oscillates sufficiently fast that the tunnelling rate is substantially suppressed, so regime (a) dominates. The Keldysh parameter [137], γ, can give a quantitative insight into these processes:

$$\gamma = \frac{T_\mathrm{tunnel}}{T_\mathrm{osc.}} = \sqrt{\frac{I_p}{2U_p}} \tag{4.24}$$

Where $T_\mathrm{osc.}$ is the oscillation period of the laser field ($T_\mathrm{osc.} = {}^{2\pi}/_{\omega}$); T_tunnel is the time taken for an electron to tunnel through the field; I_p is the ionisation potential; and U_p is the ponderomotive energy, which is a mea-

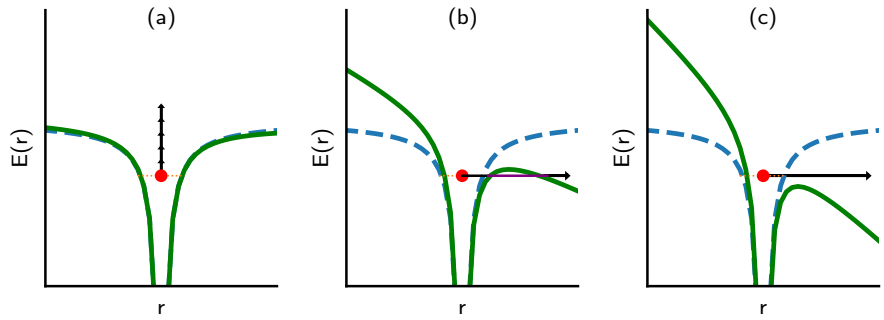

Figure 4.5: Sketches of different cases of strong field ionisation of a single electron. The field-free potential is shown in dashed blue, and the field-dressed potential in green, with the electron in red. (a) multiphoton ionisation, (b) tunnelling ionisation, (c) over-the-barrier ionisation.

sure of the average kinetic energy of an electron in the oscillating field. If $\gamma \gg 1$, then multiphoton ionisation dominates as the electron doesn't have time to tunnel into the continuum. Conversely, if $\gamma \ll 1$, the field is stronger and the electron can tunnel into the continuum.

A pleasant analogy for qualitatively understanding these processes is Albert Stolow's 'Bathtub Model': Imagining the molecular potential as a bathtub containing water (electrons), if the bathtub is rapidly tilted back and forth (high frequency fields), then water haphazardly spills out and the ionisation process is violent - multiphoton ionisation. Conversely, if the bathtub is gently tilted back and forth (low frequency fields), then water is gently spilled from each end of the bath, and the ionisation process is less violent - this is tunnelling or over-the-barrier ionisation. In general, the softer ionisation using lower frequency fields results in less fragmentation of ionised molecules, whereas multiphoton ionisation with higher frequency fields results in more fragmentation [138]. The majority of the work described herein is somewhere in between the regimes shown by (a) and (b) in Fig. 4.5. The ideas presented here will be returned to in chapter 10, where single ionisation of large fragile molecules is desired.

Having created a highly charged parent cation, it subsequently fragments due to Coulombic repulsion. Imaging the recoil directions of the fragments can provide information about the structure of the parent molecule, subject to axial recoil considerations (see subsection 4.2.3.

4.2.2 Ion Imaging

Ion imaging is the process of focussing ions onto a 2D detector such that an 'ion image' can be made. In this work, velocity-map imaging (VMI) is employed. Here, a series of three electrodes ('repeller', 'extractor', and 'ground') are used to produce a field that will focus ions (of the same mass) produced with a unique velocity (in the plane of the detector) onto a unique point on a 2D detector, independent of their position in the laser focus when ionised. The way this is set up in our laboratory, and specific electrodes used are discussed in chapter 6, with a general overview given here.

Ions are produced by focussed laser beams in a space between the repeller and extractor plates (the 'interaction region'). A voltage gradient of around $0.5\,\mathrm{kV\,cm^{-1}}$ is applied between the repeller and extractor plates, resulting in a field where the position at which the ions impinge on the detector is independent of the position at which they are ionised in the interaction region, and depends only on their velocity in the plane of the detector - this is the 'velocity-mapping' in VMI. The specific voltage ratio is discussed further in chapter 6. Other types of ion imaging are possible, such 'spatial-map imaging' (SMI) [139, 140], but are not used in this work and are not covered here. The third electrode is always grounded, to ensure that the accelerated ions fly in a field-free region where they diverge in the detector plane due to their initial velocity in the detector plane, and also diverge in time as heavy ions with a large mass-to-charge (m/z) ratio fly more slowly than lighter ions (flight time $t \propto \sqrt{m/z}$).

The voltages on the electrodes are chosen depending on the energy of the desired ions for imaging - very fast ions require a high voltage on the repeller to focus them onto the screen such that they don't miss and fly past the edge of the detector. Conversely, if one is looking at slow, large ions, then using a high extraction voltage is not ideal as the slower ions will be focussed into the middle of the detector where there is lower resolution. Therefore lower voltages are often used when imaging of slow species is desired, due to the greater magnification of the low energy parts of the image. The exact voltages used are quoted in each respective experimental chapter.

Strictly speaking, the term 'velocity-map imaging' applies only to ions of the same mass. To be more precise, ions with the same kinetic energy are focussed onto the same position on the detector, regardless of their positions when ionised - this allows a wide variety of different ion masses (or electrons) to be imaged. This can be simply understood by considering two different ions, both produced with the same kinetic

energy, but with different masses. The ions will both fly towards the detector, but the heavier ion has a longer flight time. Both ions diverge away from the center of the detector and towards the edge. The lighter ion has a higher velocity, so initially diverges more, but has a shorter flight time. In contrast, the heavier (slower) ion, diverges less initially, but flies for a longer time (and diverges over the flight) such that it will eventually hit the same position on the detector as the lighter ion.

4.2.3 Axial Recoil

When a molecule fragments due to Coulomb explosion, the ionic fragments will recoil with specific velocities. The speed of the recoiling fragments is related to the magnitude of the electrostatic repulsion they feel from the surrounding fragments. The direction of the recoiling fragments is related to the momentum of all the other recoiling fragments. In a simple diatomic molecule, the two ionic fragments will recoil at 180° to each other due to momentum conservation, but in larger systems the recoil trajectories depend on the momenta of all other fragments.

The Axial Recoil Approximation (ARA) is the assumption that ionic fragments recoil along the bond they had to parent molecule prior to ionisation. This is generally the case for molecules with a substantial high-mass 'backbone' that the imaged fragments recoil from. Specifically, substituted benzenes (and their derivatives) are often observed to exhibit very good axial recoil, because the recoiling substituents (which are imaged) recoil from the benzene ring, which is heavy enough that the substituents tend to recoil along their original bond axes [57, 111, 112, 141]. When the ARA holds, a measurement of the emission angles of the recoiling fragments (relative to some space-fixed axis) provides a direct link to the angle of the molecular axes relative to that axis, so the obtainable information from an ion image is increased. Deviation from the ARA often renders ion images difficult to interpret, as then the emission angles of recoiling fragments do not reflect the orientation of their parent molecule. Non-Axial Recoil (NAR) is especially problematic when studying LIA using CEI, as measuring alignment from an ion image generally relies on the emission angles measured in the ion image giving an accurate measure of the molecular axis alignment.

Ionic fragments produced inside HeDs often show very high degrees of NAR, as the fragments scatter off the helium atoms as they exit the droplet, so the recoil velocities are distorted. This is a key experimental consideration and generally requires that the droplets used are as small as possible to minimise this effect. In many cases, it is possible to deconvolute

the effect of the NAR from covariance data [142]. This will be be more thoroughly explored later in section 5.4.

4.3 Summary

In this chapter the main experimental techniques used in the study of molecular complexes throughout this work have been discussed. LIA and CEI is a powerful combination that can reveal much about the structure and dynamics of a system, whilst retaining femtosecond time resolution. The resulting ion images from these techniques are analysed in a variety of different ways, which are detailed in chapter 5.

CHAPTER 5

Analysis of Ion Imaging Data

There are many techniques used throughout this thesis to analyse the data acquired from ion imaging experiments. They are detailed in this chapter so they can be easily referred to from the results chapters.

5.1 Covariance Analysis

Covariance analysis is a widely used technique molecular dynamics [111, 143–149], and is used extensively in this thesis. Firstly the mathematical groundwork of covariance analysis and covariance mapping will be outlined. Then the practical implementation of covariance mapping to ion detection experiments will be outlined. The writing of this section was greatly helped by correspondence with Dr Michael Burt, to whom I am grateful.

5.1.1 Mathematical Basis of Covariance Analysis

Statistically, covariance is simply a measure of the correlation between two or more random variables [150], and can be thought of as a generalising variance to multiple dimensions. The covariance $\mathrm{cov}(x, y)$ between two random variables, x and y, observed n times, is given by Eq. 5.1.

$$\mathrm{cov}(x, y) = \frac{1}{n}\sum_{i=1}^{n}(x_i - \bar{x})(y_i - \bar{y}) = \frac{1}{n}\sum_{i=1}^{n}(x_i y_i) - \bar{x}\bar{y} \qquad (5.1)$$

Where x_i is the i^{th} observation of variable x, and $\bar{x}$ is the expected value (mean) of variable x. In the case where $x = y$, the covariance

$\mathrm{cov}(x, y)$ is equivalent to the variance, i.e. $\mathrm{cov}(x, x) = \mathrm{var}(x)$. Equation 5.1 can equivalently be written using expectation values, as in Eq. 5.2.

$$\mathrm{cov}(x, y) = \langle xy \rangle - \langle x \rangle \langle y \rangle \tag{5.2}$$

Eq. 5.2 is the most commonly used expression for the covariance between two variables x and y. Considering the terms in Eq. 5.2, the first term, $\langle xy \rangle$ is a measure of how often both variables are observed simultaneously ('in coincidence') - and provides an effective measure of how often the events are observed to be correlated. However, it is important to note that this may include instances where the two variables appear to be correlated but actually are not ('false coincidences'). This can happen, for example, if the variables are both are measured in such a way as to render correlated and uncorrelated observations indistinguishable from one another. The second term, $\langle x \rangle \langle y \rangle$, is a measure of how often both variables are observed alone (not in coincidence), and as such estimates the number of these false coincidences. Subtracting this term from the first term corrects for the spurious contribution the falsely correlated events make to the total covariance [151]. If the variables are measured in such a way that there are no false coincidences (i.e. $\langle x \rangle \langle y \rangle \to 0$), then $\mathrm{cov}(x, y) = \langle xy \rangle$, as all correlations measured are necessarily 'real correlations'. Furthermore, it is clear that if the two variables are uncorrelated (i.e. $\langle xy \rangle = \langle x \rangle \langle y \rangle$), then covariance is necessarily zero. These ideas will be returned to in the context of ion imaging experiments in subsection 5.1.2.

Covariances are immune to noise and random fluctuation in the desired signal, provided it is entirely uncorrelated from the processes of interest. To illustrate this, the following analysis by Zhaunerchyk *et al.* is reproduced with slight modification [151]. To simulate the contamination of a random variable x with some noise s_x, we can define x as in Eq. 5.3.

$$x = x_0 + s_x \tag{5.3}$$

Where x_0 is the pure random variable, without contaminating noise. Defining another variable y in an exactly analogous way, the covariance between these two variables can be defined simply as $\mathrm{cov}(x_0 + s_x, y_0 + s_y)$. Provided that the pure variable and the noise are independent, and using the fact that the expectation operator is linear, then the covariance is given by Eq. 5.4.

$$\mathrm{cov}(x, y) = \mathrm{cov}(x_0 + s_x, y_0 + s_y) = \mathrm{cov}(x_0, y_0) \tag{5.4}$$

Thus, the noise has no effect on the final covariance, provided it is uncorrelated with the process of interest. An important implication of this is that

any signal coming from a completely uncorrelated process will not affect the resulting covariance. For the case where the there is fluctuation/noise that is correlated with the processes of interest[1], then partial covariance analysis [146,147] can be used to remove the spurious noise contributions. Partial covariance analysis is not used in this work, and thus will not be explored further here.

It is instructive to now consider random variables x and y in more detail. Evidently, x and y must be governed by some probability distribution law, else the data would be exact, and there would be no need for covariance analysis. Quantitatively, the covariance between two variables is related to the second central moment μ_2 of the underlying probability distribution of the two variables. The second central moment of the distribution is the variance, so the covariance is meaningful provided that the variance is non-zero. To reiterate, if the variance is zero, the data is exact (no underlying distribution), and there is no need for covariance analysis. This is not especially interesting for the case of covariance between two variables, but it provides a useful framework for considering higher orders of covariance analysis. These are not used in this work, but are covered briefly here for completeness.

For a set of n random variables, the n-fold covariance is related to the n^{th} central moment of the probability distribution underlying the variables. Thus, if the n^{th} central moment is non-zero, the n-fold covariance is meaningful. Three-fold covariance is a technique that is used in ion imaging [144, 152], and the third central moment of a distribution is the skewness of the distribution, and thus three-fold covariance can only be used if the skewness of the underlying distribution is non-zero. For a Poisson distribution, the skewness is non-zero, so three-fold covariance can be applied. In contrast, for a Gaussian distribution, the skewness is zero, so three-fold covariance cannot be used. Photofragmentation processes tend to be governed by Poisson statistics, as the number of ion fragments produced in an acquisition cycle generally does not depend on how many were produced in the previous cycle, so three-fold covariance can be applied to ion imaging data.

An illustrative way to picture variances and covariances for m random variables is to construct an $m \times m$ variance-covariance matrix, $\mathbf{S}$,

[1] An example of this in chemical dynamics would be fluctuating laser power affecting the number of events recorded per shot. This is generally a problem at large free-electron lasers, where the shot-to-shot power fluctuation can be severe. Within Femtolab, this is generally not the case, so partial covariance analysis is not used.

shown in Eq. 5.5[2].

$$\mathbf{S} = \begin{bmatrix} \mathrm{cov}(x,x) & \mathrm{cov}(x,y) & \cdots & \mathrm{cov}(x,m) \\ \mathrm{cov}(y,x) & \mathrm{cov}(y,y) & \cdots & \mathrm{cov}(y,m) \\ \vdots & \vdots & \ddots & \vdots \\ \mathrm{cov}(m,x) & \mathrm{cov}(m,y) & \cdots & \mathrm{cov}(m,m) \end{bmatrix} \tag{5.5}$$

The central diagonal of the matrix **S** corresponds to the variance of each variable, and the off-diagonal elements are the covariances. The matrix is necessarily symmetric about the central diagonal. Representation and analysis of the covariances in this way is generally referred to as 'covariance mapping', and it can be applied to a number of different experimental observables, as will be shown in subsection 5.1.2.

5.1.2 Application to Ion Detection Experiments

The application of covariance mapping to ion detection experiments was pioneered by Frasinski *et al.* [152]. In the first instance, covariance mapping was applied to ToF spectra, to reveal correlations between different mass peaks in a given ToF spectrum. To illustrate the utility of correlation analysis to chemical dynamics, consider a hypothetical molecule AB undergoing ionisation and subsequent fragmentation, some possible fragmentation channels are shown below (adapted from [152]).

$$\begin{aligned} \mathrm{AB}^+ &\longrightarrow \mathrm{A}^+ + \mathrm{B} \\ \mathrm{AB}^+ &\longrightarrow \mathrm{A} + \mathrm{B}^+ \\ \mathrm{AB}^{2+} &\longrightarrow \mathrm{A}^+ + \mathrm{B}^+ \end{aligned}$$

In a standard ion detection experiment, the neutral atoms A and B are undetected, with only the A^+ and B^+ ions being detected. Merely detecting (for example) an A^+ ion doesn't reveal much information about the fragmentation dynamics, as the A^+ ion could have been born out of either the monovalent fragmentation of AB^+, or the divalent fragmentation of AB^{2+}. However, by doing covariance analysis between the two ions, one can see which fragmentation event they came from. If there is a non-zero covariance between the two ions, then they were produced from the same fragmentation event, and must have come from the fragmentation of AB^{2+}. Conversely, if no covariance is visible (but both ions are still detected), then they must have come from the fragmentation of

[2]It is important to note that we are not calculating the m-dimensional covariance between m different random variables, but are calculating a matrix of different two-fold covariance values between different pairs of the m variables.

AB^+. Herein lies the beauty of correlation analysis, as it reveals powerful information that is not revealed in the raw data.

Note that up until now in the discussion of this hypothetical system, there has not been a clear distinction made between 'correlation analysis', 'coincidence analysis', and 'covariance analysis'. 'Correlation analysis' is an umbrella term incorporating both coincidence and covariance analysis. The distinction between the latter two was alluded to in subsection 5.1.1, and lies in the number of fragmentation events of a given system occuring *per experimental acquisition cycle*[3].

In 'coincidence analysis', there is necessarily a maximum of one fragmentation event occurring per acquisition cycle, and generally far fewer than this in typical conditions [134, 153]. This ensures experimentally that any events that are detected as coming from the same fragmentation event do actually come from the same fragmentation event, and the degree of correlation can be counted simply by counting the number of ions detected in coincidence. However, in some experiments, such as gas-phase imaging experiments with high target densities, or high laser powers, it is impractical to have to ensure that there is only one fragmentation event per every 10-100 acquisition cycles. In such experiments, there are multiple fragmentation events occurring per acquisition cycle, and as such the correlations measured are masked by 'false coincidences', ions detected in the same acquisition cycle that arise from different fragmentation events. Under this regime, covariance analysis must be used to subtract off and correct for the contribution of these false coincidences, as described mathematically in subsection 5.1.1. Provided that the number of acquisition cycles sampled is sufficiently large, (and the underlying distribution of events is appropriate), then covariance analysis will completely correct for the false coincidences and reveal the desired correlations in the data[4]. Additionally, to reiterate arguments from subsection 5.1.1, it is clear that if covariance analysis is applied to data taken under the low count rate 'coincidence' regime, then covariance analysis simply reduces

[3] In this context, an acquisition cycle is generally a single laser shot, or a single camera frame.

[4] A note on nomenclature. The term 'false covariance' is commonly, and erroneously, used to describe any obviously false correlation feature in a covariance map. If a covariance algorithm is applied correctly, and the number of acquisition cycles is sufficient, then covariance analysis will always correct for any false correlation. Thus, a covariance cannot be 'false' if it has been correctly calculated. False correlation arises in covariance maps because there are insufficient statistics to completely remove the contribution of falsely correlated events. 'False correlation caused by insufficient data to allow the covariance map to remove false coincidences and converge to the correct result' would be a more correct term, although sadly precision has given way to brevity.

down to coincidence analysis. This is convenient, as it means that the same covariance algorithms can be applied to any dataset (recorded with a high or low count rate) and used to reveal the correlations within.

The experimental observables that covariance mapping can be applied to are varied, and include ToF peaks [145]; pixels in an ion image [111, 143]; the emission angles of ion fragments [154]; or the emission radii of ion fragments [96]. In all cases, the fundamental technique is the same, and is to construct a variance-covariance matrix of the desired observable. Throughout this work, covariance maps correlating the emission angles of ion fragments ('angular covariance maps') are used to analyse experimental data. As such, this is the example that will be used in the following discussions. To first construct an angular covariance map from an ion image, the image is first segmented into different bins of a pre-defined angular width ϕ over its full 360° range, such that there are $^{360}/_{\phi}$ separate bins. These bins can either run over all radii, from the center of the image (radius $r = 0$) to the edge ($r = 225.5$)[5], or over a pre-defined radial range, $r_1 < r < r_2$, as desired. Each angular bin is integrated over the desired radial range. The resulting variance-covariance matrix $\mathbf{S_{Angular}}$, with m angular bins, is given by Eq. 5.6.

$$\mathbf{S_{Angular}} = \begin{bmatrix} \mathrm{cov}(\theta_1,\theta_1) & \mathrm{cov}(\theta_1,\theta_2) & \cdots & \mathrm{cov}(\theta_1,\theta_m) \\ \mathrm{cov}(\theta_2,\theta_1) & \mathrm{cov}(\theta_2,\theta_2) & \cdots & \mathrm{cov}(\theta_2,\theta_m) \\ \vdots & \vdots & \ddots & \vdots \\ \mathrm{cov}(\theta_m,\theta_1) & \mathrm{cov}(\theta_m,\theta_2) & \cdots & \mathrm{cov}(\theta_m,\theta_m) \end{bmatrix} \tag{5.6}$$

The resulting matrix is also only defined within the aforementioned radial range, but that is omitted from Eq. 5.6 for clarity. Each element $\mathrm{cov}(\theta_a, \theta_b)$ is the covariance between emission angles θ_a and θ_b, defined as in Eq. 5.7.

$$\begin{aligned} \mathrm{cov}(\theta_a,\theta_b) &= \frac{1}{N_{\mathrm{cycles}}} \sum_{i=1}^{N_{\mathrm{cycles}}} (\theta_{ia} - \bar{\theta_a})(\theta_{ib} - \bar{\theta_b}) \\ &= \langle \theta_a \theta_b \rangle - \langle \theta_a \rangle \langle \theta_b \rangle \end{aligned} \tag{5.7}$$

Where N_{cycles} is the total number of acquisition cycles over which the data is recorded. To reiterate for clarity, the term $\langle \theta_a \theta_b \rangle$ is a measure of how often (on average) ion hits in angular bins θ_a and θ_b are detected in the same acquisition cycle, and the term $\langle \theta_a \rangle \langle \theta_b \rangle$ is a measure of the spurious uncorrelated contributions that should be subtracted. An example of an angular covariance map and the ion image it was calculated from is shown

[5] In our experiment, the image dimensions are 451 pixels by 451 pixels.

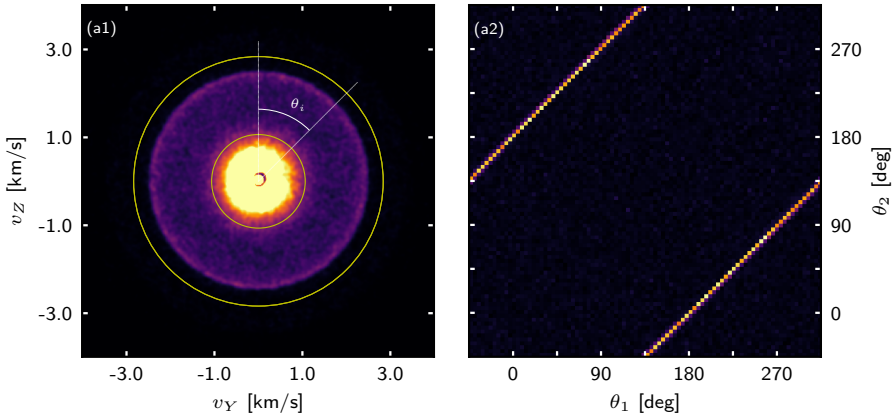

Figure 5.1: (a1) An ion image with (a2) corresponding angular covariance map to illustrate the angular covariance technique. The angular covariance map is calculated using ions between the two yellow circles marked in (a1). The angle θ_i is defined as shown, overlaid in white. See appendix B for experimental details.

in Fig. 5.1. A final point to note is that the matrix plotted in Fig. 5.1 is the transpose of $\mathbf{S_{Angular}}$; this is done such that the lower left corner of the matrix is element (θ_1, θ_1), to aid interpretation.

Figure 5.1 (a1) shows an ion image, with the corresponding angular covariance map shown in Fig. 5.1 (a2). This serves just to illustrate the angular covariance mapping technique, so the experimental details will not be covered here (see appendix B), suffice to say that this is the break up of a system into two ions of equal mass and charge. The angular covariance map shows a clear signal at $\theta_1 = \theta_2 + 180°$, which means that when one ion is detected at an angle of $\theta_1 = 0°$, then another ion is detected in the same acquistion cycle at an angle of $\theta_2 = 180°$, entirely consistent with the two-body break up expected. The signal is spread over all possible angles, suggesting that the molecular system can freely rotate in the detection (YZ) plane. Of this information, we can only tell that the system is free to rotate from the ion image (a1), but the covariance map (a2) also shows that the ions giving rise to the signal in (a1) are two ions produced in coincidence. This is a limited example of the capabilities of the covariance mapping technique, which will be applied to more ambitious examples in subsequent chapters, but serves to provide a reference as to how the maps are interpreted.

5.2 Kinetic Energy Release of Clusters

In VMI, ions (of the same mass) produced with the same velocity in the detector plane are mapped onto the same point on a 2D detector. Ions with a higher velocity in the detector plane are mapped to larger radii on the image, and ions with zero velocity in the detector plane are mapped into the center of the image. An equivalent way to state this is that all ions with the same *speed* will be mapped onto the same *radius* on the detector, if one integrates over all possible emission angles to consider speed rather than velocity. The process of VMI has been discussed in detail in subsection 4.2.2, and the calibration of the spectrometer (with the exact relation between the radius an ion will hit and its speed in the detector plane) is given in appendix A. That ions with different speeds are mapped to different radii can be used to isolate ion signals arising from different explosion channels.

For example, if during Coulomb explosion of molecule AB, an ion A^+ can be produced with two possible partner fragment, B^+, and B^{2+}, then the A^+ ion would be produced with two distinct speeds caused by differing degrees of Coulombic repulsion with the differently charged partner fragments. The A^+ ions formed with B^{2+} would have the highest speed, while the A^+ ions formed with B^+ would have the lowest. One can then select for ions produced with a specific partner ion by selecting specific radii, such that (for example) an angular covariance map can be calculated using just ions that originate from a specific explosion channel.

A natural extension of this technique when considering clusters of molecules is to consider how the size of the cluster will affect the speed of the nascent ions when the cluster is Coulomb exploded. To this end, we consider a cluster of N molecules, in which all molecules are ionised during a Coulomb explosion. Modelling each ion as a point charge, at the instant of ionisation, the electrostatic potential energy $U(N)$ stored within the cluster is given by Eq. 5.8.

$$U(N) = \frac{1}{2}\sum_{i=1}^{N} q_i \sum_{i=1}^{i\neq j} \frac{1}{4\pi\epsilon_0}\frac{q_i q_j}{r_{ij}} \tag{5.8}$$

Where q_i is the charge on ion i, r_{ij} is the separation between two ions i and j, and ϵ_0 is the vacuum permittivity. After the instant of ionisation the ions will gain kinetic energy E_k as they mutually repel due to Coulombic repulsion. Assuming that the potential energy $U(N)$ is completely converted to kinetic energy, and is equally shared between the N ions, their resultant kinetic energy can be used to calculate their

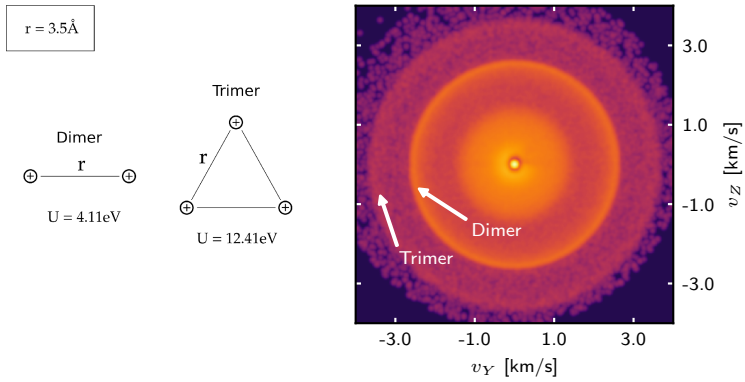

Figure 5.2: Left: example clusters of two (dimer) and three (trimer) ions, with their stored electrostatic potential shown beneath each cluster. Right: an ion image containing signals from such clusters, annotated with white arrows.

speed after ionisation. Figure 5.2 shows two example structures of ions with their stored electrostatic potential energy annotated beneath them (left panel); together with an example ion image containing signals from both structures (right panel).

If the stored potential energy in each cluster (left panel) is completely transformed into kinetic energy and equally shared between each ion in the cluster, then each ion gains 2.05 eV in the dimer structure, and 4.13 eV in the trimer structure. Under normal experimental conditions, for an ion of mass 76 Da, these kinetic energies would result in a speeds of around $2.3\,\mathrm{km\,s^{-1}}$ (dimer) and $3.2\,\mathrm{km\,s^{-1}}$ (trimer). The example ion image (right panel - see appendix B for experimental details) shows clear signatures at these speeds, annotated with white arrows. Thus it is clear that ions from different sizes of cluster may be differentiated in a velocity-mapped image if the ions from each different cluster are produced with different amount of kinetic energy. In addition, it is important to note that an ion produced via ionisation of a monomer (i.e. one that is not in a cluster, such that $r \to \infty$) will be produced with zero kinetic energy, and will therefore be mapped into the centre of the ion image, this is visible as the intense central spot in the ion image shown in Fig. 5.2. A final point to note is that in the example shown in Fig. 5.2, the clusters can freely rotate in space prior to ionisation, so a 3D sphere of ions is produced which is then projected onto the detector plane. Accordingly, there will be some ions from clusters that are mapped to the central parts of the image,

but the projection means that the majority will be mapped to the edges (this is clearly visible on the image) - more details about this are given in section 5.3[6]. To summarise, it is clear that ions resulting from ionisation (and Coulomb explosion) of clusters can be differentiated from ions resulting from ionisation of monomers based on their emission radii; in the same way that ions from different sizes of cluster can be differentiated.

5.3 Projection of Ion Emission Angles

Focussed laser beams are used to ionise molecules inside our VMI spectrometer, and the ions are then focussed towards a two-dimensional detector. At the instant of ionisation, the nascent cations mutually repel due to Coulombic repulsion and, spread out in a three-dimensional distribution known as a Newton sphere. This distribution would be spherical provided that the molecules are oriented isotropically prior to ionisation, and if the ionisation process is equally selective for molecules in any given orientation. In practice, the distribution may be non-spherical if the molecules are distributed anisotropically (e.g. if they are aligned), or if the ionising laser is polarised such that molecules lying at a specific orientation to the polarisation axis are preferentially ionised. The resulting 3D distribution is then projected onto the 2D detector by the spectrometer, and is necessarily 'crushed' flat during the projection. The 3D distribution can be recovered in post-processing, such as by inverse Abel transforms [155], polar onion-peeling (POP) [156], or tomographic reconstruction [157, 158]; or it can be experimentally measured by techniques such as slice imaging [159, 160]. Throughout this thesis, 2D ion images are shown without any reconstruction of the 3D distribution, as it is not necessary to interpret the results (and often reconstruction algorithms are not applicable to data taken using aligned molecules). However, it is still instructive to consider the projection of a 3D sphere of ions onto a 2D detector, as this has important ramifications for the interpretation of experimental ion images.

The leftmost panel of Fig. 5.3 shows a 3D distribution of ion velocities, simulated to resemble a Newton sphere produced after a photofragmentation event. The projection of this 3D sphere onto a 2D screen is shown in the rightmost panel of Fig. 5.3. Despite the sphere being completely isotropic, the projection shows a 'bunching' of ions towards the edges of the projected circle. This is a well-documented consequence of

[6] If the clusters cannot freely rotate in space prior to ionisation (i.e. if they are aligned), then this effect is not seen, and very sharp rings with no ion signal inside the ring will be seen.

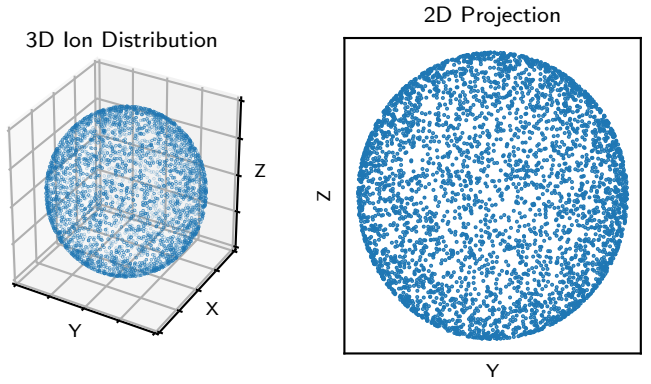

Figure 5.3: Left: a simulated isotropic 3D distribution of ion velocities, simulating a Newton sphere following a photofragmentation process. Right: the projection of the 3D velocity distribution onto a 2D screen.

the projection of a sphere onto a plane, but is of importance to ion-imaging experiments [130, 161], so is documented here for reference.

5.4 Deconvolution of Non-Axial Recoil

The Axial Recoil Approximation (ARA) was introduced in chapter 4. To reiterate, the ARA assumes that an ion fragment produced in a photofragmentation process recoils exactly along the the axis of the bond it formed to the parent molecule prior to fragmentation. If the ARA is valid, then the measurement of the emission angles of the ion fragments is a measurement of the alignment of the molecular axis (with respect to a space-fixed axis). Good axial recoil is important when the recoil velocities of ion fragments are used to interrogate the system of interest, such as when measuring the degree of LIA by measuring $\langle \cos^2 \theta_{2D} \rangle$. In this case, if the axial recoil is bad, then the measured degree of alignment will be lower than the true degree of alignment. The ARA is generally valid for diatomic systems, or systems with a sufficiently heavy 'backbone' for the imaged fragment to recoil from. Non-axial recoil (NAR) can occur if the fragmenting molecule vibrates during the fragmentation process, or if the charge distribution on the ionised parent molecule is asymmetric. Photofragmentation processes in HeDs suffer from especially bad NAR due to the scattering of the recoiling fragments off the helium atoms as the fragments exit the droplet [162]. The situation can be ameliorated by using heavier fragment ions, or smaller droplets, but sometimes neither of these approaches are applicable, and they cannot remedy the problem

completely. In this case, it has been shown that the effect of the NAR can be deconvoluted using the angular covariance map [142].

A detailed analysis of this technique is described in reference [142], and only an outline will be presented here to facilitate understanding of the analysis in chapter 8. The crux of the method relies on the fact that the two phenomena responsible for the broadening of a covariance signal in an angular covariance map are imperfect alignment, and poor axial recoil. Both of these phenomena affect the covariance map in different ways, and the contributions from each can be deconvoluted from one another via Fourier deconvolution. This allows the effect of the NAR to be removed, and the true degree of alignment extracted. This has been used to great effect in the measurement of alignment from molecules embedded in HeDs, where it was shown that excellent agreement with theory could be obtained when the non-axial recoil was deconvoluted [162]. This technique can be used provided that an angular covariance map is calculable, and additionally provides a measure of the best alignment measureable for a given degree of non-axial recoil. This is helpful in analysing the effect of different droplet sizes and different fragment ion observables.

5.5 Summary

Having established the experimental techniques used to record ion images, this chapter has documented some of the ways in which the resulting data is analysed. These analysis techniques will be referred back to throughout the remainder of this thesis. The next chapter details how the techniques used are realised physically, and forms the final introductory chapter before the presentationof results from chapter 7 onwards.

CHAPTER 6

Experimental Setup

The experiments described herein were all performed on the 'New Droplet Machine', designed and built by Dr. Ben Shepperson during his time in Femtolab [162]. Since its completion in 2015, this new He droplet machine has greatly increased the number of possible experiments we can undertake, compared to older HeD systems[1]. This machine is described in detail in section 6.1. To provide the intense light sources required for the experiments performed, an amplified Ti:Sapphire laser was used, presented in section 6.2. The specific optical setup used varies slightly between experiments - where there is a difference between the optical setup used and the optical setup presented here, it is documented in the relevant results chapter.

6.1 Helium Droplet Machine

The HeD machine on which all described experiments were performed consists of four separate vacuum chambers, described in the following sections. All chambers are isolated from each other by pneumatic gate valves (VAT Series 108 UHV), which are electronically controlled and allow chambers to be vented independently of each other. An exploded diagram of the machine is shown in Fig. 6.1.

[1] Which have been recently (early 2018) upgraded to be more similar to the machine designed by Ben.

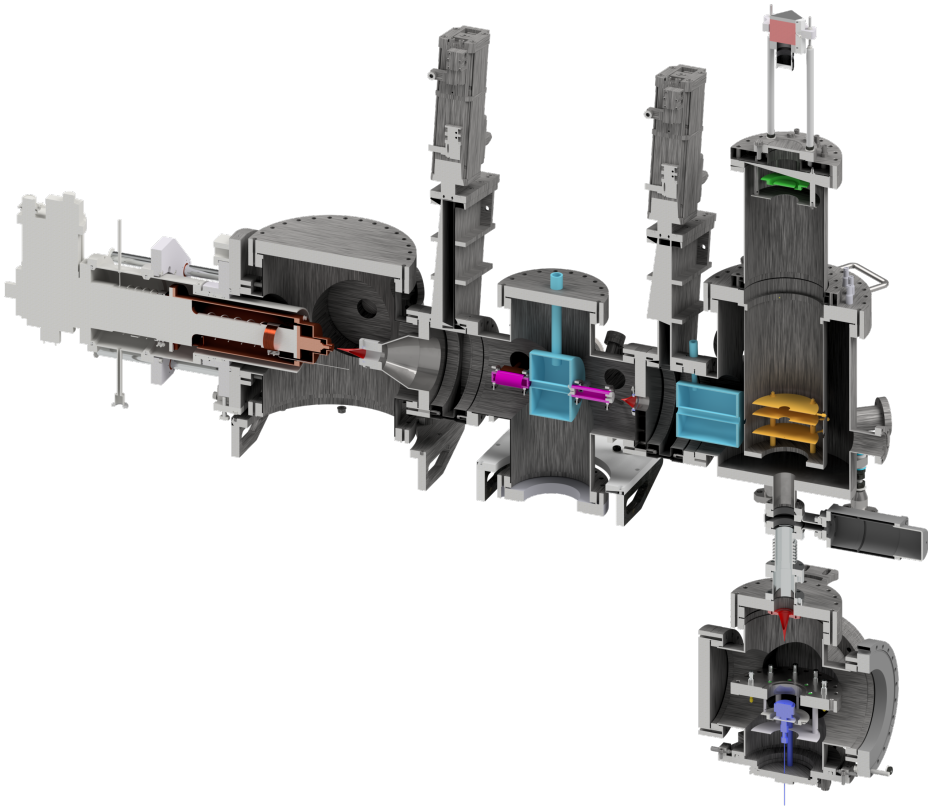

Figure 6.1: An exploded diagram of the HeD machine. Important parts of the machine are shown in false colour to aid the reader, as follows: cold head and nozzle assembly (orange); skimmers (red); pickup cell and oven (magenta); cold traps (sky blue); spectrometer electrodes (yellow); MCPs (green); Even-Lavie valve (dark blue). Render created by Anders Vestergaard.

6.1.1 Source Chamber

The source chamber is where the HeDs are created, and central to this a 5 µm nozzle (Pt-Ir electron microscope aperture) mounted on a cryogenically-cooled cold head (Sumitomo Heavy Industries RDK-408D2). The cold head is cooled by a closed-cycle helium compressor (Sumitomo Heavy Industries F-50L), and can reach an ultimate temperature of around 5 K. In general, for generating the HeDs a nozzle temperature of around 10 to 16 K is desired, thus the nozzle must be heated slightly to stabilise at its working temperature. The nozzle is resistively heated by two high-power resistors (Farnell MHP35470F 47 Ω 1% 35 W) bolted to the nozzle assembly, and the temperature is monitored using a silicon diode

(LakeShore Cryogenics DT-670B-CU). Both diode and resistors are connected to a cryogenic temperature controller (LakeShore Cryogenics Model 335), which allows the nozzle temperature to be stabilised at the desired working temperature. The temperature stability of the nozzle is on the order of $\pm 3\,\mathrm{mK}$, which was greatly increased from previous designs via the addition of stainless steel plates between the nozzle assembly and the cold head itself. These plates act to slightly thermally insulate the nozzle assembly from the cold head, such that the heat generated by the resistors is not dissipated by the cold head so rapidly, resulting in a much more stable nozzle temperature. The entire cold head-nozzle assembly is contained within a copper radiation shield, to prevent radiative heating of the cold head/nozzle assembly. The cold head/nozzle assembly is shown in orange in Fig. 6.1.

High purity He gas (HiQ Helium 6.0, purity $> 99.9999\%$) is introduced into the nozzle assembly from an external cylinder at a backing pressure of 25 bar. This helium travels to the nozzle assembly through copper tubing that is clamped onto the body of the cold head, which ensures that the helium is pre-cooled to a low temperature before it reaches the nozzle itself. There is a small reservoir behind the nozzle where the helium is finally cooled to the desired working temperature, before supersonic expansion through the nozzle results in the generation of a beam of HeDs. The nozzles used are very easily blocked, thus it is imperative that there is a flow of helium gas through the nozzle at all times (even when the machine is idle), to prevent any blockage. To this end, the backing pressure of helium is reduced to 10 bar when the experiment is idle. A lower pressure is used than the working backing pressure (25 bar) for two reasons; firstly to conserve the helium gas; and secondly to limit the flow such that if there was a sudden pumping failure (e.g. a powercut) then the chamber would not overpressurise so quickly. At 25 bar and 16 K the resulting HeD beam will consist of droplets of around 5000 helium atoms on average [9]. The droplet beam travels at around 300 to $400\,\mathrm{m\,s^{-1}}$, and passes through a 1 mm skimmer for collimation before entering the doping chamber. The source chamber skimmer is shown in red adjacent to the nozzle assembly in Fig. 6.1.

As alluded to previously, the continuous helium flow into this chamber means that it must be constantly pumped to maintain a reasonable vacuum and prevent a buildup of helium that could overpressurise and damage the vacuum chamber. To achieve this, the chamber is pumped by a magnetically levitated turbomolecular pump (Edwards STP-iXA2206C, pumping speed $2200\,\mathrm{L\,s^{-1}}$ (quoted for N_2)) which is backed by a dry vacuum pump (Edwards iGX-600L, pumping speed $172\,\mathrm{L\,s^{-1}}$). These

pumps result in a chamber pressure of around 3×10^{-4} mbar under normal working conditions. The pressure is monitored using a Vacom ATMION ATS40C pressure gauge.

6.1.2 Doping Chamber

The HeD beam passes through the skimmer from the source chamber into the doping chamber. This chamber primarily consists of two ports for the addition of pickup cells or ovens (shown in purple in Fig. 6.1 - see below for further detail), together with a cryogenically cooled cold trap. The droplet beam passes through either the pickup cell or oven, which contains some partial pressure of a foreign dopant species. When a HeD collides with a dopant molecule, it solvates the dopant molecule and continues travelling through the vacuum system (see subsection 2.2.1 for a more detailed discussion of the doping process). The dopant species can be vapourised either within an unheated pickup cell, or a heated oven. The machine is designed such that the exact configuration (whether to have ovens or pickup cells) is changeable, adding to the flexibility of the system. To ensure ultra-high vacuum, the chamber is pumped by an magnetically levitated turbomolecular pump (Edwards STP-iX455, pumping speed $450\,\mathrm{L\,s^{-1}}$ (quoted for N_2)), which is backed by a dry screw pump (Busch COBRA BA 100, pumping speed $30\,\mathrm{L\,s^{-1}}$). These pumps result in a chamber pressure of around 1×10^{-9} mbar when the cold traps are filled, rising to around 1×10^{-6} mbar under normal working conditions when the droplet beam is propagating through the chamber, and VAT valves to both adjacent chambers are open. The pressure is monitored using a Vacom ATMION ATS40C pressure gauge.

The pickup cell is a cylindrical cell of 7.4 cm length and 1.4 cm internal diameter, and is mounted such that the long axis of the cylinder is parallel to the droplet beam, and that the droplet beam passes freely through the center of the cell. A photograph of a pickup cell is shown in Fig. 6.2 (a). The cell is connected via swagelok tubing to an externally mounted reservoir containing the desired dopant molecule. The number of molecules solvated by the droplet follows a Poisson distribution [9], as discussed in subsection 2.2.1, and depends strongly on the number density of dopant molecules in the pickup region. To regulate this, the pickup cell is connected to the sample reservoir via a high-precision leak valve (Kurt J. Lesker LVM Series All-Metal Leak Valve), which allows the vapour pressure (and, by extension, the number density) of the dopant molecules in the pickup cell to be finely controlled. This allows dopant species with a wide range of vapour pressures to be run using the same pickup cell.

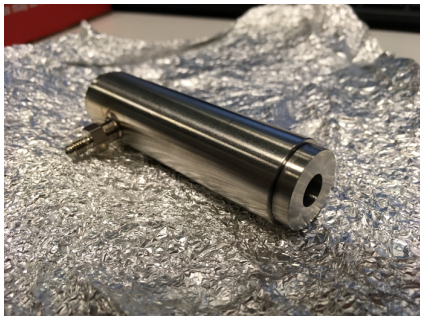

(a)

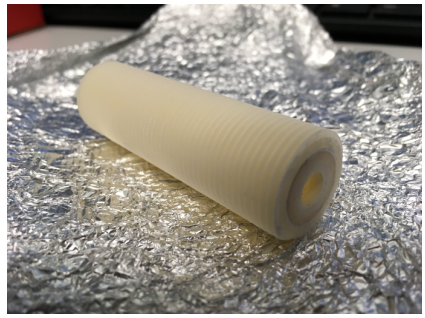

(b)

Figure 6.2: (a) A stainless steel pickup cell, with the central hole for the droplet beam, and the swagelock connection to the external reservoir clearly visible. (b) A ceramic oven shown without tantalum wire, with the grooves clearly visible. The desired molecular sample is placed directly inside this ceramic tube in vacuum.

In addition to the leak valve, there are a number of other Swagelok tap valves connecting the sample reservoir to rough vacuum lines, and allowing it to be isolated from the leak valve. These valves allow the sample to be changed without having to break vacuum in the pickup chamber itself. Figure 6.3 (a) shows this external part of the setup. Any molecule can be run in the pickup cell provided that its vapour pressure is high enough at room temperature, as the pickup cell cannot be heated. For molecules with a low vapour pressure, a heated oven can be installed that allows them to be heated slightly in vacuum.

The oven is a grooved ceramic tube of similar dimensions to the pickup cell, with tantalum wire wrapped in the grooves. The ceramic part of the oven (without wire) is shown in Fig. 6.2 (b). The tantalum wire can then be attached to a power supply (Aim-TTi CPX400DP DC Power Supply) via a high-resistance feedthrough (MeiVac ReVap 900), where a constant current applied to the wire results in resistive heating of the wire and the oven via the Joule effect. The desired sample molecule is placed inside the ceramic tube, and sufficient current is applied (typically 0.5 to 4 A) to slightly vapourise the sample. As the pickup cell, the oven is mounted coaxial to the droplet beam, such that the droplet beam freely passes through and will collide with vapourised sample molecules, resulting in their solvation into the droplets. The power supply is connected to the oven via a vacuum feedthrough, together with a thermocouple that is clamped to the ceramic of the oven body, allowing the temperature to be monitored. There is also a water-cooled copper block that is clamped to

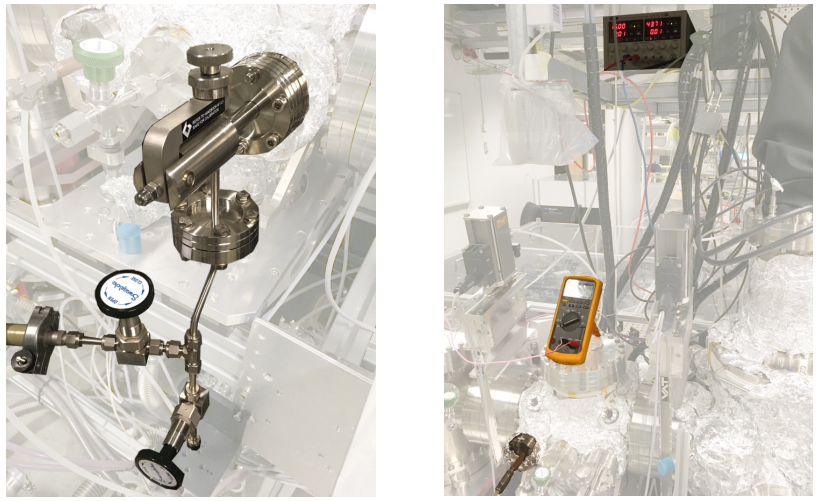

(a) **(b)**

Figure 6.3: (a) The external parts of the pickup cell assembly. The leak valve is clearly visible at the top of the image, and the sample reservoir is at the very bottom, connected to the valve through a swagelok tap. A T-piece is used to connect to an external roughing pump (left side of image). (b) The external parts of the oven assembly. The power supply is visible at the very top, with the multimeter used to measure the temperature visible in the middle, and the oven port with copper cooling feedthrough visible at the very bottom.

the side of the ceramic, to hasten the cooling of the oven when the power supply is switched off. This design of oven can theoretically reach extremely high temperatures (>1500 K - sufficient to vapourise NaCl), and has been used to dope large polycyclic aromatic hydrocarbons such as C_{60} into HeDs on our system. The exact vapour pressure can be controlled by adjusting the current supplied to the oven, however this control is not as fine as that exhibited when using the leak valve in the unheated cell. As such, it can be more difficult to finely tune doping regimes using the oven, and an increase in supplied current will often take several hours to stabilise to the desired doping regime. Additionally, this design requires that vacuum must be broken to refill the oven, so care must be taken to ensure that the oven is not overheated and the sample completely evaporated. The external parts of the oven assembly (power supply, thermocouple, cooling block) are shown in Fig. 6.3 (b).

Both of the aforementioned designs are open-ended to allow the droplet beam to pass through. As such, it is unavoidable that unsolvated

dopant molecules will leak out into the vacuum chamber. These 'effusive' molecules have a deletrious effect on any experiments, as ions resulting from effusive molecules are often indistinguishable from those solvated in HeDs. As they are often indistinguishable, it is often not possible to remove their contributions in subsequent analysis, so it is critical to be able to reduce the number of effusive molecules that reach the interaction region. To achieve this, cold traps cooled with liquid N_2 (T = 77 K) are used to trap effusive molecules. The cold trap is effectively a stainless steel reservoir of liquid N_2, with a high surface area to ensure that unsolvated (or other background) molecules in the chamber are frozen onto it. The cold traps are highlighted in blue in Fig. 6.1. Each cold trap consists of a reservoir for the liquid N_2 with a 3 mm hole in the center (drilled into an aluminium insert) to allow the droplet beam to pass through it. The small internal diameter ensures that any effusive molecules co-propagating with the HeD beam are effectively trapped and do not enter the target region. The location of the cold trap (between the two ports where pickup cells/ovens can be added) means that effusive molecules arising from a cell/oven attached to the first port (nearest the nozzle) will be more effectively trapped than those from the second[2], which is a consideration when planning experiments. As explained below, there is also a cold trap at the entrance to the target chamber, which serves to further reduce the effusive contribution. Experimentally, it is observed that filling the cold traps can reduce the amount of effusive signal by several orders of magnitude, but some molecules are more effectively trapped than others (for example, anything that is still gaseous at 77 K will not be trapped).

6.1.3 Target Chamber

Doped HeDs from the doping chamber pass through a 2 mm skimmer (shown in red between the two cold traps in Fig. 6.1), and enter the target chamber. Immediately after the entrance to the target chamber, there is a second cold trap (shown in blue in Fig. 6.1), which serves to trap background molecules in the target chamber and further reduce the number of unsolvated effusive molecules. The doped droplet beam then enters the interaction region, where it is crossed at 90° by one or more focussed laser beams. The point at which the droplet beam and the laser beams cross is in the center of a velocity-map imaging (VMI) spectrometer [139], which will be discussed in further detail in subsection 6.1.5. The interaction with the laser beam(s) produces ions, which are focussed towards a position sensitive detector by the VMI electrodes. Light from this detector is detected

[2]Doped droplets from an oven/cell on the second port will only pass through one cold trap before reaching the target chamber.

by a fast-framing CCD camera, data from which is then fed to a computer for readout. The VMI plates and detector are highlighted in yellow and green respectively in Fig. 6.1. This chamber is pumped by a magnetically-levitated turbomolecular pump (Edwards STP iXR-1606, pumping speed $1600\,\mathrm{L\,s^{-1}}$ (quoted for N_2)), which is backed by the same dry screw pump as used on the doping chamber (Busch COBRA BA 100, pumping speed $30\,\mathrm{L\,s^{-1}}$). Under normal operating conditions with the cold trap filled, the pressure in this chamber is often below 1×10^{-9} mbar, rising to around 1×10^{-8} mbar when the HeD beam is introduced.

6.1.4 Supersonic Source Chamber

The final chamber on the HeD machine is mounted below the target chamber, and contains an Even-Lavie valve (EL-7-4-2011-HRR, 600 Hz) (shown in dark blue in Fig. 6.1). The Even-Lavie valve produces an intense beam of isolated (i.e. not in HeDs) molecules, that are cooled during a supersonic expansion by collisions with a helium carrier gas. A molecular sample is placed inside the valve and a backing pressure of 80 bar of helium gas is applied to the backside of the valve. The valve is pulsed by an external electronic valve driver, and the resultant beam of molecules passes through a 4 mm skimmer (shown in red above the Even-Lavie valve in Fig. 6.1) before entering the target chamber. The beam of isolated molecules then interacts with the laser beams in an analogous way to the droplet beam. This chamber is pumped using a magnetically-levitated turbomolecular pump (Edwards STP iXR-1606, pumping speed $1600\,\mathrm{L\,s^{-1}}$ (quoted for N_2)), backed by the same dry backing pump as the source chamber (Edwards iGX-600L, pumping speed $172\,\mathrm{L\,s^{-1}}$). These pumps result in a chamber pressure of around 5×10^{-7} mbar, rising to 1×10^{-5} mbar when the Even-Lavie valve is running. The purpose of this chamber is to allow comparison between isolated molecules and molecules in HeDs to be undertaken quickly, and using the same laser parameters. No work presented in the main body of this thesis was undertaken using isolated molecules, and the information presented here is included only for completeness, and to aid in the interpretation of appendix B.

6.1.5 Detection Systems

As mentioned previously, the ions are produced inside a VMI spectrometer, and are focussed onto a position-sensitive detector using this spectrometer. The spectrometer is highlighted in yellow in Fig. 6.1, and consists of three stainless steel electrodes, referred to as the 'repeller', 'extractor', and 'grounded plate', each plate is 1 mm thick. Ions are produced in

the space between the repeller and the extractor[3]. The voltage applied to the repeller (V_{Rep}) is in the range of 2 to 8 kV, and the voltage applied to the extractor (V_{Ext}) is lower, roughly following Eq. 6.1.

$$V_{\mathrm{Ext}} \approx 0.67 \times V_{\mathrm{Rep}} \tag{6.1}$$

This separation of the two plates is 3.5 cm, resulting in a voltage gradient of 0.19 to 0.76 kV cm^{-1} between the plates. This voltage gradient accelerates the ions towards the detector. The voltage ratio is chosen according to Eq. 6.1[4], as this results in a field where the position at which the ions impinge on the detector is independent of the position at which they are ionised in the interaction region, and depends only on their velocity in the plane of the detector - this is the 'velocity-mapping' in VMI. A fuller account of the process was given in chapter 4. The entire spectrometer is also shrouded in a cylindrical tube of mu-metal, to protect against stray magnetic fields.

The detector consists of two stacked microchannel plates (MCPs - El Mul Technologies B050V, 38 mm active diameter) and a P47 phosphor screen (El Mul Technologies Scintimax P47). The MCPs consist of a large number of small channels (∼25 µm diameter), and when an ion impinges on a channel in the front MCP, it creates electrons via secondary emission. These electrons are accelerated through the MCP stack via a voltage difference of 1.8 kV applied between the front and back of the MCP stack. The channels are cut such that as the electrons are accelerated, they repeatedly collide with the channel walls, resulting in further secondary emission. This process results in a gain of around 10^3 electrons per ion per MCP, for an overall gain of 10^6 electrons per impinging ion across the whole stack. The resultant electron cascades are then accelerated onto the P47 phosphor screen (held at 3.5 to 3.8 kV, resulting in a voltage difference of around 2.3 to 2.6 kV between the back of the MCP and the phosphor). As the electrons hit the phosphor screen, the phosphor screen produces a flash ($\tau \approx$100 ns) of blue (400 nm) light. This light is subsequently detected by a CCD camera (Allied Vision Prosilica GE680), and the resulting images are sent to a computer for readout. The exact voltages applied to each component of the detector depend upon the desired experiment, as discussed below.

Focussing the laser beams onto the HeD beam will result in the creation of a large number of different ions. It can be advantageous to get

[3]The droplet beam enters between these two electrodes, while the Even-Lavie valve beam enters through a 3 mm hole in the repeller plate.

[4]In practice, it often needs to be adjusted by ±100 V to achieve good focussing.

information about all the ions produced in the duty cycle (time-of-flight (ToF) mode), or to focus on one specific ion of interest (imaging mode). In ToF mode, the front of the MCP stack and the phosphor screen are left grounded, and the back of the MCP is raised to 1.8 kV, all ions produced will diverge in time based on their m/z ratio, and will impinge on the detector over the course of around 20 µs. The MCP back is connected to an oscilloscope (LeCroy Wavesurfer 64 MXs-B)[5], and as ions impinge on the MCP, they induce a small AC current which results in a small voltage drop on the MCP which can be measured using the oscilloscope. These voltage drops are separated in time corresponding to the arrival times of the ions, and by monitoring this signal over the whole time range, a ToF spectrum can be produced. This spectrum can then be calibrated and used to find the precise arrival time of a specific ion species, that can then be used in imaging mode.

Taking an image of all ions produced in a duty cycle is not experimentally useful as every image will overlap, and no information can be gained. However, by applying a voltage of 1.2 kV to the MCP back, and pulsing the MCP front to −0.6 kV during the arrival time of a specific ion, an image of one single ion species can be obtained. This pulsing is achieved using a delay generator (Stanford Research Systems DG535), which can pulse the MCP front to −0.6 kV for 100 to 400 ns. The delay generator is connected to the 1 kHz trigger coming from the laser, such that it synchronises the MCP pulsing with the arrival time of a specific ion. Under this regime, the voltage across the MCP is only 1.2 kV when the pulsing is not active, which is not enough to amplify signal from impinging ions and results in no amplification. When the MCP is pulsed to −0.6 kV, the MCPs amplify the impinging ions and the resulting electrons are incident on the phosphor screen, producing an image which is captured by the CCD camera. As the pulsing is set to only be active during the time in which a specific ion arrives at the detector, the resulting image only contains ion signal from one specific ion species.

6.2 Laser Systems

Here a general overview of the optical setup, together with beam characterisation techniques, is presented. The setup presented here is essentially the same for all experiments presented in this thesis. Where there is a difference between the setup shown here and a specific experiment, it is documented in the relevant results chapter.

[5]Through a high-pass filter to block the 1.8 kV DC voltage from the oscilloscope.

6.2.1 Spitfire Ace

The laser system used for all experiments described in this thesis is a Spectra-Physics Spitfire Ace-35F regenerative amplifier, pumped by a Spectra-Physics Empower 45 Nd:YLF laser, and seeded by a Spectra-Physics MaiTai SP oscillator. The oscillator produces a train of 5 nJ pulses (at a repetition rate of 84 MHz), with a bandwidth of 60 nm. These pulses are fed into the regenerative amplifier which operates at a repetition rate of 1 kHz and amplifies the pulses to a maximum pulse energy of 5 mJ, resulting in an average power of 5 W. After amplification the pulses are necessarily very strongly chirped (τ=160 ps), so are subsequently compressed down to 35 fs.[6] There are two ports at the laser output, which allow the user to take either the compressed 35 fs pulses, or the uncompressed (chirped) 160 ps pulses. A combination of a half-wave plate (HWP) and polariser allow the total output pulse energy to be divided between the compressed or the uncompressed outputs as desired. The 1 kHz trigger signal is taken from the laser system and used to synchronise various parts of the experiment with the arrival of the laser pulse..

In general, the uncompressed output of the laser is used to align molecules ('alignment arm') and the compressed output is used to ionise and Coulomb explode molcules ('probe arm').

6.2.2 Optical Setup

Both alignment and probe arms exit the laser and are guided towards the HeD machine via a series of mirrors. Various optical components are present in each beam path, detailed below. A sketch of the optical setup is shown in Fig. 6.4.

The alignment arm (dashed line) exits the laser and passes through a HWP and thin-film polariser (mounted at Brewster's angle) to afford fine power control. The portion of the beam reflected from the polariser is dumped in a ceramic beam dump, and the transmitted portion is taken for further use. The transmitted beam can then be passed through a long-pass filter (LPF) to produce a truncated alignment pulse if desired (see chapter 10). The beam exiting the laser output is around 10 mm in diameter, so it is then passed through a telescope (T1) to shrink it down to around 4 mm and to allow the divergence to be controlled. Following this, the polarisation is controlled via transmission through a HWP and

[6] Readers may note that the quoted oscillator bandwidth of 60 nm would result in a transform limited pulse of 15 fs if fully compressed. In reality, the regenerative amplifier cannot amplify the full bandwidth supplied by the oscillator, so the effective bandwidth is only around 30 nm, and not all of this bandwidth is effectively compressed.

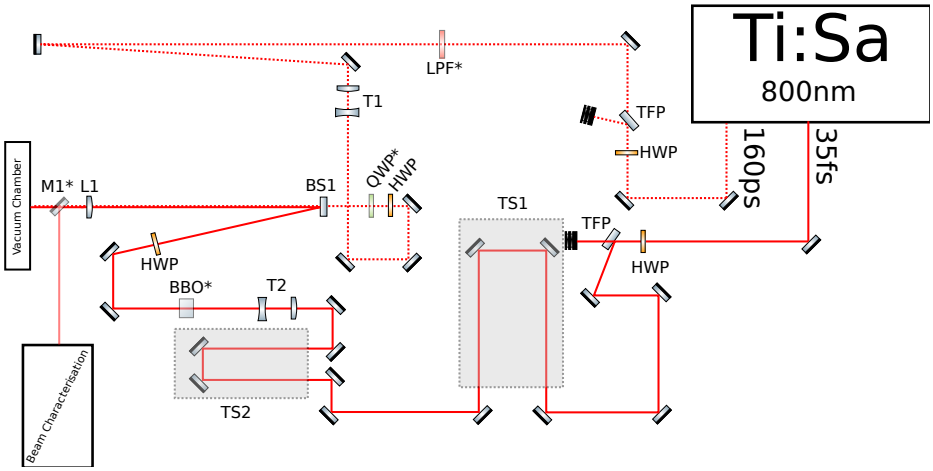

Figure 6.4: A sketch of the optical setup. Optical components rendered with transparency, and with asterisks in the name, are removable. The alignment beam is shown as a dashed line, and the probe beam as a solid line. See text for details.

a quarter-wave plate (QWP), allowing linear, elliptical, and circular polarisation to be produced as desired. The beam is subsequently focussed into the vacuum chamber through a singlet lens with 300 mm focal length (L1). Typically, this results in the beam waist in the focus being around 35 µm.

The probe arm exits the laser and also passes through a HWP-polariser combination to afford power control. As the pulses are substantially shorter than those in the alignment arm (and close to the transform-limit), the reflected beam is taken for further use as the dispersion caused by transmission through the polariser will temporally stretch the pulse. This beam is then directed onto two translation stages, a 500 mm stage (Schneeberger R-9800 - TS1), and a 100 mm finer stage (Newport M-UTM100PP - TS2). These stages allow the delay between the two arms to be adjusted such that they are synchronised in time, and allow scanning of experimental observables as a function of the delay time. In total these stages can be used to provide a maximum of 4000 ps of delay, but under normal operation the Schneeberger stage is left stationary once the beams are roughly synchronised and the Newport stage is scanned, as it allows finer time steps to be taken. The Newport stage allows a maximum of 666 ps of delay to be added from the point at which the pulses arrive at the same time (referred to as 't_0'), which is normally beyond sufficient for general use. The beam is then directed through a telescope (T2) to

control the divergence and the beam waist in the focus. Following this, a β-barium borate (BBO) crystal can be introduced for second-harmonic generation (SHG), producing pulses at a central wavelength of 400 nm if desired[7]. This is followed by a HWP with the appropriate coating for the wavelength used, to allow the polarisation to be controlled. Following this, the beam is overlapped with the alignment beam using either a dichroic mirror or 80:20 (transmitted:reflected) beamsplitter[8] (BS1), depending on the wavelength of the probe pulses. It is focussed into the chamber through L1. For alignment experiments, the beam waist of the probe beam must be smaller than that of the alignment beam to minimise focal-volume effects, thus the telescope in the probe beam path is adjusted to achieve a beam waist of around 25 µm in the focus. Both beams enter the chamber through a UV-fused silica (UVFS) vacuum window, and are dumped on a beam dump after exiting the back window (not depicted in Fig. 6.4).

6.2.3 Beam Characterisation

There are a variety of methods used to characterise the laser beams, and these will be detailed in the following paragraphs.

The average power of the laser beam(s) is measured using a power meter (Thorlabs PM100D Power and Energy Meter Console with an S310C head), and controlled primarily using HWP-polariser combinations as discussed previously. The pulse duration of the 800 nm compressed output is measured using a single-shot autocorrelator (Minioptic Delta Single-Shot Autocorrelator). The pulse duration of the uncompressed output can be measured via a cross-correlation with the compressed output. To achieve this, the two beams are directed through a BBO crystal to achieve SHG, and the 400 nm SHG signal is monitored as the compressed pulse is scanned through the uncompressed pulse using the Newport delay stage previously mentioned. The SHG signal is generally monitored using a spectrometer (AvaSpec 3648), and the resulting trace allows the temporal shape of the uncompressed pulse to be measured.

To characterise the focal spot-sizes of the laser beams, they are focussed through the singlet lens towards the vacuum chamber, but a silver mirror is placed between the lens and the window into the vacuum chamber. This mirror redirects the beam through a UVFS window (of

[7]It is also possible to create pulses centered at 266 nm at the same point in the beam path using collinear third-harmonic generation (THG).

[8]The alignment pulses are transmitted through the back of this optic, as they are already strongly chirped so the additional dispersion has negligible effect.

the same dimensions as the vacuum window), and towards either a fast photodiode (Thorlabs DET10A/M) or a beam-profiling camera. When first establishing an optical setup, the focal spot sizes of the two beams must be measured to ensure that they are the correct size (as mentioned previously). To measure the focal spot size, the beams are first attenuated using several neutral density (ND) filters, which attenuate the power by a factor of up to 10^5. They are then focussed onto a 10 µm pinhole mounted on the front of the fast photodiode. The attenuation serves to prevent the focussed beams from damaging either the pinhole or the diode. The position of the diode along the beam propagation direction is scanned to ensure that the pinhole is placed exactly at the point where the beam(s) focus, and telescopes are adjusted to ensure that both beams focus at the same point. When this is confirmed, then the diode is scanned perpendicular to the propagation direction, in the focal plane, both horizontally and vertically. The signal measured on the diode is recorded on the oscilloscope previously mentioned. Provided that the focal spot size is larger than the pinhole, the resulting intensity traces can be used to ascertain the focal spot size. This is performed on both beams and telescopes are adjusted to ensure that the desired spot sizes are attained.

The spatial overlap of the two beams in the focus is a critical parameter for alignment experiments, as poor spatial overlap will result in the probing of unaligned molecules, rendering the measurements meaningless. A photodiode can be used to ensure that the foci are spatially overlapped to within the 10 µm pinhole, but using a photodiode for this is often cumbersome during day-to-day running of the experiment. As the overlap must be monitored regularly, a webcam (Genius Widecam F100) has been converted in-house to be used as as beam profiler. The laser beams are heavily attenuated (by a factor of up to 10^{10}), and the camera is placed in the focus of the beams. The camera allows the spatial position and overall shape of the foci of each beam to be monitored very quickly, although (unlike the photodiode) it cannot be used to provide accurate measurements of the beam waist in the focus. Thus, once the focal spot sizes are measured using a diode and pinhole, during day-to-day operation the beams are regularly directed towards the camera and their pointing slightly adjusted by hand to ensure that the foci of each beam are completely overlapped.

6.3 Summary

This chapter has described the experimental setup used in Femtolab in detail, and shown how many of the techniques documented in preced-

ing chapters are realised experimentally. The following chapters describe the results of experiments recorded on this system, starting with an an experiment on the CS_2 dimer.

CHAPTER 7

Structural Imaging of the CS_2 Dimer

The first step in time-resolved imaging of a bimolecular reaction is creation of a bimolecular pre-reactive complex. This chapter details the alignment and imaging of the carbon disulphide dimer ($(CS_2)_2$) in HeDs, as a model system for weakly bound pre-reactive complexes. The dimer structure is determined using LIA and CEI. Analysis of $CS_2{}^+$ recoil velocities allows the structure of the dimer to be unambiguously determined, and additional information about the precise structure can be obtained from the S^+ recoil velocities. The work presented here serves to set the scene for the remainder of the thesis, as the techniques, applied to a relatively simple system here, are applied to more complex systems in later chapters.

7.1 Background

The structure of the CS_2 dimer has been determined in the gas phase via IR spectroscopy [46], and is displayed in the inset of Fig. 7.1. The two CS_2 molecules are connected in a cross-shaped geometry with D_{2d} symmetry, and the C-C distance is 3.5 Å. The dimer is a prolate symmetric top with rotational constants A =1.637 GHz and $B = C$ =1.153 GHz. The polarisability elements have been calculated (wB97XD/aug-pcseg-2) to be $\alpha_{\parallel}$ =12 Å^3 and $\alpha_{\perp}$ =17.5 Å^3, where $\alpha_{\parallel}$ is defined as the polarisability parallel to the C-C axis (shown as the y axis in Fig. 7.1).

The experimental setup has been described in detail in chapter 6. Figure 7.1 shows essential parts of the setup. The laser beams and detector

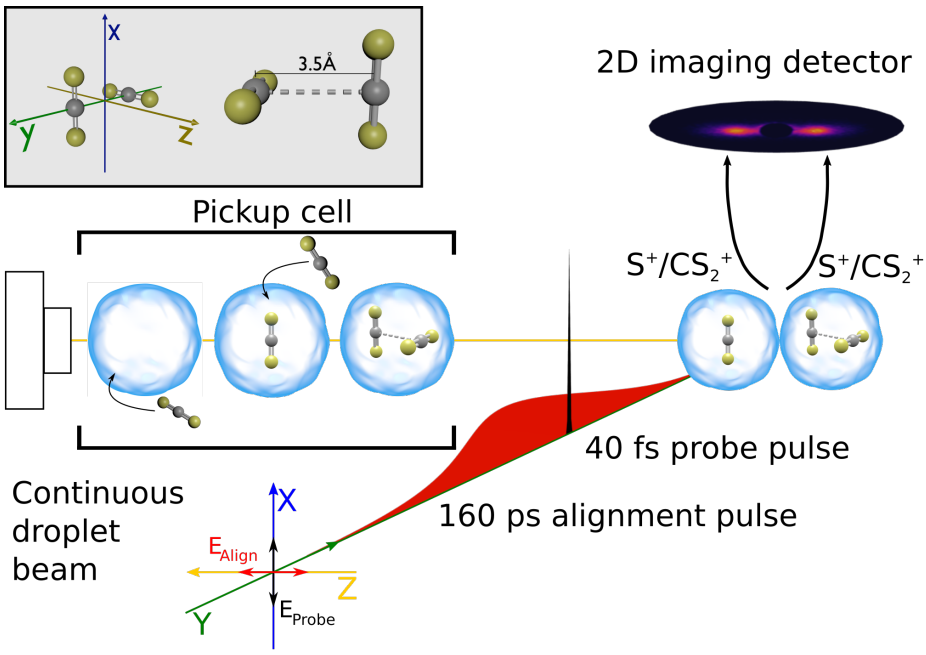

Figure 7.1: Schematic of the essential parts of the experiment. In the case depicted here the alignment (probe) laser pulse is linearly polarised along the Z (X) axis. The inset shows a sketch of the gas-phase dimer structure.

Laser beam	Intensity (W/cm^2)	Pulse duration	Beam waist (µm)
Alignment	8×10^{11}	160 ps	35
Probe	3×10^{14}	40 fs	25

Table 7.1: Laser parameters used for structural determination of the CS_2 dimer in HeDs.

are polarised/placed as described on page xi. The HeDs were formed by expanding He gas at 16 K and 30 bar backing pressure, resulting in a beam of droplets consisting of 8000 He atoms on average. The droplet beam is passed through a pickup cell containing CS_2 vapour, and the partial pressure of the CS_2 vapour can be adjusted to optimise the pickup of CS_2 monomer or dimers (see section 7.2). The laser parameters are summarised in Table 7.1.

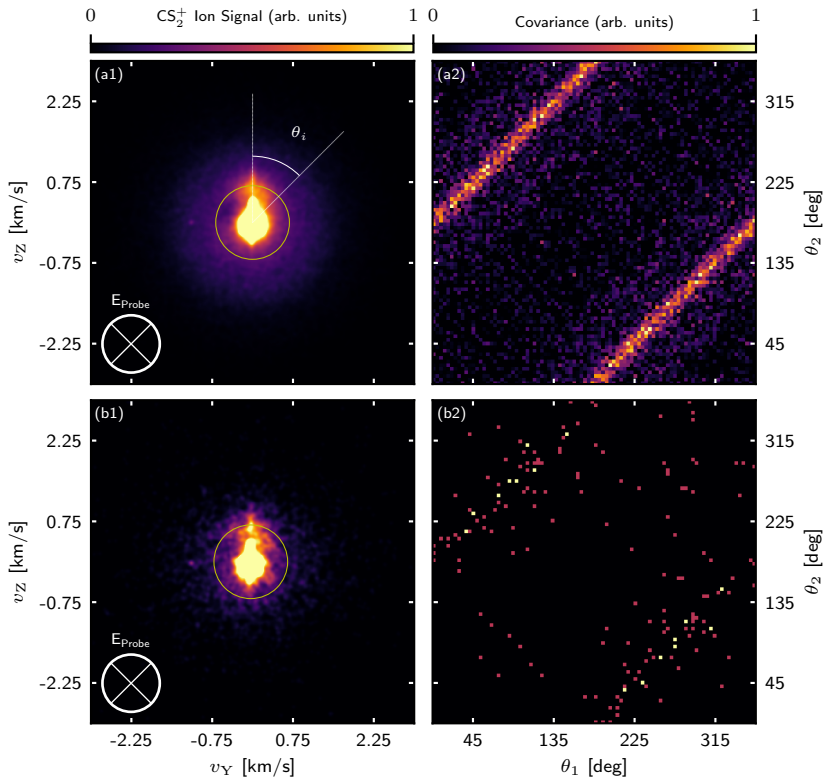

Figure 7.2: (a1)-(b1) CS_2^+ ion images and (a2)-(b2) corresponding angular covariance maps created from ions outside the annotated yellow circles. The polarisation state of the probe pulse is shown in the lower left corner of each image. Data in row (a) [(b)] was recorded under the DDC [MDC].

7.2 Forming the CS_2 dimer in Helium Droplets

Before embarking on a more in depth study of $(CS_2)_2$, we first demonstrate that it is possible to form and detect $(CS_2)_2$ inside HeDs. The most obvious way to attempt this would be to look for the presence of $(CS_2)_2^+$ ions created by the probe pulse alone in the ToF spectrum at an m/z ratio of 152 Da. However, no such signal is observable, as the singly charged dimer cation is very fragile, and readily fragments into two CS_2^+ ions. To circumvent this problem, we measure the recoil velocity of CS_2^+ ions, as CS_2^+ ions stemming from Coulomb explosion of $(CS_2)_2$ will have a higher velocity in the detector plane than those stemming from single ionisation of CS_2 monomers (see section 5.2).

Figure 7.2 (a1) shows a velocity-map image of CS_2^+ ions recorded with the probe pulse only, polarised perpendicular to the detector plane (along X). The image is dominated by an intense signal in the centre. This signal arises from the low velocity ions formed via ionisation of CS_2 monomers. There is also a significant amount of signal detected at larger radii, which is consistent with the formation and Coulomb explosion of $(CS_2)_2$. To substantiate this assignment, the angular covariance map was calculated, shown in Fig. 7.2 (a2). The covariance map is calculated using ions detected outside the annotated yellow circle in (a1), this corresponds to ions travelling faster than $0.65\,\mathrm{km\,s^{-1}}$. Two distinct diagonal lines centered at $\theta_1 = \theta_2 + 180°$, where θ_i $(i = 1, 2)$ is the angle between an ion hit and the vertical center line, shown on panel (a1). These covariance signals show that one CS_2^+ ion is produced in coincidence with another CS_2^+ ion travelling in the opposite direction. This strongly indicates that the ions originate from double ionisation of $(CS_2)_2$ which subsequently fragments into two CS_2^+ ions. The angular positions of the CS_2^+ hits outside the yellow circle are therefore interpreted as a measure of the projection of the recoil velocities of CS_2^+ ions from dimers on the detector (YZ) plane. This is therefore a measure of the position of the C-C axes in the dimers at the point of ionisation. The uniform extent of the covariance signal over the full 360° range shows that the C-C axes are randomly aligned, expected here as there is no alignment laser pulse present.

Figure 7.2 (b1) shows an analogous CS_2^+ image, but now the partial pressure of CS_2 vapour in the pickup cell is reduced. It is clear that there are fewer ions detected outside the annotated yellow circle, but there is still an intense central signal. Additionally, the signal in the angular covariance map (panel (b2)) has now almost completely disappeared. This signal has already been shown to arise from fragmentation of $(CS_2)_2$, so the disappearance of it suggests that now the amount of $(CS_2)_2$ in the HeDs is dramatically reduced. On the basis of this, this doping regime is defined as the 'monomer-doping-condition' (MDC), and the regime used to record the data in panel (a1) is defined as the 'dimer-doping-condition' (DDC).

However, as discussed in chapter 2, the doping of molecules into HeDs follows Poisson statistics, and as such there are still more monomers than dimers in the DDC. It is also plausible that higher oligomers (trimers, tetramers) are formed. To ensure clean conditions, it is desirable to minimse the contributions of higher oligomers as much as possible, but it is impossible to only dope the droplets with a specific cluster size. To minimise the contributions of higher oligomers, the partial pressure of CS_2 gas in the DDC is kept as low as possible whilst retaining a usable dimer signal. Table 7.2 shows total number of ions recorded in each image in

Doping Condition	Total Ions	Low KE (%)	High KE (%)
MDC	14740	12320 (84)	2415 (16)
DDC	83520	55470 (67)	28050 (33)

Table 7.2: A comparison of the relative yields of high (outside yellow circle) and low (inside yellow circle) kinetic energy ions recorded in the MDC and DCC (Fig. 7.2 (b1),(a1)).

Fig. 7.2 (a1) and (b1), inside and outside the annotated yellow circle. It is clear that the number of dimers is increased when operating under the DDC. Comparing to an idealised Poisson distribution (see Fig. 2.3), it would still appear as though this ratio of monomers to dimers would result in some non-negligible contribution from higher oligomers. However, the central portion of the detector is substantially less sensitive than the outer radii due to the consistently high ion flux on this part of the detector over its lifetime. Thus, it is expected that the number of low KE ions in Table 7.2 is substantially underestimated, making it less likely that higher oligomers are making any substantial contribution. Despite the limitation that the desired oligomer cannot be completely isolated for further study, it is clear that we can control the doping and enter a regime where there are signifcant amounts of $(CS_2)_2$ in HeDs.

7.3 The Structure of $(CS_2)_2$ in Helium Droplets

Having demonstrated that it is possible to form and detect $(CS_2)_2$ in HeDs, we now consider the possibility to align it and determine its structure. To do this, a number of possible structures (and their expected alignment behaviour) are considered, and are then compared to experimental results.

Column (1) of Fig. 7.3 shows four possible structures of $(CS_2)_2$ in HeDs. These structures are the cross-shaped structure (a1); the slipped-parallel structure (b1); the T-shaped structure (c1); and the linear structure (d1). In column (1) the structure are shown in the molecular frame, and the polarisability elements are annotated on each axis in units of $Å^3$. It is known from IR spectroscopy that the gas-phase structure of $(CS_2)_2$ is the cross-shaped structure shown in panel (a1). The other structures are all considered due to vdW complexes of other small molecules exhibiting them in the gas-phase [46]. The slipped-parallel structure (b1) is exhibited by the OCS dimer in the gas phase; the T-shaped structure (c1) is exhibited by the acetylene (HCCH) dimer; and the linear chain structure (d1) is exhibited by the HCN dimer.

Columns (2) and (3) in Fig. 7.3 show how each structure (a1)-(d1) will align in the laboratory frame when exposed to either a circularly polarised (polarised in the XZ plane - column (2)) or a linearly polarised (polarised along the Z axis - column (3)) laser pulse. As described in chapter 4, a circularly polarised laser pulse will align the LPA to the propagation direction (Y) of the laser, and a linearly polarised laser pulse will align the MPA to the polarisation direction (here Z) of the laser pulse. The sketches in columns (2) and (3) show how each structure will align. In the case where there are multiple possible aligned geometries, only one is shown, and the curved arrows on each space-fixed axis shows an axis about which rotation (free or hindered)[1] is possible.

The possible structures are now compared to the aligned ion images. Figure 7.4 shows ion images that are analogous to those presented in Fig. 7.2, but now an alignment pulse is present. The alignment pulse is 160 ps long, which is longer than the rotational period of $(CS_2)_2$, so the alignment dynamics are expected to be esssentially adiabatic. The probe pulse is therefore synchronised to arrive at the peak of the alignment pulse, to probe the best aligned molecules.

Figure 7.4 (a1) shows a CS_2^+ ion image recorded as in Fig. 7.2, but with an alignment pulse also present. The alignment pulse is circularly polarised in the XZ plane. The emission direction of the CS_2^+ ions outside the annotated yellow circle is strongly confined along the Y axis; and the covariance signals in the corresponding covariance map (panel (a2)) are now truncated to short islands centered at (90°,270°) and (270°, 90°). The distribution of ions outside the yellow circle is peaked at the outermost part, and is separated from the intense central signal. These observations indicate that the $(CS_2)_2$ is aligned with the Inter-Monomer Axis (IMA) confined along Y, and that the IMA is not able to rotate around Z into the plane of the detector. We expect that a circularly polarised field will align the LPA along the propagation axis of the laser field, the Y axis. As such, the structure of the CS_2 dimer must be one in which the IMA is the sole LPA. Considering the structures shown in Fig. 7.3, this is true only true for the cross-shaped dimer (row (a) in Fig. 7.3). For the other structures the LPA is either not the IMA (as in for the T-shaped dimer (row (c)), or there are multiple LPAs, such as in rows (b) and (d). If there are multiple LPAs, then we expect to see a rotation such that either of the LPAs can be aligned to the Y axis at any one time (e.g. Fig. 7.3 (b2) or (d2)).

[1] Where only one rotation is shown, the molecule can freely rotate around that axis. Where two are shown, the molecule may not be able to freely rotate about both axes simultaneously. For example, in panel (c3), the depicted structure can freely rotate around Z, and another aligned geometry can be reached via a 90° rotation around X.

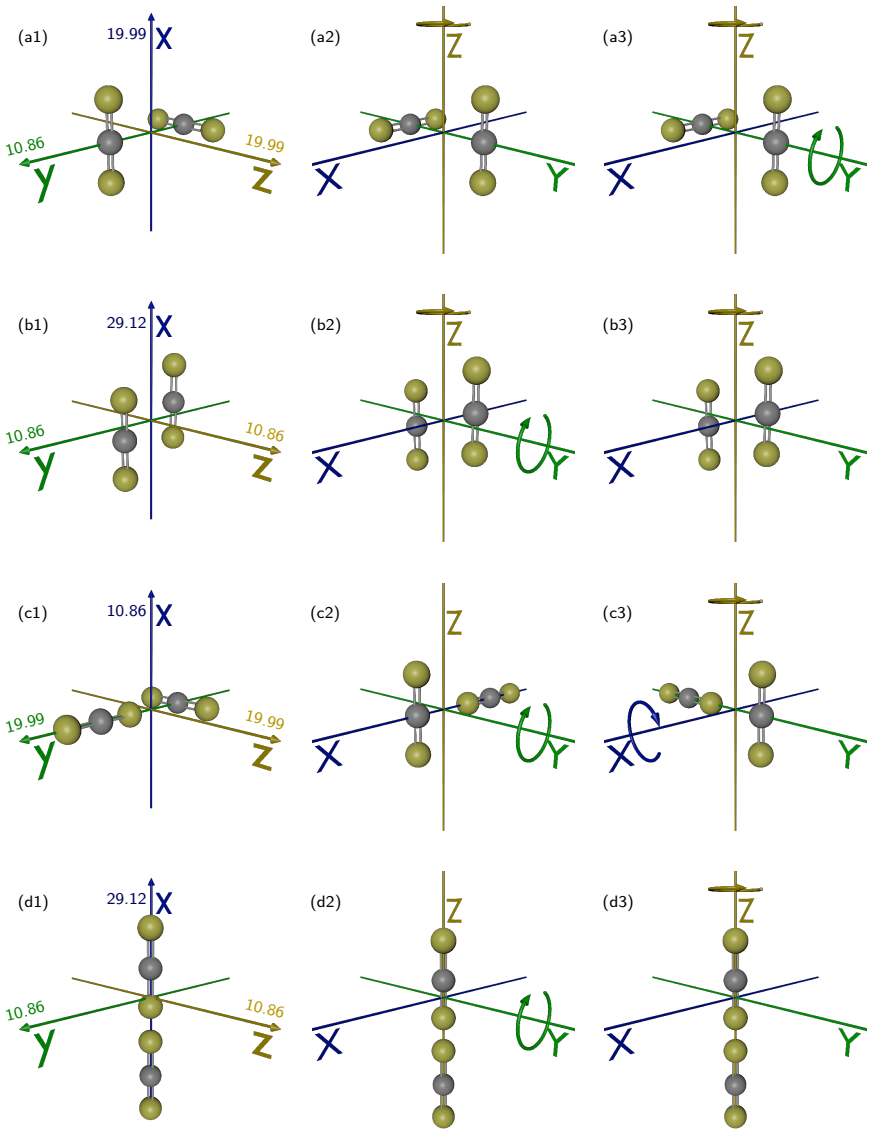

Figure 7.3: (a1)-(d1) Sketches of possible $(CS_2)_2$ structures, shown in the molecular frame. Polarisability elements are annotated on each relevant axis, in units of $Å^3$. (a2)-(d2) [(a3)-(d3)] Sketches of how each structure would align in the laboratory frame, when exposed to a laser field circularly [linearly] polarised in the XZ plane [along the Z axis]. Curved arrows show axes around which rotation is possible

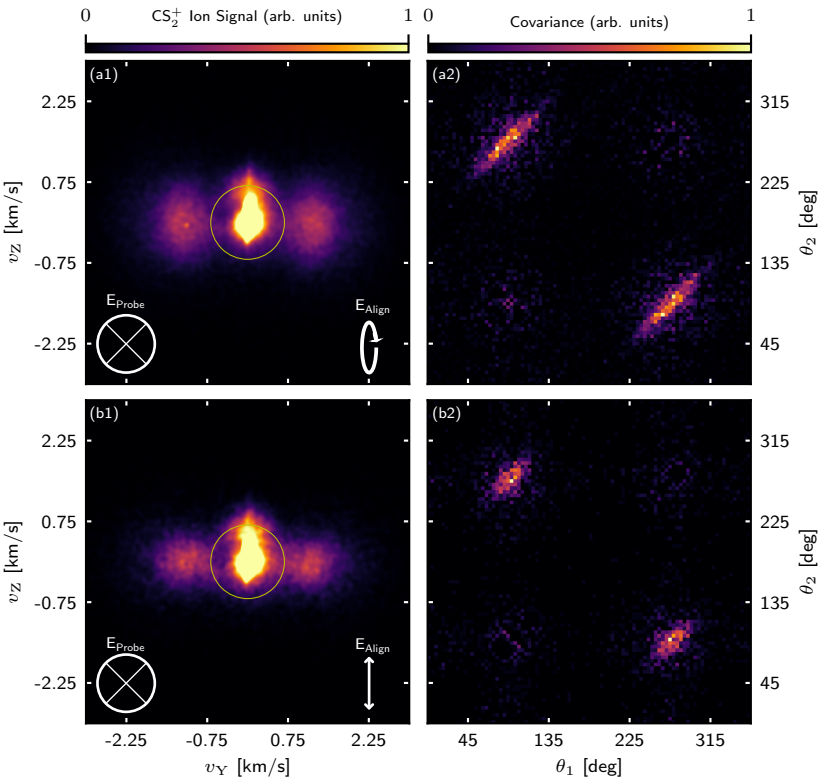

Figure 7.4: (a1)-(a2) CS_2^+ ion images and (a2)-(b2) corresponding angular covariance maps created from ions outside the annotated yellow circles. The polarisation state of the probe [alignment] laser is shown in the lower left [right] corner of each ion image. All data was recorded under the DDC.

This would manifest in the observed distribution of ions in Fig. 7.4 (a1) extending towards the center of the detector, rather than being peaked at the outer radii. This is not observed, therefore the structure of $(CS_2)_2$ in the HeDs is the gas-phase cross-shaped structure (Fig. 7.3 (a1)).

As just shown, in this case it is possible to unambiguously determine the structure by analysis of the circularly polarised image alone. This is not necessarily the case for other systems, so here we show that our results can be corroborated by analysis of images recorded with a linearly polarised alignment pulse present. Figure 7.4 (b1)) shows a CS_2^+ image recorded now with an alignment pulse present that is linearly polarised along the Z axis, with the corresponding angular covariance map shown in panel (b2). In this case, the observed distribution of ions is still

slightly peaked at the outermost part (a consequence of the projection - see section 5.3), but the distribution now extends towards the center of the detector as a broad stripe (rather than two localised spots as in panel (a1)). This distribution of ions is consistent with ions being ejected in the XY plane, which would give rise to the observed stripe when projected onto the YZ plane. To get this distribution of ions, the IMA must be aligned such that it is confined to, but can freely rotate in, the XY plane. An alignment pulse that is linearly polarised along Z will align the MPA to the Z axis (but the MPA will freely rotate around Z). Therefore, to produce the observed distribution of ions, the MPA must be orthogonal to the IMA. This is only the case for the cross-shaped and the slipped-parallel structures (Fig. 7.3 row (a) and (b)), therefore we can conclusively discount the other structures (both of which would give rise to some ion signal appearing along the Z direction of the image). Figure 7.4 (b1) is therefore completely consistent with our prior observations, but this image alone would not enable us to comprehensively discount the slipped-parallel structure.

A final difference between Fig. 7.4 (a1) and (b1) is that the observed distribution of ions extends more along Z under the circularly polarised alignment field (a1) than the linearly polarised field (b1). This effect can also be seen in the angular covariance maps, with the covariance island being longer in the circularly polarised case (a2) than the linearly polarised case (b2) - indicating weaker alignment by the circularly polarised field. The intensity of the alignment pulse the same in both cases. The difference can be thought of as arising because in the circularly polarised case, the available alignment intensity is spread over two polarisation axes, rather than just one. Mathematically, this was observed in subsection 4.1.1 as an additional factor of $1/2$ being present in the expression for the potential energy of a molecule in a circularly polarised alignment field, compared to a molecule in a linearly polarised field (compare i.e. Eq. 4.21 and Eq. 4.23). As such, the degree of alignment appears to be lower as we are aligning two molecular axes with the circularly polarised field, so each is effectively aligned less strongly. In contrast, the degree of alignment appears to be higher with the linearly polarised field, as we align one axis very strongly, and have free rotation about Z into the plane of the detector. This free rotation around Z results in ions being ejected into the XY plane, which is only visible as a stripe along Y in our experiment, so the free rotation (and implicit lack of alignment) is not visible.

7.4 Imaging the dihedral angle of $(CS_2)_2$

Having conclusively demonstrated that the structure of $(CS_2)_2$ in HeDs is the cross-shaped structure shown in row (a) of Fig. 7.3, it is now demonstrated that the dihedral angle (the angle between the two CS_2 units in $(CS_2)_2$) can be imaged. This angle cannot be directly imaged via analysis of the $CS_2{}^+$ ion images, but can be obtained by analysis of the recoil velocities of the S^+ ions, and especially the angular covariance maps.

Figure 7.5 (a1) shows a S^+ image recorded with the probe pulse only (polarised along X), recorded under the MDC. As there is no alignment present, the CS_2 molecules are able to freely rotate, and as such S^+ ions are ejected completely isotropically, as the image shows. The center of the image is removed due to contamination with by singly charged molecular oxygen ($O_2{}^+$), that overlaps the S^+ channel at $m/z = 32$ Da. The corresponding covariance map (a2) also shows a very weak, broad area of signal either side of the central diagonal. This is evidence that two $CS_2{}^+$ ions are ejected, but there is insufficient statistics to see any clearer pattern in the covariance map. Figure 7.5 (b1) shows an analogous ion image, now recorded with an alignment pulse linearly polarised along Z present. The S^+ ions are now confined along the Z axis, demonstrating the 1D alignment of the CS_2 molecules by the laser pulse[2]. The corresponding covariance map (b2) shows a strong correlation between S^+ ions ejected at 0° and 180°, consistent with the ejection of an S^+ from either end of a Coulomb exploded CS_2 molecule.

Importantly, both of the images considered previously (Fig. 7.5 (a1) and (b1)) are taken under the MDC, so demonstrate the signature of S^+ ions from monomer-doped droplets, as dimer-doped droplets are almost absent under this doping condition. This is important, as it is not possible to differentiate the S^+ ions arising from monomer doped droplets based on their recoil velocities in the detector plane (as was the case for $CS_2{}^+$ ions). During the Coulomb explosion, an S^+ ion experiences the highest electrostatic repulsion from its neighbouring C^+ ion, and an S^+ ion produced from ionisation of $(CS_2)_2$ does not experience signifcantly more Coulombic repulsion than an S^+ ion produced from ionisation of CS_2.

Figure 7.5 (c1) now shows an analogous image to (a1), but recorded under the DDC. Aside from there being more signal, there is little visible difference between the two images. This is expected, for reasons given in

[2]The MPA is the internuclear axis of CS_2.

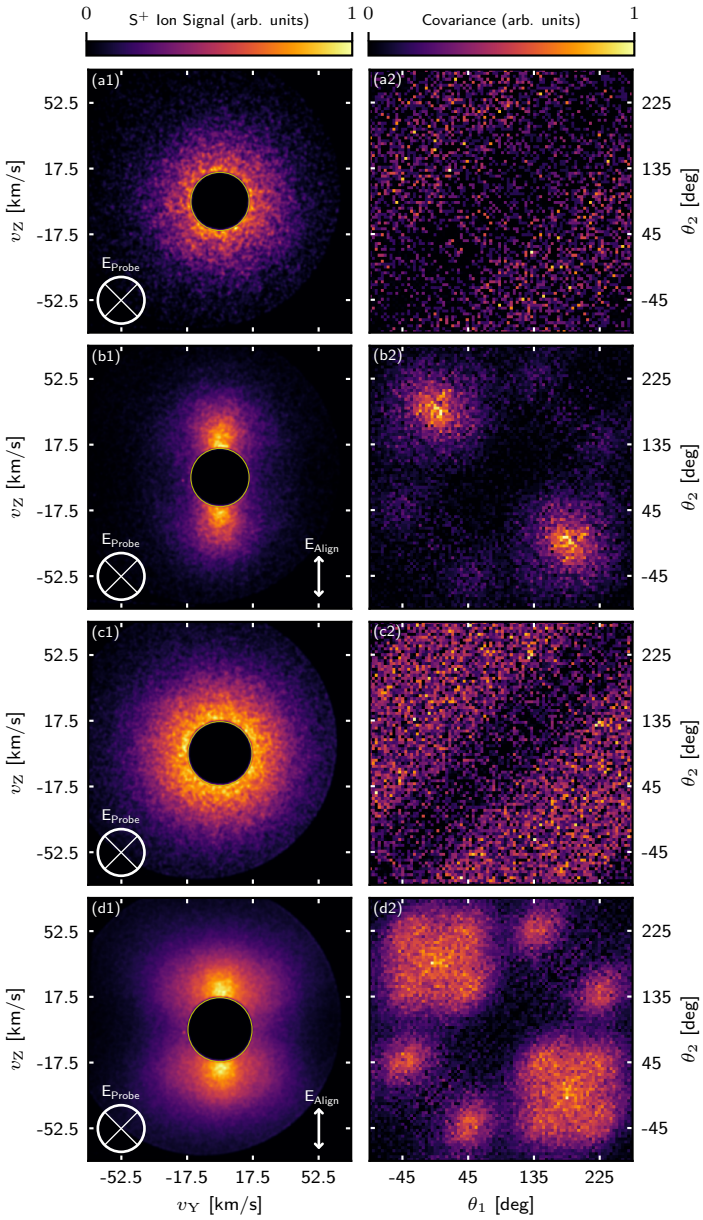

Figure 7.5: (a1)-(d1) S^+ ion images and (a2)-(d2) corresponding angular covariance maps. The polarisation state of the probe [alignment] laser pulse is shown in the lower left [right] corner of each ion image. Data in rows (a)-(b) [(c)-(d)] was recorded under the MDC [DDC]. The center is removed from each image due to contamination by $O_2{}^+$ (see text).

the previous paragraph[3]. The corresponding covariance map (c2) shows a stronger signal than (a2), but the signal is still almost entirely featureless, extending as a broad stripe either side of the central diagonal. All of these observations are entirely consistent with an unaligned ensemble consisting of both CS_2 and $(CS_2)_2$.

Figure 7.5 (d1) shows an analogous image to (c1), but with an alignment pulse present, polarised along Z. There is a clear and dramatic change. The ion image (d1) has gone from being isotropic to being composed of two lobes, and the previously featureless covariance map has resolved into a highly structured one. First considering the covariance map, it is clear that monomer signal at (0°, 180°) is still present, but now signals arising from explosion of $(CS_2)_2$ stand out much more clearly. These signals are approximately centered at (−45°, 45°), (−45°, 135°), (−45°,225°), (45°, 135°), (45°, 225°), (135°, 225°), with six equivalent positions obtained by mirroring the covariance map in the central diagonal. These correlations all show an angle of 90°, 180°, or 270° for the angle between recoiling S^+ ions. At first glance, this is completely consistent with the explosion of a cross-shaped CS_2 dimer, where the dihedral angle is expected to be 90°. However, a deeper analysis of this covariance map provides more insight.

7.4.1 Projection of the S^+ ions under the alignment field

With the alignment pulse linearly polarised along Z, the LPA (IMA) is aligned orthogonal to the Z axis, but the dimer should be free to rotate around the Z axis. Thus, one might expect that the covariance signals would extend as broad stripes, rather than localised islands, reflecting the free rotation. Row (a) in Fig. 7.6 shows a sketch of three different dimer orientations, imposed by the alignment pulse, as seen in perspective in the space-fixed frame. The dimers are sketched with the expected 90° dihedral angle between the two monomers. Row (b) shows the resulting S^+ ion emission directions in the detector (YZ) plane, assuming that the S^+ ions recoiling along their parent C-S bonds, and row (c) shows a sketch of the final, velocity-mapped, image. The dimers sketched in row (a) are depicted for three different angles, α, between the IMA and X axis, $\alpha =$ 0°, 45°, 90° ((a1), (a2), and (a3) respectively). The detector records the projection of the angle between the S^+ ion recoil directions (termed β), and it is clear that only in the case that α =0° does this angle correspond

[3]Astute readers may say that the average velocity of ions appears to be higher in image (c1) than in (a1). This is the case, but is due to the much larger number of ions, which make the outer regions of the image more visible with this colour map.

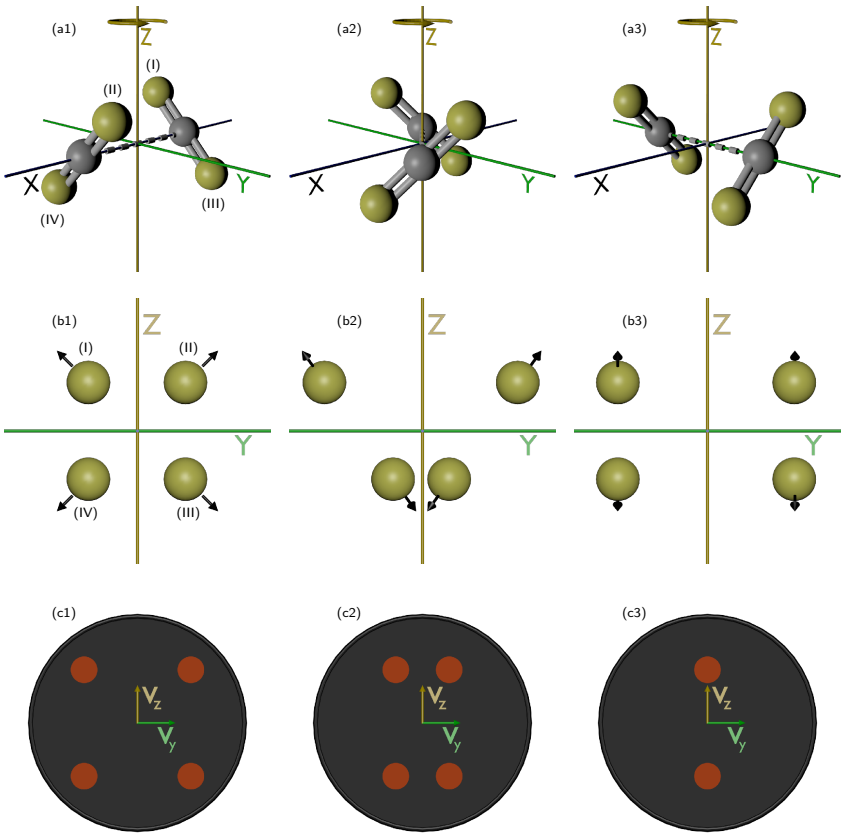

Figure 7.6: (a1)-(a3) Perspective view of the dimer for three rotation angles α, around the alignment polarisation (Z) axis. (b1)-(b3) The velocities of the recoiling S^+ ions in the detector (YZ) plane. (c1)-(c3) Sketches of the resultant velocity-mapped images from each rotation. Velocities along the Z and Y axes, V_Z and V_Y are annotated on each sketched image.

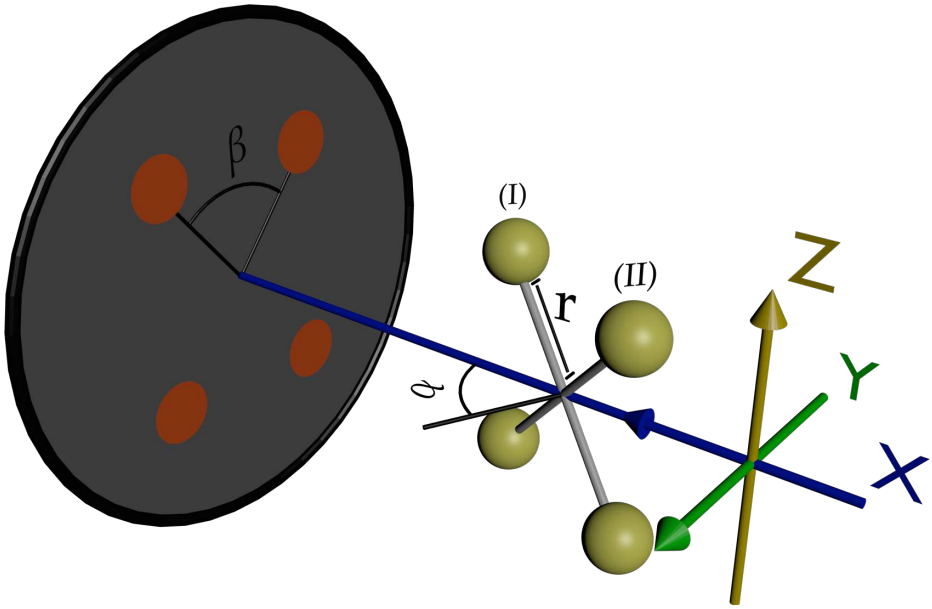

Figure 7.7: A schematic representation of the coordinate frame used to derive a relation between α and β. The alignment laser is polarised along Z.The angles α and β are shown on the drawing for an arbitrary rotation of the dimer.

to the true angle between the C-S bonds in $(CS_2)_2$. As α nears 90°, the projected angle nears 0°. The question then still stands, as to why the covariance map exhibits such localised signal when the projected angle can vary between 0° and 90°. This can be answered by considering the geometry of the projection.

Figure 7.7 shows a schematic representation of the projection of S^+ ions onto a detector. The angles α and β are shown on the sketch, and are defined as the angle betwee the C-C axis and the X axis (α), and the angle between the two sulphur atoms marked (I) and (II) (β). Taking the dihedral angle to be 90°, and placing the central point of the cross shape at the origin, we can define position vectors $\boldsymbol{n_I}$ and $\boldsymbol{n_{II}}$ for the positions of sulphur atoms I and II respectively, at an angle of α =0°:

$$\boldsymbol{n_I} = \begin{pmatrix} 0 \\ -\frac{r}{\sqrt{2}} \\ \frac{r}{\sqrt{2}} \end{pmatrix}, \boldsymbol{n_{II}} = \begin{pmatrix} 0 \\ \frac{r}{\sqrt{2}} \\ \frac{r}{\sqrt{2}} \end{pmatrix} \tag{7.1}$$

To account for the rotation of the dimer around the polarisation (Z) axis, we can then apply an arbitrary rotation matrix $\boldsymbol{R_Z(\alpha)}$ to each position

vector:

$$\boldsymbol{R_Z(\alpha)} = \begin{pmatrix} \cos\alpha & -\sin\alpha & 0 \\ \sin\alpha & \cos\alpha & 0 \\ 0 & 0 & 1 \end{pmatrix} \tag{7.2}$$

Letting $\frac{r}{\sqrt{2}} = r'$ for clarity, this results in the following position vectors as a function of α:

$$\boldsymbol{n_I(\alpha)} = \begin{pmatrix} r'\sin\alpha \\ -r'\cos\alpha \\ r' \end{pmatrix}, \boldsymbol{n_{II}(\alpha)} = \begin{pmatrix} -r'\sin\alpha \\ r'\cos\alpha \\ r' \end{pmatrix} \tag{7.3}$$

These position vectors can then be projected onto a the YZ plane by multiplication with a projection matrix. For an orthographic projection, this is given by the matrix $\boldsymbol{M_{Proj.}}$:

$$\boldsymbol{M_{Proj.}} = \begin{pmatrix} 0 & 0 & 0 \\ 0 & 1 & 0 \\ 0 & 0 & 1 \end{pmatrix} \tag{7.4}$$

Multiplication by $\boldsymbol{M_{Proj.}}$ results in the following expressions for $\boldsymbol{n_I}$ and $\boldsymbol{n_{II}}$:

$$\boldsymbol{n_{I,proj}(\alpha)} = \begin{pmatrix} 0 \\ -r'\cos\alpha \\ r' \end{pmatrix}, \boldsymbol{n_{II,proj}(\alpha)} = \begin{pmatrix} 0 \\ r'\cos\alpha \\ r' \end{pmatrix} \tag{7.5}$$

The angle between these two vectors is equal to β. Calculating the angle between these vectors by their scalar product results in Eq. 7.6 for the dependence of β on α.

$$\beta = \arccos\left(\frac{\sin^2\alpha}{\cos^2\alpha + 1}\right) \tag{7.6}$$

The functional form of β for the range $0° \leq \alpha \leq 180°$ is shown in Fig. 7.8 (a). From Eq. 7.6 the probability density function, $f_r(\beta)$, is determined. It is plotted in Fig. 7.8 (b) along with the probability distribution:

$$P(0 < B < \beta) = \int_0^\beta f_r(\beta')d\beta' \tag{7.7}$$

It is clear from Fig. 7.8 (b),(c) that the probability of measuring β at near 90° is much higher than the probability of measuring β at lower angles. This is illustrated in Fig. 7.8 (c), where the horizontal dotted line is at $P(0 < B < \beta) = 0.5$. It shows that the probability of measuring β

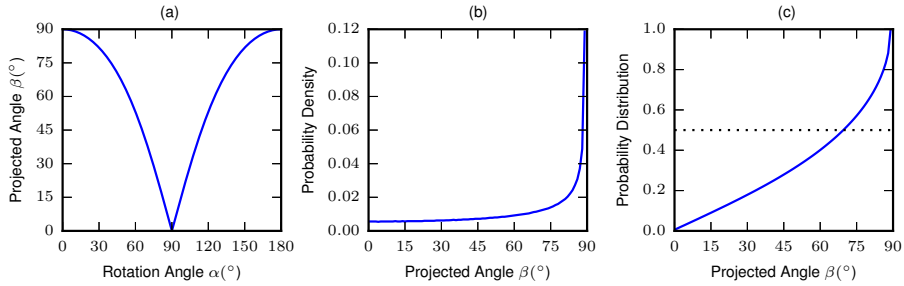

Figure 7.8: (a) Eq. 7.6 plotted in the range $0^\circ \leq \alpha \leq 180^\circ$. (b) The resulting probability density function $f_r(\beta)$. (c) The probability distribution $P(0 \leq B \leq \beta)$m defined according to Eq. 7.7. The dotted line in (c) is at $P = 0.5$.

between 0° and 70° is the same as the probability of measuring β between 70° and 90°. This explains the observations, that see localised islands in the covariance map rather than a broad stripe, despite the free rotation around Z.

7.4.2 Detailed Analysis of the Covariance Islands

We have so far seen that we can image the dihedral angle, and measure it to be a approximately 90°. A crucial question that remains unanswered, however, is why the covariance islands are observed at (−45°, 45°), and not at (0°, 90°); i.e. why is each CS_2 monomer in the dimer aligned at 45° to the alignment polarisation direction (as illustrated in Fig. 7.6 (a1)), and not at 0°?

If the angle between the CS_2 monomers in the dimer is 90°, then free rotation around the C-C axis would be expected due to the uniform polarisability in the molecular xz plane (see Fig. 7.1). This would create correlation stripes extending over 360° in the covariance map. Specifically, a stripe centered around $\theta_1 = \theta_2 + 90^\circ$ would be expected, at odds with the the three localised islands observed at (−45°, 45°), (45°, 135°), and (135°,225°). The explanation for this behaviour is that under the influence of the alignment field, the dihedral angle between the two CS_2 monomers deviates from 90°. This deviation can be understood simply as the alignment field trying to align each of the individual CS_2 monomers along the polarisation axis, but the torsional potential between the two monomers resists this, such that the two monomers settle at an equilibrium angle, determined by the minimum in the sum in the inherent torsional potential

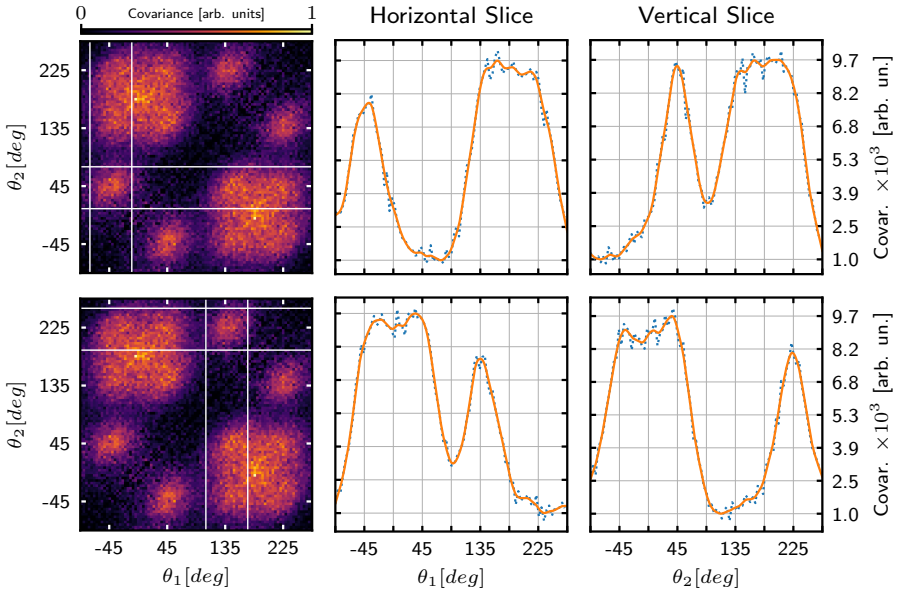

Figure 7.9: Covariance maps (left) with graphs (center and right) showing the intensity of the map integrated over a specific angular range. Each row corresponds to the integration of a specific covariance island (marked by the intersection of the two sets of white lines). The column headed 'horizontal slice' shows the integration of the covariance map between the two horizontal white lines. The column headed 'vertical slice' shows the integration between the two vertical white lines. On each graph, the raw data is plotted as a blue dashed line, and a FFT fit is overlaid in orange.

and the laser-induced alignment potential[4].

Any deviation from 90° should manifest itself in the covariance map shown in Fig. 7.5 (d2). From looking at the map as shown, this distortion is difficult to observe. However by integrating specific covariance islands along each axis, we are able to determine the exact center of the island. This is illustrated in Fig. 7.9. Analysis of these maps shows that the covariance islands approximately centered at (−45°,45°) and (135°,225°) are actually centered at (−39°,45°) and (137°,222°). These islands correspond to a dihedral angle of roughly 85°, compressed by 5° from the expected dihedral angle. Equivalently, the covariance islands approximately centered

[4]Attempts were made to calculate this torsional potential, and compare it to the intensity of the laser field. Accurately modelling this torsional potential proved difficult, due to the dispersion interactions inherent in it. Revisiting this problem is a potential avenue for further study.

at (−45°,225°) and (45°,135°) are expected to show an increase of around 5°. This cannot, unfortunately, be measured, as these covariance islands are heavily contaminated with signal from the strong covariance island at (0°,180°), so their centers cannot be reliably determined.

7.5 Summary

To summarise, we have shown that analysis of $CS_2{}^+$ ion images allows us to conclude that the structure of the CS_2 dimer inside He droplets is cross-shaped structure observed in the gas-phase. This structure is the only observed structure, so the dimer is not trapped in a non-ground state local minimum, as has been observed for other species in He droplets (see subsection 3.2.3). Analysis of S^+ ion images showed that the dihedral angle is somewhat distorted, an effect that is ascribed to the action of the laser field. Exploitation of this effect to inititate a torsion that can be imaged in real-time was attempted in Femtolab shortly after these experiments, but was not successful.

This chapter served to illustrate the experimental methods used throughout this work on a (relatively) simple system. The following chapters will firstly examine the alignment of this same system ($(CS_2)_2$) in a circularly polarised field in more detail, and then the same techniques will be applied to dimers and trimers of OCS molecules - a more complex system where more unexpected results were obtained.

CHAPTER 8

Intensity Dependent Alignment of $(CS_2)_2$

Having ascertained in chapter 7 that the structure of $(CS_2)_2$ in the droplet phase is the same as that of the gas phase (a cross-shaped symmetric top with D_{2d} symmetry), a more thorough description of the alignment dynamics in a circularly polarised laser field is now presented. This represents the first demonstration of the intensity-dependent alignment of a symmetric top in a circularly polarised laser field, and compares the intensity-dependent alignment to simulation. Firstly, the experimental results are presented, followed by a comparison with simulated results.

8.1 Experimental results

The experimental setup used to record the data is the same as in chapter 7. Ion images of CS_2^+ were recorded using a circularly polarised (in the XZ plane) alignment pulse and a linearly polarised (along X) probe laser pulse. The intensity of the probe laser pulse was $3 \times 10^{14}\,\mathrm{W/cm^2}$ and the intensity of the alignment laser pulse was varied to record a series of images at different alignment intensities. Images were recorded under the DDC. The ion images and corresponding angular covariance maps (calculated using ions outside the yellow circle) are shown in Fig. 8.1 (note that this figure extends over two pages).

It is clear from both the images (a1)-(i1) and covariance maps (a2)-(i2) that the degree of alignment increases as the intensity of the alignment pulse is increased. Fig. 8.1 (a1) shows an image recorded with no align-

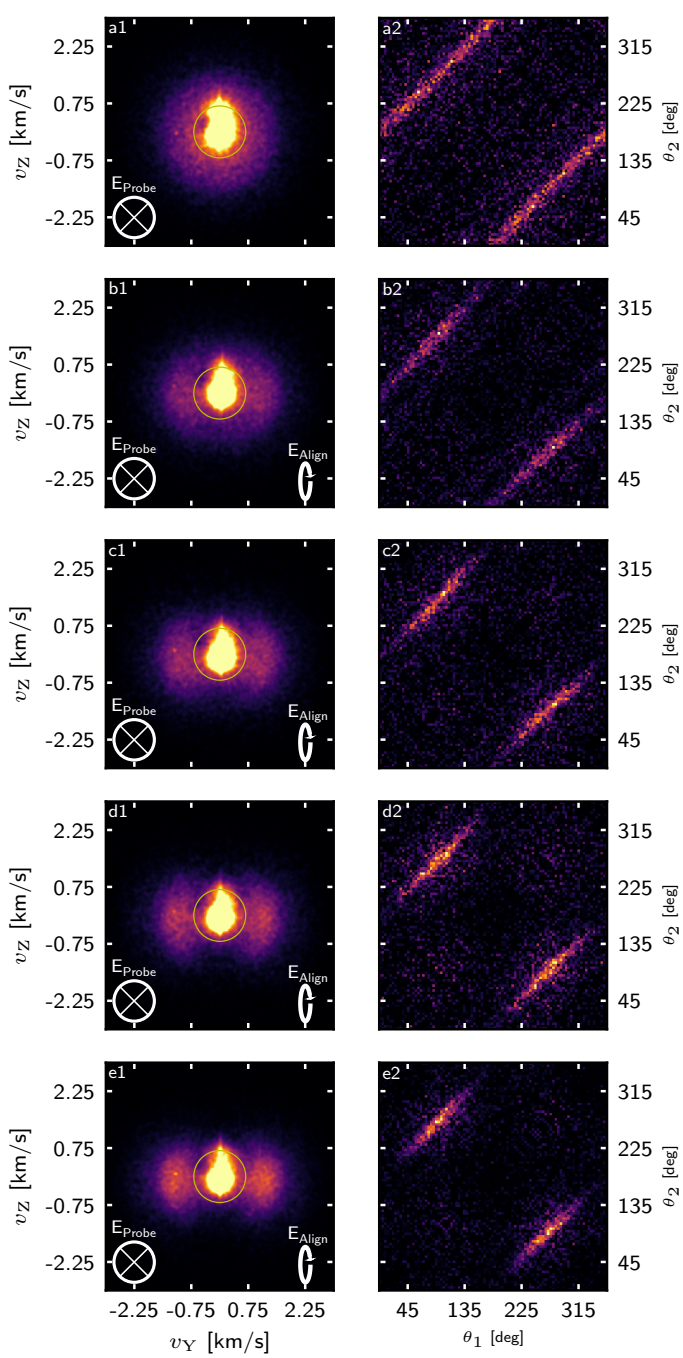
Intensity [W/cm^2]
a1
a2
b1
b2
c1
c2
d1
d2
e1
e2
E$_{Probe}$
E$_{Align}$
v_Z [km/s]
2.25
0.75
-0.75
-2.25
θ_2 [deg]
315
225
135
45
0
0.34×10^{11}
0.68×10^{11}
1.36×10^{11}
2.72×10^{11}
v_Y [km/s]
θ_1 [deg]

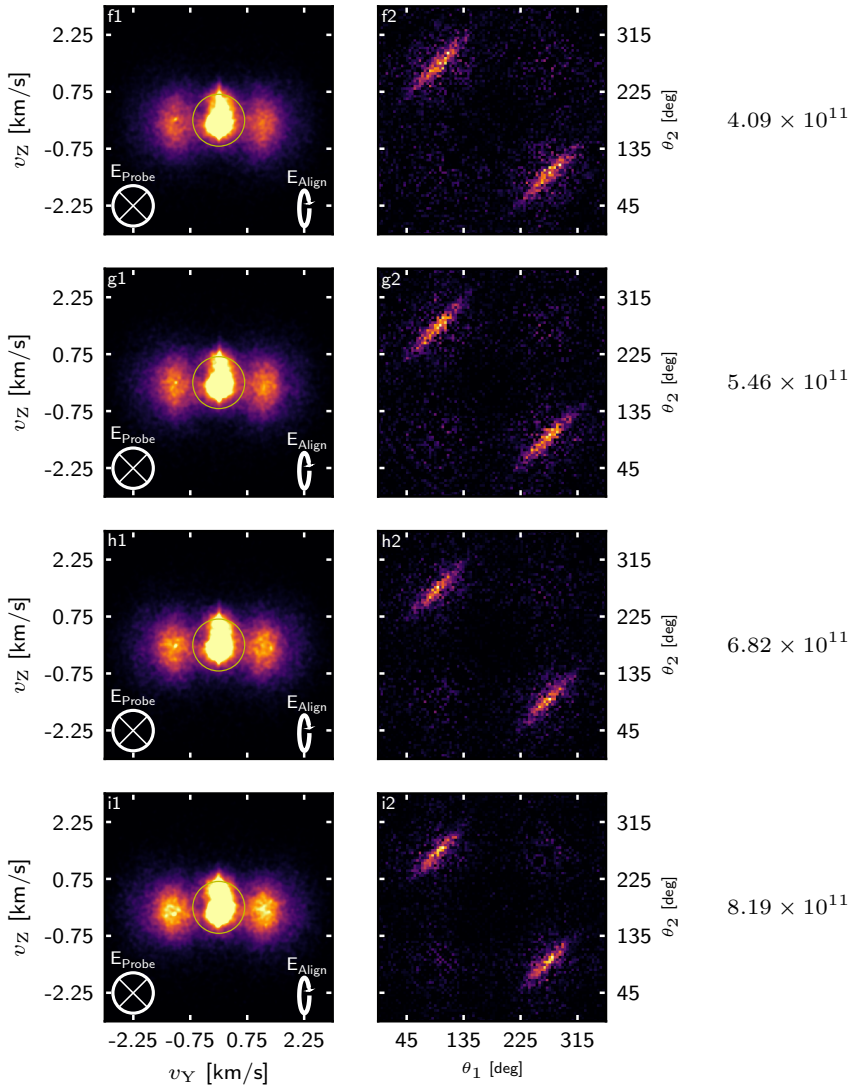

Figure 8.1: (a1)-(i1) CS_2^+ ion images and (a2)-(i2) corresponding angular covariance maps. The polarisation state of the probe (alignment) pulse is shown in the lower left (right) corner each image (a1)-(i1). Images were recorded under the DDC. The intensity of the alignment pulse used in each row (a)-(i) is shown to the right of the angular covariance map in each row.

ment pulse present, which is completely circularly symmetric - as expected in the case where there is no alignment. This is also corroborated by the signal in the angular covariance map, as there is a covariance signal at $\theta_1 = \theta_2 + 180°$ extending over the full 360° range. The alignment intensity was incremented in rows (a)-(i) from $0\,\mathrm{W/cm^2}$ to $8.2 \times 10^{11}\,\mathrm{W/cm^2}$, with the specific intensity used in each row annotated to the right of the angular covariance map in each row. Looking at panels (b1)-(i1), the circular symmetry is broken and the ion signal becomes more and more localised along the Y axis - indicating stronger alignment. The signal in covariance maps (b2)-(i2) also becomes a truncated island rather than a uniform line, and the island becomes more localised as the alignment power is increased - again indicating stronger alignment.

The increase in the degree of alignment can be quantified by calculating $\langle \cos^2 \theta_{2D} \rangle$ (see chapter 4). This can be calculated from the raw ion images (a1)-(i1). The value of $\langle \cos^2 \theta_{2D} \rangle$ obtained from the raw ion images is plotted in grey on Fig. 8.2. However, it is known that the recoil velocities of ions exiting HeDs (as in this case) are often somewhat scrambled, as scattering off the helium atoms as the ion leaves the droplet results in significant NAR. The consequence of this when measuring alignment is that the degree of alignment calculated from the ion images is an underestimate of the true degree of alignment. This is problematic, but can be ameliorated via deconvolution of the NAR from the angular covariance map [142]. An outline of the deconvolution process was given in chapter 4. The value of $\langle \cos^2 \theta_{2D} \rangle$ obtained from this deconvolution are shown in black on Fig. 8.2. It is clear that the measured degree of alignment is higher when calculated using the deconvolution than from the raw images directly, and the deconvolution likely provides a more accurate measurement of how the molecular axis is actually aligned. In the next section, this result is compared with the calculated power-dependent alignment trace.

8.2 Alignment Simulations

The degree of alignment can be simulated for symmetric top molecules, using software developed within Femtolab by Anders Aspegren Søndergaard [163]. This software can quickly and efficiently provide the time-dependent alignment trace for a molecule, given both molecular parameters (polarisability, rotational constants), and experimental parameters (alignment laser intensity, alignment pulse duration, temperature of the molecular ensemble). In general, the program can only simulate 1D alignment using linearly polarised fields. However, it was shown in chapter 4

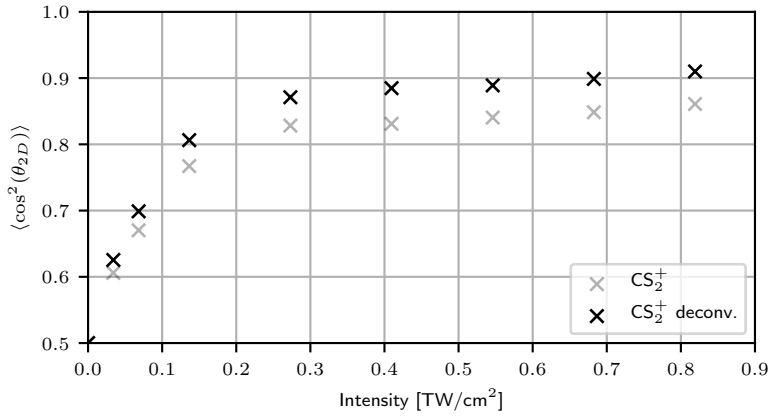

Figure 8.2: Degree of alignment ($\langle\cos^2\theta_{2D}\rangle$) of $(CS_2)_2$, calculated from $CS_2{}^+$ images directly (grey) and via deconvoluting the degree of alignment from the angular covariance map (black), as a function of alignment pulse intensity.

that aligning a symmetric top with circularly polarised light represents a special case which is completely analogous to alignment of a linear molecule with linearly polarised light. The arguments are briefly reiterated here for completeness.

8.2.1 Alignment with Circularly Polarised Fields

Circularly polarised fields, where the light is polarised in a plane perpendicular to the propagation direction of the laser field, can be used to confine the LPA of a molecule. The theory behind this has been covered in detail in chapter 4. It was shown that for a symmetric top molecule, the alignment potential in a circularly polarised field is given by:

$$\hat{V}_{\text{circ.}}(t) = -\frac{1}{8}E_0^2(t)[(\alpha_\perp - \alpha_\parallel)\cos^2(\theta) + \alpha_\parallel + \alpha_\perp] \tag{8.1}$$

Where $\alpha_\parallel$ is the polarisability along the symmetric top axis (the axis with a unique moment of inertia), and $\alpha_\perp$ is the polarisability along the two other axes. In line with the convention set out on page xi, θ is the angle between the symmetric top axis (y) and the axis orthogonal to the polarisation plane (the Y axis) of the laser field. Figure 8.3 shows the coordinate convention used with a model of $(CS_2)_2$, and the resulting potential $\hat{V}_{circ.}(t)$. It is clear from Fig. 8.3 that the potential is at a minimum when $\theta = (0, \pi)$. This can be interpreted as either the most polarisable plane (MPP) of the molecule aligning to the polarisation plane

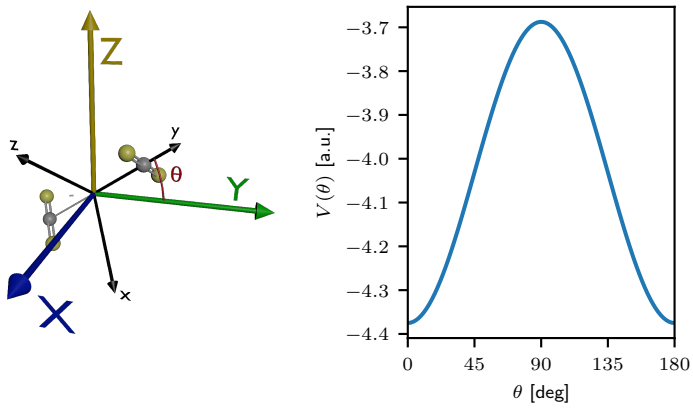

Figure 8.3: Left: the coordinate system used to derive Eq. 8.1, now with $(CS_2)_2$. Space fixed (molecule fixed) axes shown in colour (black). The angle θ between the y and the Y axis is illustrated. Right: $\hat{V}(\theta)$ plotted for $(CS_2)_2$ with typical laser parameters. The laser is circularly polarised in the XZ plane.

(xz $\rightarrow$ XZ); or equivalently as the least polarisable axis (LPA) aligning to the propagation direction of the laser field (y $\rightarrow$ Y).

Equation 4.23 shows that the degree of alignment will only depend on the polarisability anisotropy $\Delta\alpha = \alpha_\perp - \alpha_\parallel$ and the angle θ between the y and the Y axis. As such, the degree of alignment can be calculated using the software designed for use with linear fields, purely by changing the polarisability anisotropy.

8.2.2 Simulation Parameters

Here the parameters used in simulation, together with any necessary explanation, are presented.

Polarisability Elements

The structure of $(CS_2)_2$ in the HeDs is known to be cross shaped. The polarisability tensor of $(CS_2)_2$ can be qualitatively estimated by simply adding the polarisability tensors of two CS_2 molecules, rotated at 90° to each other. The polarisability elements of the dimer calculated in this way are given in the first line of Table 8.1. The assumption here is that there is negligible orbital interaction between the two CS_2 molecules (i.e. the interaction strength is purely electrostatic in origin). At first glance,

this may not appear to be a bad assumption, as orbital overlap should be fairly minimal for a vdW complex. However, if the total polarisability is calculated using DFT methods (wB97XD/aug-pcseg-2), assuming a separation of 3.5 Å, then the polarisability elements change, and the overall anisotropy $\Delta\alpha$ is reduced. This is shown in line 2 of Table 8.1.

Method	$\alpha_{\parallel}$ (Å^3)	$\alpha_{\perp}$ (Å^3)	$\Delta\alpha$ (Å^3)
Addition	10.8	19.9	9.1
DFT (3.5 Å)	12	17.5	5.5

Table 8.1: Polarisability elements parallel ($\alpha_{\parallel}$) and perpendicular ($\alpha_{\perp}$) to the y axis of $(CS_2)_2$ (see Fig. 8.3), calculated via addition of monomer polarisabilities, and via DFT methods. The polarisability anisotropy ($\Delta\alpha = \alpha_{\perp} - \alpha_{\parallel}$) is shown in the third column.

Rotational Constants

The calculated rotational constants of isolated $(CS_2)_2$ are given in the first line Table 8.2. $(CS_2)_2$ is a prolate top[1]. The rotational constants were calculated using the ground-state geometry in the gas phase [46]. However, from the very early days of HeD research, it was established that rotational constants of molecules in HeDs are often reduced by a factor of 2-4 when compared to isolated molecules [9]. The rationale for this is that as the molecule rotates, it drags a solvation shell of helium with it, increasing the effective moment of inertia, lowering the rotational constant. From prior work in Femtolab, we know that the moment of inertia of single CS_2 molecules solvated in HeDs increases by around a factor of 3 relative to an isolated molecule. Assuming a similar increase for $(CS_2)_2$, the adjusted rotational constants are shown in the second line of Table 8.2. In practice the adjusted rotational constants do not affect the maximum measured degree of alignment for adiabatic alignment very much [164], having much more of an effect in non-adiabatic alignment where the adjusted rotational constant will affect the measured revival times. The adjusted rotational constants are used in the calculation here.

[1]Rotational Constants $A > B = C$.

System	A(GHz)	B(GHz)	C(GHz)
$(CS_2)_2$	1.637	1.153	1.153
$(CS_2)_2$-He	0.546	0.384	0.384

Table 8.2: Rotational constants calculated for isolated $(CS_2)_2$ and for $(CS_2)_2$ in HeDs ($(CS_2)_2$-He). The constant A is calculated around the y axis, with B and C calculated around the x and z axes respectively (see Fig. 8.3). The helium-adjusted rotational constants were calculated assuming that the moment of inertia was increased by a factor of 3.

Laser and Misc. Parameters

Laser parameters used in the simulation are summarised in Table 8.3. The initial rotational state distribution of the molecules was chosen to be a Boltzmann ensemble at a temperature of 0.38 K. 20 focal volume averaging shells were used in each simulation[2] .

Parameter	Value
Peak intensity	0 TW cm^{-2} to 0.8 TW cm^{-2}
Pulse duration (FWHM)	160 ps
Alignment beam waist	35 µm
Probe beam waist	25 µm

Table 8.3: Laser parameters used in to calculate a simulated alignment trace. The beam waist refers to half of the $1/e^2$ width of one dimension of a 2D Gaussian fit across the laser focus. The laser foci are assumed to be circular.

8.3 Comparison of Simulation and Experiment

Simulated and experimental results are plotted in Fig. 8.4. Simulated data is shown with circular markers and a dashed line, whereas experimental data is shown with cross shaped markers. Generally it can be seen that the observed degree of alignment rises rapidly as the intensity increases, before levelling out at higher intensities as the rotational transitions become saturated. The raw CS_2^+ trace (without deconvolution) is shown in

[2]Focal volume averaging accounts for the spatial variation in alignment intensity over the laser focus.

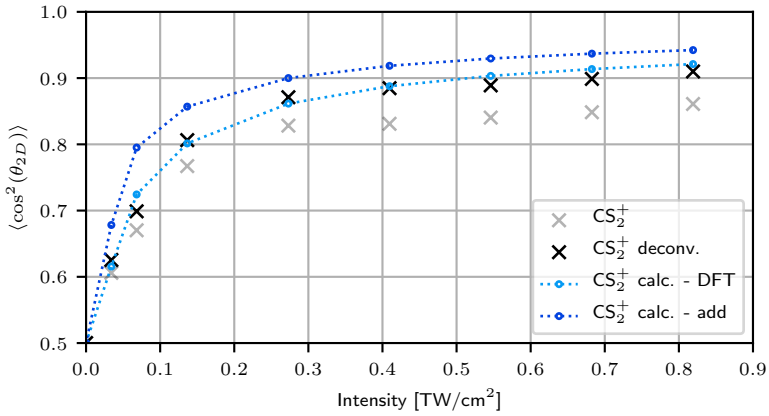

Figure 8.4: Experimental (crosses) and simulated (circles) degree of alignment of $(CS_2)_2$ as a function of alignment intensity. The alignment was induced adiabatically by a circularly polarised laser pulse. Alignment traces for both raw and deconvoluted data are presented (see text).

grey, and the maximum degree of alignment measured here is much lower than any other trace. The deconvolution $CS_2{}^+$ trace is shown in black, and a much higher degree of alignment is observed. This trace overlaps almost completely with the simulated trace calculated using the polarisability anistropy calculated using DFT methods (shown in light blue). The topmost (dark blue) trace is a simulated trace, calculated using the polarisability anistropy obtained by adding the polarisability tensors of two CS_2 monomers.

Considering this result, it is clear that the best match between theory and experiment is obtained between the deconvoluted trace and the simulated trace calculated using the polarisability anisotropy from DFT calculation, rather than that obtained by adding the polarisability of the two monomers. It is unsurprising that the deconvoluted trace fits the calculated trace better than the raw (non-deconvoluted) trace, as the deconvolution has been shown to provide a better measure of the alignment of the molecular axesthan the raw traces for other systems [162].

It is, however, perhaps surprising that the polarisability calculated using DFT is more accurate than that obtained simply adding the polarisability tensors of the two monomers. The polarisability anistropy is lowered (relative to the added case) when the polarisability elements are calculated using DFT. On the one hand, it may seem obvious that DFT would provide a more accurate answer than the hand-waving method of

adding the tensors. However, that the DFT calculation fits the observed degree of alignment better indicates that there is some electronic interaction between the two CS_2 monomers when the dimer is formed (as the addition assumes there is no interaction). This is perhaps surprising, as for a vdW complex there is expected to be minimal orbital overlap (and therefore minimal electronic interaction), with the binding strength arising primarily from electrostatic interactions (see chapter 3). The results here suggest that there is some non-negligible orbital overlap contributing to the binding strength - it is unclear how the polarisability would be reduced in the dimer otherwise. This shows the potential utility of LIA as a diagnostic tool for studying non-covalent interactions, and may (with further analysis) provide some deeper insight into the electronic structure of the complexes.

8.4 Summary

This chapter has expanded on analysis in the previous chapter and shown that a thorough understanding of the alignment behaviour of a weakly-bound molecular dimer can be gained by comparison to simulation. In addition to this, it was shown that comparisons to simulated alignment traces potentially could be very useful in studying non-covalent interactions, as they can be used to estimate the true polarisability of a weakly-bound complex. The next chapter takes the techniques presented in the previous two chapters and applies them to more complex systems, dimers and trimers of OCS.

CHAPTER 9

Alignment and Imaging of OCS Oligomers

In this chapter, LIA and CEI are used to determine the structure of dimers and trimers of OCS molecules embedded in HeDs. This represents an increase in complexity compared to the systems studied in the previous two chapters. The format of the analysis mirrors that of chapter 7, where a number of possible structures are initially considered, and then compared to the experimental observations.

9.1 Background

The experimental setup is entirely analogous to that described in the previous chapters, with some minor differences. Firstly, OCS is a gas at room temperature, so a pressurised cylinder of OCS is attached to the pickup cell rather than a liquid sample reservoir. Secondly, the HeDs are now formed by expanding He gas at 14 K and 30 bar. The higher temperature is used for OCS (compared to 16 K for CS_2), as this creates larger droplets (∼10000 He atoms on average) . Using larger droplets results in a larger pickup cross-section, which will increase the amount of He droplet signal relative to any deletrious effusive background signal. The effusive background when using OCS is larger than that for CS_2, because it has a higher vapour pressure and is less effectively trapped on the cold traps. Larger droplets were therefore used to increase the amount of droplet signal, as at 16 K the relative amount of effusive background was too high. However, this comes at the cost of slightly worse NAR.

The laser parameters used were the same as described in chapter 7 for the study of the CS_2 dimer.

9.2 Doping Regimes

For the CS_2 dimer, it was shown that it was possible to increase or decrease the relative amounts of monomers and dimers in the HeDs by adjusting the partial pressure of CS_2 in the pickup cell. Here, an equivalent analysis is performed for OCS, and the pressure is now also optimised for the doping of trimers into the droplets.

Figure 9.1 (a1) shows an OCS^+ ion image recorded using a linearly polarised probe pulse polarised along the X axis (perpendicular to the detector plane). An intense signal is present in the central portion of the image, and some weaker signal occurs at larger radii. The OCS^+ ions produced via ionisation of OCS molecules in droplets containing only single OCS molecules will necessarily have a very low speed. Thus, we ascribe the intense central signal as resulting from ionisation of OCS monomers [1]. However, OCS^+ ions arising from Coulomb explosion of oligomers of OCS will have a non-negligible speed due to the Coulombic repulsion between two or more OCS^+ ions in the He droplet (see subsection 9.2.1 and section 5.2). We therefore ascribe the signal occurring at radii outside the innermost yellow circle in Fig. 9.1 (a1) ($v > 0.6\,\mathrm{km\,s^{-1}}$, where speed $v = \sqrt{(v_Y^2 + v_Z^2)}$ - see appendix A) as arising from Coulomb explosion of OCS oligomers.

Figure 9.1 (b1) shows the angular covariance map calculated over all ion hits outside the innermost yellow circle in Fig. 9.1 (a1). This shows that there are clear correlations between OCS^+ ions recoiling at $\theta_1 = \theta_2 + 180°$. This is consistent with a two-body breakup, and therefore Coulomb explosion of an OCS dimer ($(OCS)_2$) into a pair of OCS^+ ions. There is also some faint signal at different angles, at $\theta_1 = \theta_2 + 120°$ and $\theta_1 = \theta_2 + 240°$. This is inconsistent with a two-body break up as expected for $(OCS)_2$, but would be consistent with three-body break up of $(OCS)_3$, thus this signal is tentatively ascribed as such. Figure 9.1 (c1) shows the angular covariance map now calculated over all ion hits between the innermost and outermost ($0.6\,\mathrm{km\,s^{-1}} < v < 1.4\,\mathrm{km\,s^{-1}}$) yellow circles in Fig. 9.1 (a1). Here there is a marked reduction in the number of ions seen at angles other than $\theta_1 = \theta_2 + 180°$. Similarly, Fig. 9.1 (d1) shows the angular covariance map calculated over all ion hits outside of

[1] There is also possibly a small signal from $He_{15}{}^+$, which will overlap the OCS^+ in this central region

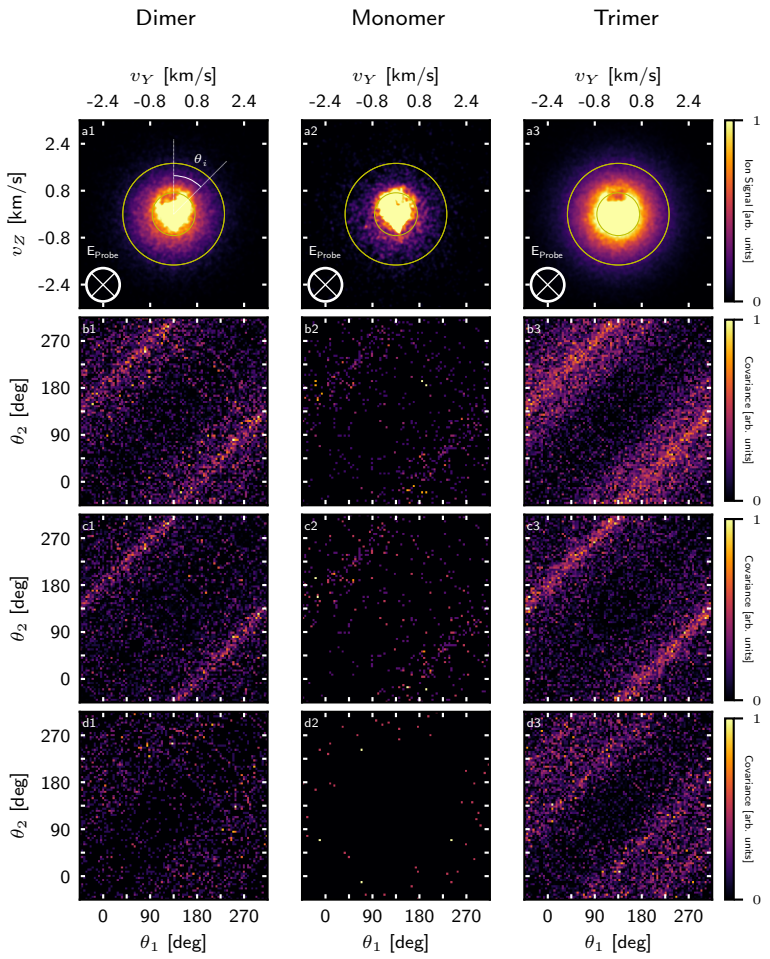

Figure 9.1: (a1)-(a3) OCS ion images and (b1)-(d3) corresponding angular covariance maps. The polarisation state of the probe pulse is given in the lower left corner of each image. Data in column (1) [(2)] {(3)} were recorded under the DDC [MDC] {TDC} (see text). Angular covariance maps in row (b) [(c)] {(d)} were calculated using all [dimer] {trimer} radii (see text). v_Y and v_Z are the velocity components of the speed v along the Y and Z axes respectively.

the outermost yellow circle in (a1) (v >1.4 km s^{-1}). Here none of the $\theta_1 = \theta_2 + 180°$ signal is present, instead only some very faint correlations consistent with the aforementioned breakup of $(OCS)_3$ present.

It is clear that selecting the radii in this way allows the ions resulting from Coulomb explosion of $(OCS)_2$ to be distinguished from those originating from explosion of $(OCS)_3$, as an OCS^+ ion arising from $(OCS)_3$ will experience Coulombic repulsion from two other OCS^+ partners, resulting in a higher speed. In contrast, an OCS^+ ion arising from Coulomb explosion of $(OCS)_2$ will only experience repulsion from one other OCS^+ partner, resulting in a lower speed. This can be quantified with electrostatic arguments, discussed in section 5.2, and reiterated with additional analysis in subsection 9.2.1. On this basis, we define the radii used in (b1) as 'all radii' (outside the innermost circle, $v > 0.6$ km s^{-1}); radii used in (c1) (between the innermost and outermost circles, 0.6 km s^{-1} < v < 1.4 km s^{-1}) as the 'dimer radii'; and radii used in (d1) (outside of the outermost circle, $v > 1.4$ km s^{-1}) as the 'trimer radii'.

It is clear that the majority of the signal in Fig. 9.1 (a1) arises from OCS monomers, but that there are a substantial amount of dimers present and a smaller amount of trimers. As such, this is defined as the DDC. As seen previously, it is then possible to enhance or reduce various parts of this signal by altering the pressure of the OCS gas in the pickup cell. Figure 9.1 (a2) shows an OCS^+ image recorded with a much lower partial pressure of OCS in the doping cell compared to the case of Fig. 9.1 (a1). It is evident from the angular covariance maps (Fig. 9.1 (b2)-(d2)) that there is markedly less $(OCS)_2$ present here, and very little $(OCS)_3$, as expected. There is still a visible monomer contribution in Fig. 9.1 (a2), thus this region is defined as the MDC. Finally, for the OCS^+ image in Fig. 9.1 (a3) the OCS pressure in the pickup cell was increased compared to the case of Fig. 9.1 (a1). Now it is clear that there are more ions outside the outermost yellow circle, and the covariance maps Fig. 9.1 (b3)-(d3) show an enhanced dimer and trimer signal compared to covariance maps Fig. 9.1 (b1)-(d1). As there are clearly substantially more trimers present under this doping condition, it is defined as the 'trimer-doping-condition' (TDC).

Table 9.1 gives the total number of ions inside the innermost yellow circle (monomers); between the two yellow circles (dimers); and outside the outermost yellow circle (trimers). The latter two of these radii correspond to the aforementioned dimer radii and trimer radii, where the former condition (inside the innermost circle) is referred to as the 'monomer radii'. As seen for CS_2, under all doping conditions there are more monomers

Doping Condition	Monomer (%)	Dimer (%)	Trimer (%)
Monomer	66.98	26.65	6.37
Dimer	54.88	34.96	10.16
Trimer	44.36	39.89	15.76

Table 9.1: The relative amounts of OCS^+ ions hitting the detector at different radii at the different specified doping conditions. The proportions are given relative to the total number of OCS^+ ions hitting the detector.

than dimers, and more dimers than trimers, but it is possible to increase the relative proportions of dimers and trimers by increasing the doping pressure.

9.2.1 Quantitative Analysis of Kinetic Energy Release

The assignment of monomer, dimer, and trimer radii can be justified using electrostatic arguments, as was detailed in section 5.2. Relevant parts of the analysis are reiterated here, together with an extension to another system relevant to the study of OCS oligomers.

Figure 9.2 shows possible arrangements of point charges that are based on the spectroscopically observed structures of $(OCS)_2$ and $(OCS)_3$ in the gas phase (images (a) and (b) respectively), and an arrangement based on a linear structure of $(OCS)_3$ for comparative purposes (image (c)). The total potential energy stored in each structure is annotated below each structure, where it is clear that the triangular structure (image (b)) stores the most electrostatic potential energy, and the dimer structure (image (a)) the least. The separation between each point charge was taken to be 3.7 Å, a reasonable approximation to the true separation in the gas-phase [165], as the true separation in He droplets has not been determined.

We now consider how the potential energy will be distributed into each constituent charge when they undergo Coulombic repulsion. In the triangular structure, the potential energy will be equally shared between each constituent ion, such that each OCS^+ ion would gain 3.89 eV of kinetic energy (corresponding to a maximum speed of around $3.5\,\mathrm{km\,s^{-1}}$ in the detector plane). Similarly, for the dimer structure each OCS^+ ion gains 1.95 eV of kinetic energy (a maximum speed of around $2.5\,\mathrm{km\,s^{-1}}$ in the detector plane). However, in the linear trimer structure, the central OCS^+ ion would experience an equal and opposite repulsion from each terminal OCS^+ ion, such that it would gain no net kinetic energy; thus the total stored potential is shared equally between each terminal OCS^+

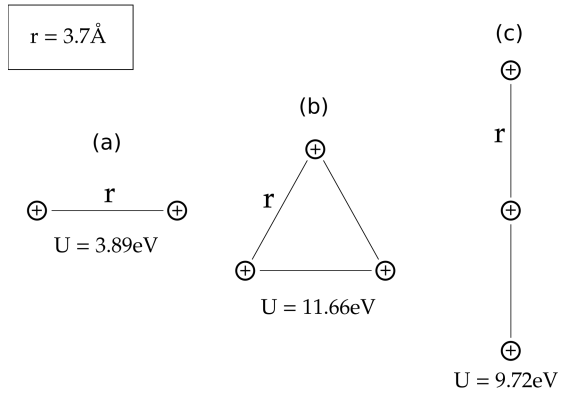

Figure 9.2: Sketches of arrangements of point charges in the dimer (a); triangular trimer (b); and linear trimer (c) geometries, used to estimate the potential energy U stored. The total potential energy U stored in each geometry is given below each drawing. The separation between two adjacent point charges r was taken to be 3.7 Å in all cases.

ion, each gaining 4.86 eV of kinetic energy (a maximum speed of around $4\,\mathrm{km\,s^{-1}}$ in the detector plane). This not only corroborates the conclusion of section 5.2 - that ions resulting from the explosion of different cluster sizes can be differentiated based on their speeds in the detector plane - but also demonstrates that in some cases, different shapes of cluster may be differentiated in an analogous way.

It is noteworthy that these calculated energies lead to speeds that are substantially greater than the empirical speeds discussed in section 9.2. For example, it was observed that ions with a speed above $1.4\,\mathrm{km\,s^{-1}}$ resulted from the explosion of $(OCS)_3$. This speed is vastly lower than the calculated speed of $3.5\,\mathrm{km\,s^{-1}}$, and similar observations can be made for other radii. We attribute the bulk of this effect to the kinetic energy lost by the recoiling OCS^+ ions as they scatter off He atoms on their way out of the droplet [87]. It is also possible that in HeDs the separation between OCS molecules within the different clusters differs slightly from that observed in the gas phase. However, these effects are expected to be minor compared to the effect of the He scattering.

9.3 OCS Dimer Structure

It is now shown how the experimental data allows the structure of $(OCS)_2$ inside HeDs to be determined. As previously, the strategy is to consider a

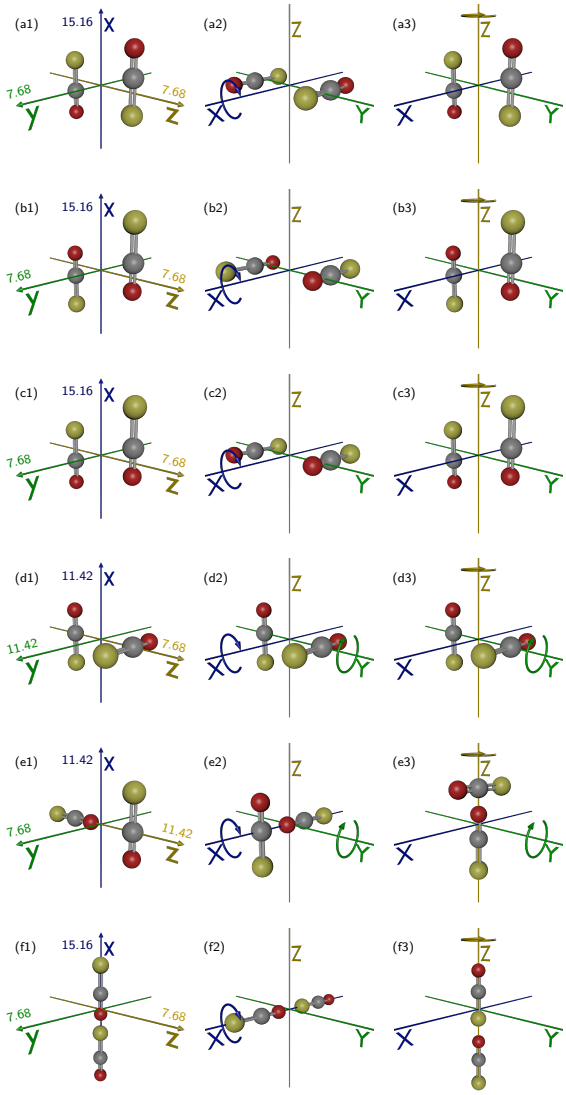

Figure 9.3: (a1)-(f1) Sketches of potential OCS dimer structures in the molecular frame, with their polarisability elements (α_x, α_y, α_z) annotated on the relevant axis, in units of Å^3 (see text). (a2)-(f2) [(a3)-(f3)] Sketches of how each structure would align in the laboratory (X, Y, Z) frame with an aligning laser field polarised along the X [Z] axis. The detector is placed in the YZ plane. Curved arrows indicate axes about which rotation is possible.

number of potential candidates for the structures and investigate if they are consistent with experimental observations. The candidates, with their structures sketched in Fig. 9.3 (a1)-(f1), were chosen due to their prior observation in the gas phase (a)-(c); or due to other small triatomics adopting analogous structures in the gas phase (d)-(f) [46, 52, 166]. The slipped-parallel sulphur-in structure shown in Fig. 9.3 (a1) has been identified as the gas phase ground-state structure of $(OCS)_2$ by IR spectroscopy [46], but it is known that HeDs can anneal non-ground state structures [68,166]. Thus, all six possible structures are considered initially.

To interpret the experimental data it is necessary to predict how each dimer structure considered aligns when exposed to the alignment pulse. This is possible if the polarisability tensor is known. Therefore, for each structure in Fig. 9.3 (a1)-(f1), the polarisability elements along each molecular axis (α_x, α_y, α_z) are given. The polarisability components for each dimer structure were calculated by summing the polarisability elements of the two monomers, with each rotated relative to each other as necessary. The neglect of the electronic interaction between the monomer units in each dimer will not qualitatively change the polarisability tensor of the dimer. The polarisability elements of the OCS monomer were taken to be $\alpha_{\parallel} = 7.58\,\text{Å}^3, \alpha_{\perp} = 3.84\,\text{Å}^3$ [167].

Figure 9.3 (a2)-(f2) shows how each potential structure would align in the laboratory (X, Y, Z) frame, under an alignment field linearly polarised along the X axis. A linearly polarised alignment field will align the MPA to the polarisation direction [126]. To reiterate, if there is not one single MPA, but two equally polarisable axes and one LPA, then the system will align such that either one of the most polarisable axes are parallel to the alignment field at any one time. To illustrate this, curved arrows on each sketch show axes where rotation (free or hindered) is possible under the alignment field. The detector is placed in the YZ plane. In cases where there are multiple possible aligned geometries, only one is shown in the sketch. Fig. 9.3 (a3)-(f3) shows analogous sketches for an alignment field linearly polarised along the Z axis.

Figure 9.4 (a1) shows an OCS^+ ion image, recorded under the dimer-doping-condition, with the probe laser polarised along the X axis, and no alignment laser present. There is clear circular symmetry in the image, but this image does not allow the dimer structure to be determined directly. The corresponding angular covariance map Fig. 9.4 (a2) is calculated over the dimer radii. This map shows a clear signature of a two-body breakup ($\theta_1 = \theta_2 + 180°$), as discussed in relation to Fig. 9.1, but similarly does not allow the structure of the dimer to be determined.

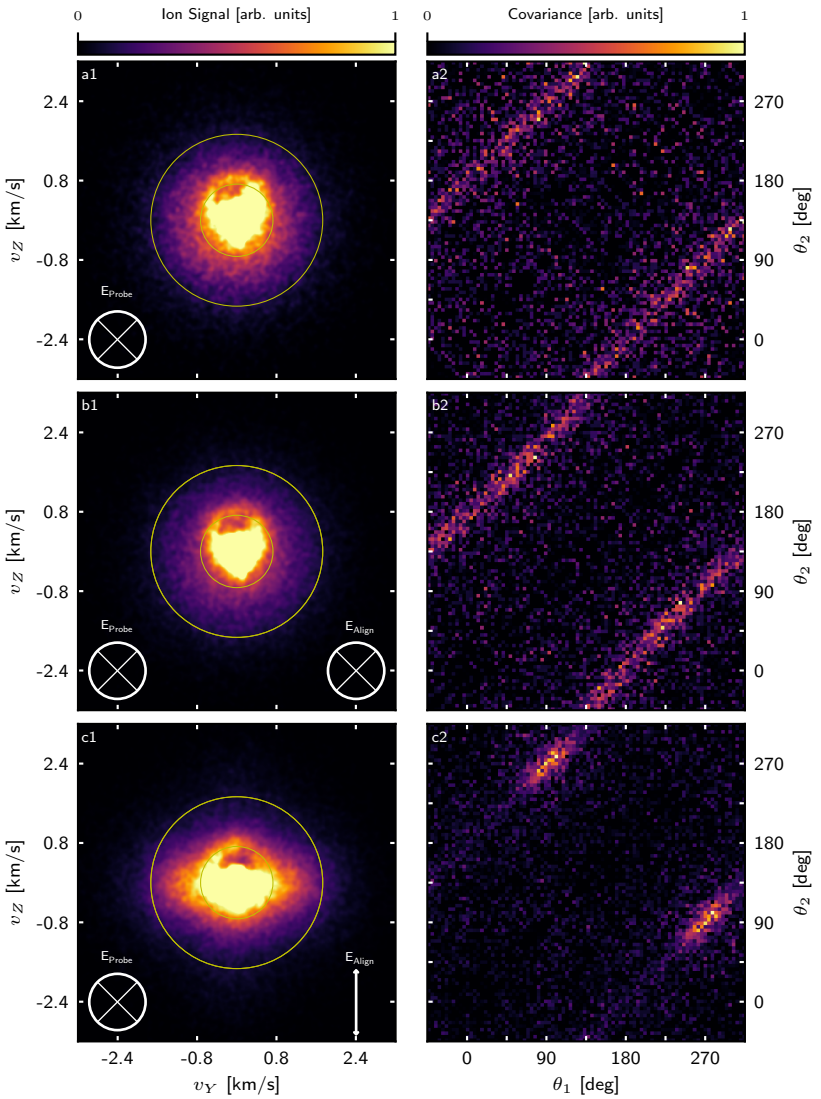

Figure 9.4: (a1)-(c1) OCS^+ ion images and (a2)-(c2) corresponding angular covariance maps. All images (a1)-(c1) were taken under the dimer-doping-condition, and all covariance maps (a2)-(c2) were calculated using the dimer radii. The polarisation state of the probe (alignment) laser is shown in the lower left (right) corner of the ion images.

Figure 9.4 (b1) shows an OCS^+ ion image with the alignment laser pulse, polarised along the X axis, present. The expected alignment of each structure under this field is shown in Fig. 9.3 (a2)-(f2). The image is still circularly symmetric, with ions being ejected in the detector (YZ) plane. This implies that the IMA is free to rotate about the X axis, such that ions are ejected in the full 360° range.

The corresponding angular covariance map Fig. 9.4 (b2) shows a clear signal at $\theta_1 = \theta_2 + 180°$, evenly distributed over the full 360° range - again consistent with a structure that is free to rotate about the X axis. The observations are compatible with all structures illustrated in Fig. 9.3, except for the linear chain (f2), as all structures are either in, or can rotate into, a position where the IMA is in the YZ plane, and can freely rotate around the X axis. For the linear-chain structure the IMA would align along the X axis. Thus, the OCS^+ ions would recoil perpendicular to the YZ plane and end up in the center of the detector. As such the ion image does not allow us to conclude if the linear structure is present or not. To summarise, with the alignment pulse polarised along the X axis none of the potential structures can be discounted.

Figure 9.4 (c1) shows an OCS^+ ion image with the alignment pulse polarised along the Z axis. The expected alignment of each structure under this field is shown in Fig. 9.3 (a3)-(f3). The image is no longer circularly symmetric. Rather the ions extend as a broad stripe along the Y axis. This shows that the IMA is confined to the XY plane with free rotation around the Z axis. The corresponding angular covariance map Fig. 9.4 (c2) corroborates this, and shows a clear localised island at (90°, 270°) (and the equivalent at (270°, 90°) obtained by mirroring in the central diagonal). These observations are inconsistent with the T-shape structure (Fig. 9.3 (e)) and the linear-chain structure (Fig. 9.3 (f)). In both cases the IMA would be able to be aligned along the Z axis (as drawn), thus we would expect to see a recoil at (0°, 180°) for these structures (as part of a broad stripe for the T-shape, and as a localised island for the linear-chain). We can therefore conclusively discount these structures from consideration. However, the other structures (Fig. 9.3 (a3)-(d3)), are consistent with the current experimental observations. Thus, we cannot unambiguously determine which of these four structures $(OCS)_2$ exhibits in the HeDs from the OCS^+ ion images alone.

Figure 9.5 (a1) shows a S^+ ion image recorded with only the probe laser pulse, polarised along the X axis, taken under the DDC. The center is removed due to the presence of singly charged molecular oxygen ($O_2{}^+$) overlapping the S^+ channel at $m/z = 32$ Da. The presence of $O_2{}^+$ results

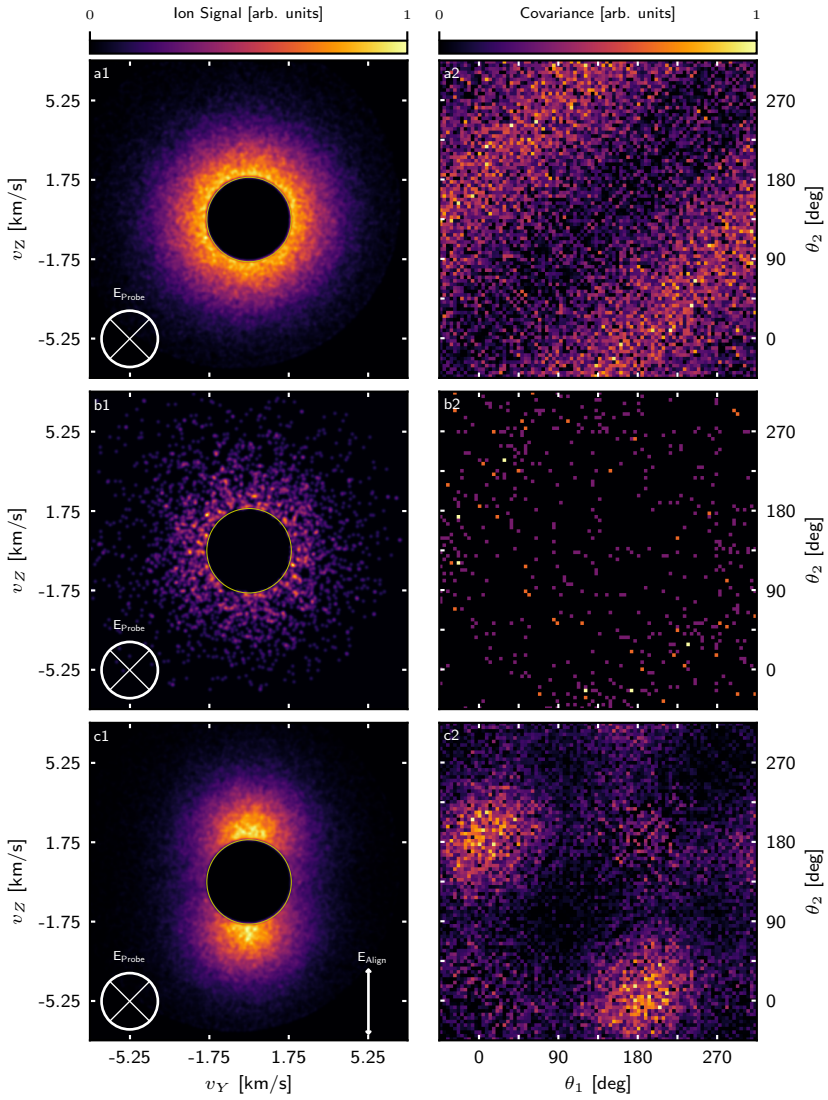

Figure 9.5: (a1)-(c1) S^+ ion images and (a2)-(c2) angular covariance maps calculated from ions outside the yellow circle. Images (a), [(b)], (c) were taken under the DDC [MDC] doping condition. The polarisation state of the probe (alignment) laser is given in the lower left (right) corner of the ion images. The center of each image is removed due to contamination by $O_2{}^+$ (see text).

in a very intense central spot, which renders the S^+ signal difficult to see if the center is not removed. This image is also circularly symmetric, expected for a probe pulse polarised perpendicular to the detector plane. The angular covariance map Fig. 9.5 (a2) is calculated using all ions outside the annotated yellow circle ($v > 1.65\,\mathrm{km\,s^{-1}}$). The observed broad stripe corresponding to $\theta_1 = \theta_2 + 180°$ reflects the circular symmetry of the ion image.

Figure 9.5 (b1)-(b2) show an analogous ion image and covariance map, now taken under the MDC. Here a marked reduction in the number of ions is observed, and almost no angular covariance signal is present. The lack of angular covariance signal for the S^+ ion is expected because Coulomb explosion of a monomer produces only one S^+ ion, i.e. there is no partner ion available to produce a correlation event. The logical consequence of this observation is that the covariance signal observed in Fig. 9.5 (a2) and (c2) must arise from the Coulomb explosion of $(OCS)_2$.

Figure 9.5 (c1) shows an analogous image to Fig. 9.5 (a1), but with the alignment pulse linearly polarised along the Z axis. Now the S^+ ions are confined along the Z axis, and the angular covariance map in Fig. 9.5 (c2) exhibits localised island at (0°, 180°) and (180°, 0°), demonstrating that the ions recoil in opposite directions along the Z axis. This 'back-to-back' recoil would only be observed if the two sulphur atoms of the dimer are oriented in opposite directions along the Z axis. Considering the remaining potential structures in Fig. 9.3 (a3)-(d3), it is clear that only the slipped-parallel S-in (Fig. 9.3 (a)) and slipped-parallel O-in (Fig. 9.3 (b)) fulfill this criterion. In contrast, the slipped aligned-parallel structure has both sulphur atoms oriented in the same direction along the Z axis, which would give rise to a covariance island at (0°, 0°). The cross-shaped structure would exhibit a covariance pattern with S^+ ions recoiling at around 90°to each other, similar to that observed for the CS_2 dimer in chapter 7 [154]. Thus, these two structures can be excluded, and we conclude that the structure of $(OCS)_2$ in HeDs is a slipped-antiparallel structure but we cannot conclusively determine if it is the O-in or the S-in structure (Fig. 9.3 (a) or (b)).

9.4 OCS Trimer Structure

Next it is shown how the experimental data allows the structure of the OCS trimer inside HeDs to be determined. The strategy is the same as for the dimer, i.e. analyse a selected number of potential structures and see if they are consistent with experimental observations. Figure 9.6 (a1)-

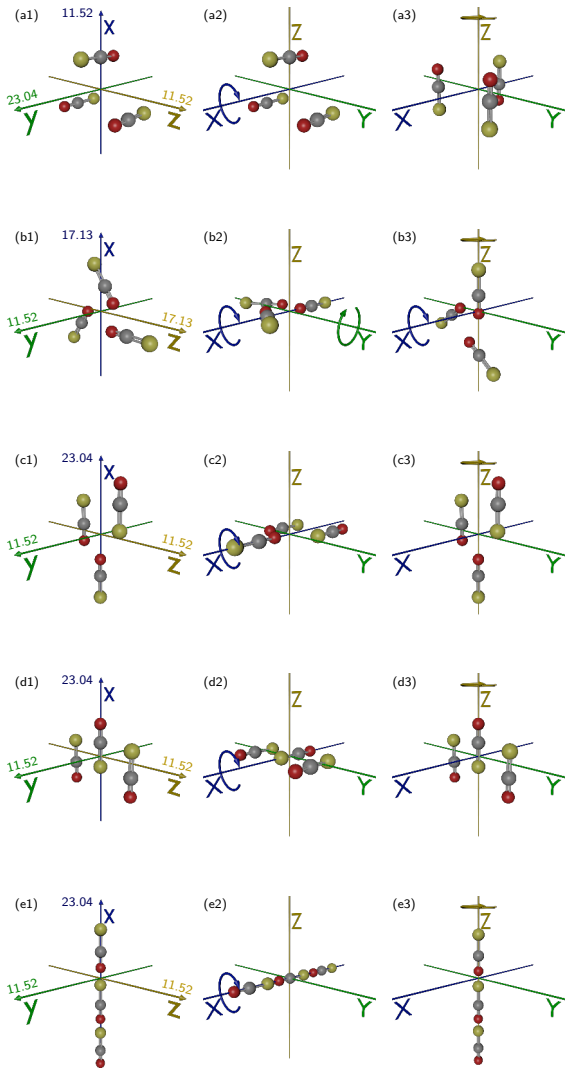

Figure 9.6: (a1)-(e1) Sketches of potential $(OCS)_3$ structures in the molecular (x, y, z) frame, with their polarisability elements (α_x, α_y, α_z) annotated on the relevant axis, in units of $Å^3$ (see text). (a2)-(f2) [(a3)-(f3)] Sketches of how each structure would align in the laboratory (X, Y, Z) frame with an aligning laser field polarised along the X [Z] axis. Curved arrows indicate axes about which rotation is possible.

(e1) show a series of possible structures for $(OCS)_3$, in the molecular (x, y, z) frame, with polarisability components annotated on the relevant axes. As for the dimers the polarisabilities were calculated by adding the polarisability tensors of the monomers in their respective orientations. The barrel-shaped structure shown in Fig. 9.6 (a1) is known to be the ground-state structure in the gas phase; and the triangle-shaped structure (Fig. 9.6 (b1)) is observed for $(CO_2)_3$ in the gas phase [46]. All other structures shown are not observed experimentally in the gas phase, yet are considered due to the effect of the He environment, as discussed previously. Structures shown in Fig. 9.6 (c1) and (d1) are obtained by adding a third OCS molecule to the ground state slipped-parallel S-in dimer (Fig. 9.3 (a1)), approaching along the molecular x axis (c1) and along the molecular z axis (d1), and will be referred to as the staggered-parallel and inline-parallel structures respectively. The linear chain-like structure shown in Fig. 9.6 (e1) is postulated to exist from theoretical work [168], and other polar triatomic molecules in HeDs have been shown to adopt such structures in prior spectroscopic work [166], thus we consider it here. It is germane to the discussion that it is plausible that we anneal multiple structures inside the HeDs.

Figure 9.7 (a1) shows an OCS^+ ion image, recorded under the TDC, with the alignment and probe pulse both polarised along the X axis. The alignment of each structure under this field is shown in Fig. 9.6 (a2)-(e2). As mentioned in section 9.2 there is necessarily a substantial amount of $(OCS)_2$ present here, and the angular covariance map calculated using the dimer radii (Fig. 9.7 (b1)) shows an identical pattern to that observed in Fig. 9.4 (b2)). However, there is clearly ion signal outside the outermost annotated yellow circle (trimer radii) in Fig. 9.7 (a1), which arises from Coulomb explosion of $(OCS)_3$ as discussed in section 9.2. The presence of this ion signal implies that at least one of the IMAs is in the YZ plane, such that OCS^+ ions recoil in the YZ plane as observed. Furthermore, at least one of the IMAs must be able to freely rotate around the X axis to account for the circularly symmetric ion distribution. Considering the aligned sketches, this is the case for all except the linear-chain structure (Fig. 9.6 (e2)). The corresponding angular covariance map calculated using the trimer radii is shown in Fig. 9.7 (c1), and shows a clear signature of a three-body breakup, with fragments being ejected at $\theta_1 = \theta_2 + 120°$ and $\theta_1 = \theta_2 + 240°$. This covariance pattern is only consistent with the barrel-shaped structure under this alignment field. Explosion of all other structures would result in at least one OCS^+ ion recoiling out of the YZ plane along the X axis, which would not result in the well defined emission angles in the YZ plane observed in the covariance map. Specifically,

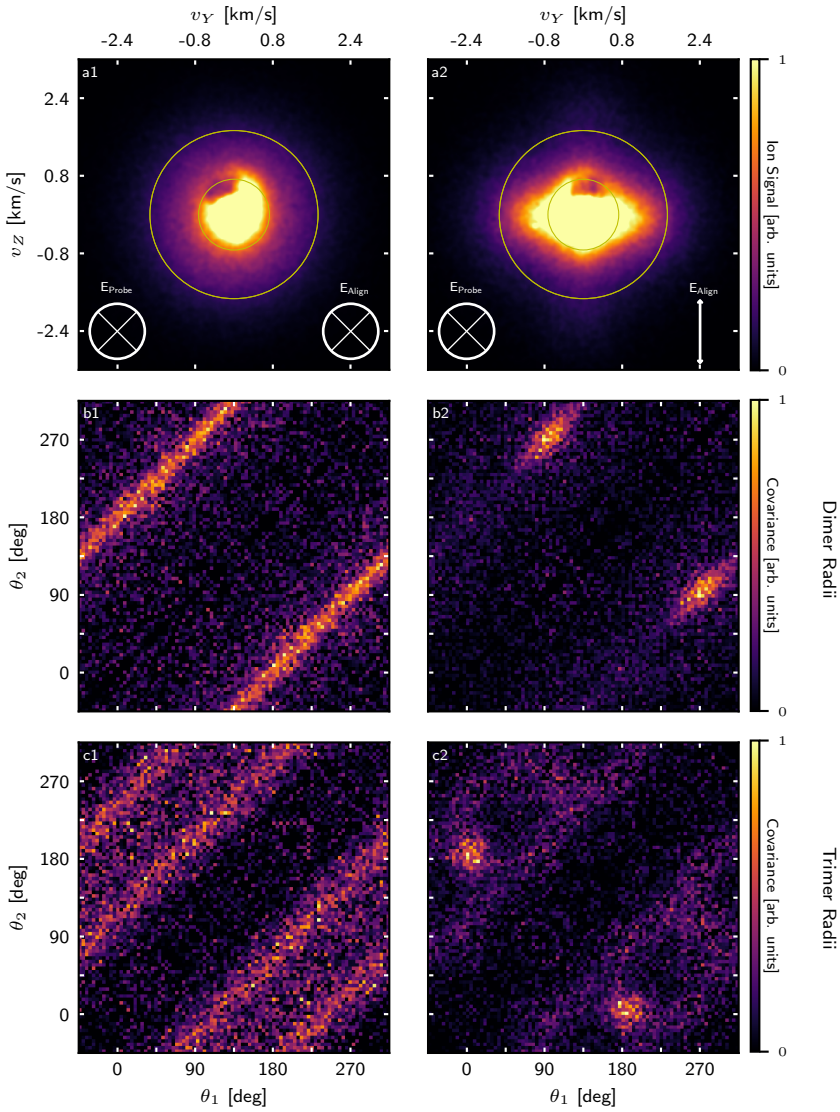

Figure 9.7: (a1)-(a2) OCS^+ ion images and (b1)-(c2) corresponding angular covariance maps produced using data recorded under the trimer-doping-condition. Data shown in column (1) [(2)] was recorded with an alignment field polarised along the X [Z] axis present. Covariance maps (b1)-(b2) [(c1)-(c2)] were calculated using the dimer [trimer] radii. The polarisation of the probe laser is shown in the lower left corner of each ion image.

Fig. 9.6 (b2)-(d2) could all result in a covariance map exhibiting a clear $\theta_1 = \theta_2 + 180°$ pattern. This is not observed, however it is now pertinent to consider the kinetic energy release from various structures in more detail.

Ion events are used to calculate the trimer-radii covariance map if they occur with a speed greater than $1.4\,\mathrm{km\,s^{-1}}$, measured in the YZ plane. If an ion event is produced with a speed greater than $1.4\,\mathrm{km\,s^{-1}}$, but with a substantial velocity component directed along the X axis, it could have a velocity of less than $1.4\,\mathrm{km\,s^{-1}}$ measured in the YZ plane, and thus overlap with dimer radii. Therefore, the absence of covariance at $\theta_1 = \theta_2 + 180°$ in Fig. 9.7 (c1) cannot conclusively exclude any structure that would result in this pattern, if there is a possibility that a substantial velocity component of the total ion speed is directed along the X axis. For example, structures shown in Fig. 9.6 (b2) and (c2) could both produce a circular distribution of ions with a covariance signal at $\theta_1 = \theta_2 + 180°$, but it could overlap with the $(OCS)_2$ signal, thus they cannot be discounted based on this data alone. Conversely, the structure shown in Fig. 9.6 (d2) would also produce a circular distribution of ions with a covariance signal at $\theta_1 = \theta_2 + 180°$, except now the central OCS in the structure will receive substantially less of the total kinetic energy (see subsection 9.2.1), resulting in the terminal OCS molecules having a higher velocity in the YZ plane. As a consequence of this, one would expect to see this covariance signal clearly in the trimer radii map shown in Fig. 9.7 (c1). This is not the case, and thus this structure can be conclusively discounted from consideration. To summarise, the presence of the barrel-shaped structure (Fig. 9.6 (a2)) has been conclusively demonstrated, and the structure in Fig. 9.6 (d2) has been conclusively discounted; but the other structures cannot be ruled out based on the information presented in Fig. 9.7 (a1)-(c1).

Figure 9.7 (a2) shows an OCS^+ ion image, recorded under identical conditions to Fig. 9.7 (a1), but with the alignment pulse polarised along the Z axis. Again there is a substantial amount of $(OCS)_2$ present, and the dimer radii covariance map (Fig. 9.7 (b2)) is identical to Fig. 9.4 (c2). The ion signal outside of the outermost yellow circle is no longer circularly symmetric. The corresponding trimer radii angular covariance map Fig. 9.7 (c2), shows a pronounced signal at (0°, 180°) and at (180°, 0°), together with some weaker structured background signal. The localised nature of these covariance islands implies that a structure in which the IMAs are aligned along the Z axis is present. Only the linear-chain structure (Fig. 9.6 (a3)) is consistent with this observation, as the IMAs are aligned along the Z axis under this alignment field, and the OCS^+ ions from the ends of the trimers will recoil in opposite directions along the

Z axis, in line with the observations. Thus the (0°, 180°), (180°, 0°) covariance signals are conclusively assigned as arising from the presence of a linear-chain structure. Now considering the weaker structured background signal, this shows a similar, albeit much weaker, signal to that observed in Fig. 9.7 (c1), with covariance signals at $\theta_1 = \theta_2 + 120°$and $\theta_1 = \theta_2 + 240°$. There is also a weak area of covariance signal centered around (90°, 270°). Each remaining potential structure is considered in turn with regards to these observations.

The barrel-shaped structure (Fig. 9.6 (a3)) will not produce the observed signal at $\theta_1 = \theta_2 + 120°/240°$, but would be expected to produce a signal at (90°, 270°), similar to the signal from $(OCS)_2$. This signal will largely overlap with the signal from $(OCS)_2$, but ions resulting from explosion of $(OCS)_3$ will gain more energy in the YZ plane, but not substantially more. This weak signal at (90°, 270°) is therefore assigned as arising from the barrel-shaped trimer. The trigonal-planar structure (Fig. 9.6 (b3)) could produce the signal at $\theta_1 = \theta_2 + 120/240°$, as it will align such that the plane containing the IMAs is in the YZ plane, producing the observed covariance pattern. The structure shown in Fig. 9.6 (c3) could also give rise to this covariance signal, in an analogous way to the trigonal planar structure. The presence of the structure shown in Fig. 9.6 (d3) has already been discounted based on Fig. 9.7 (c2), and it is evident that it would give rise to a broad covariance signal at $\theta_1 = \theta_2 + 180°$. This signal is not observed, corroborating the earlier conclusions. Therefore, the presence of a linear-chain structure (Fig. 9.6 (e3)) is conclusively demonstrated based on the data with this alignment polarisation; and it is speculated that the weak background signal at $\theta_1 = \theta_2 + 120/240°$ arises from either the trigonal planar structure (Fig. 9.6 (b3)) or the staggered-parallel structure (Fig. 9.6 (c3)). The weak background signal at (90°, 270°), arises from residual OCS^+ ions from the barrel-shaped structure.

Sketches in Fig. 9.6 show the individual OCS molecules oriented in specific directions. In the case of the barrel-shaped structure (a1), this is the expected structure from the gas-phase [46], and the linear-chain structure (e1) is shown with all dipoles aligned, as was observed for HCN inside HeDs, and would be expected to maximise the dipole-dipole interaction; and was also calculated to maximise the chalcogen bonding[2] [168]. However, it cannot be conclusively demonstrated that this is how the OCS molecules are oriented, as an equivalent analysis of the S^+ ion images as in section 9.3 is not possible under the TDC. This is because

[2]Chalcogen bonding can be thought of as analogous to hydrogen bonding, as part of a broader family of σ-hole interactions. The lone pair on a nucleophilic atom donates electron density into an electrophilic region of the C-X bond, where X is a chalcogen.

an S^+ ion arising from $(OCS)_3$ does not gain substantially more kinetic energy than an S^+ ion arising from $(OCS)_2$.

To summarise, at least two structures of $(OCS)_3$ in HeDs have been conclusively observed: the barrel-shaped structure (Fig. 9.6 (a)), previously observed in the gas phase; and the linear-chain structure (Fig. 9.6 (e)), not previously observed to our knowledge. We also speculate as to the presence of either a trigonal-planar or staggered-parallel structure, (Fig. 9.6 (b) or (c)), which has not previously been predicted for $(OCS)_3$. Of these two structures, one expects that the trigonal-planar structure (Fig. 9.6 (b)) is most likely, as it has been observed for CO_2 trimers previously in the gas phase [46], but the weak covariance signal means that this is only a speculation.

The observation of the multiple structures of $(OCS)_3$ in He droplets provokes considerable interest. There is a clear precedent for molecules inside HeDs to anneal into local minima on the global potential energy surface, and there is also a precedent for multiple structures to anneal inside HeDs [66,68,166]. However, complicating this is the fact that there is only one dimer structure observed in our experiments. The formation of a barrel shaped structure is easily understood by considering the addition of an extra OCS molecule to the observed $(OCS)_2$ structure, and the trimer can then be formed without substantial rearrangement of the present dimer structure. A trigonal-planar structure can be formed in a similar manner. However, we conclusively showed that there is no trace of a linear dimer in section 9.3. The implication of this is that the slipped-parallel dimer must rearrange upon the addition of a third OCS molecule into the HeD, to enable formation of the linear-chain trimer structure. The low temperature He environment might be expected to prohibit any such rearrangement of the dimer, however the extra energy released upon binding of a third OCS molecule may be sufficient to allow the weakly-bound dimer to rearrange into a linear structure - there is some precedent of such a rearrangement being possible [65].

To estimate how plausible this rearrangement would be, the energy difference between the barrel-shaped trimer and linear trimer has been calculated using CCSD(T) methods with a variety of basis sets. In all cases, the linear trimer is around $420\,cm^{-1}$ (50 meV) higher in energy than the ground state barrel-shaped structure. This energy is on the same order of magnitude as the binding energy of a typical vdW complex (usually on the order of $500\,cm^{-1}$), so it is not implausible that the binding energy released on addition of a third OCS molecule could result in the rearrangement of the complex.

One limitation of the technique, as discussed in section 9.4, is that we are unable to determine the orientation of each OCS molecule in the barrel-shaped and linear structures. One would, however, expect that the dipole-dipole interaction and possible chalcogen bonding [168] would stabilise the structure shown Fig. 9.6 (e1). Another limitation is that we are unable to determine accurate bond lengths from the kinetic energy of the fragments due to the energy loss from scattering of ions off the HeD. It is possible that this limitation can be overcome by measurements at several different droplet sizes to quantify how much energy is lost in the scattering process.

9.5 Summary

In summary, the structure of dimers and trimers of OCS molecules embedded in HeDs were identified by detecting correlations in the emission directions of the nascent OCS^+ or S^+ ions following CEI. The results show that the dimer is only formed in a slipped-parallel structure (as in the gas phase), whereas the trimer was identified in both the barrel-shaped (gas-phase) structure, and in a linear geometry. The latter, which has never been observed previously, demonstrates how HeDs enable the formation of molecular complexes in non-ground state configurations.

The work presented here relies crucially on the ability to detect intact parent ions from ionisation of strongly aligned molecules. The alignment occurs in the adiabatic limit implying that the parent ions created are exposed to the moderately strong ($I = 8 \times 10^{11}\,\mathrm{W/cm^2}$) alignment pulse. For OCS reported here as well as for CS_2 reported in the preceding chapters, the parent ions are not affected by the presence of the alignment field. For larger molecules, this is sometimes not the case, and the next chapter details attempted experiments on the dimers of anthracene molecules embedded in HeDs. These experiments required use of a truncated alignment pulse [169] to produced sufficient numbers of intact, aligned parent ions for study.

CHAPTER 10

Anthracene in Helium Droplets

The preceding results chapters have demonstrated that it is possible to form, align, and image dimers and trimers of small molecules inside HeDs. These experiments have proved that we have the experimental tools to manipulate such systems, but always represented only the first step of a wider project. Ultimately, there are a number of possible routes that this project could take. These include the formation and manipulation of much larger systems, and the study of time-resolved bimolecular processes. This chapter details initial attempts at both of these goals, by studying the vdW dimers and photodimers of anthracene (Anth) molecules in HeDs.

10.1 Motivations and Background

There are many motivations for wanting to extend the study of molecular complexes in HeDs to beyond small triatomic molecules, to larger (>150 Da) molecules. Larger molecules have more potential to exhibit interesting and unusual chemistry - with the possibility of studying complex intramolecular processes that do not exist for the small triatomic molecules currently studied. For example, intramolecular torsion of a heavily substituted biphenyl has been previously studied in the gas phase in Femtolab [57]; and intramolecular bond formation is a critical step in many important synthetic reactions, such as the Claisen rearrangement or the Dieckmann condensation [170]. Further to this, clusters of large molecules potentially have some interesting industrial uses, such as sin-

glet fission in dimers of polycyclic aromatic hydrocarbons (PAHs), which has the potential to dramatically increase the efficiency solar cells [171].

However, there are some additional challenges involved in studying such large molecules using the experimental techniques available in Femtolab, and especially in studying clusters of large molecules. As the size of the molecules increase, their vapour pressure drops, which means that it can be more difficult to bring the molecules into the gas-phase without extensive heating - problematic if the molecule is not thermally stable. If this is the case, it is even harder to generate clusters of such molecules. Using supersonic beams, it can be difficult to form clusters of very large molecules, even at the upper limits of the operating temperature of such valves. Finally, even if such clusters can be formed in a supersonic beam, the low-frequency vibrational modes will often not be efficiently cooled. This difficulty in cooling clusters of large molecules in seeded beams means that spectroscopic analysis is less insightful, as less of the molecules exist in their ground vibrational states. HeDs, then, provide an obvious solution to this problem, as very large molecules can be solvated into HeDs (provided the droplet is large enough and the molecule can be brought into the gas phase[1]) and are effectively cooled via helium evaporation. HeDs have previously been used to study clusters of very large molecules [172], and very large clusters of small molecules [173].

The second motivation mentioned, the study of time-resolved bimolecular processes, has been a long term goal within Femtolab. All the experiments described in this work have shown that it is possible to image the structure of aligned molecular clusters inside HeDs whilst retaining the inherent femtoscond time resolution of the probe process. The motivation to image a bimolecular process in real time (making a 'molecular movie') is almost self-evident. It could provide a major insight into the structure of reactive intermediates, which have never been directly observed, and could also facilitate a deep understanding of reaction mechanisms. So far, chemists know that such processes happpen (and that reactive intermediates exist), but can only directly observe the tracks that they leave behind. It has not been possible to pin down and photograph a transition-state, and this might be possible via time-resolved imaging of a bimolecular process.

Prior study of large molecules (and clusters of large molecules) solvated in HeDs have primarily been done using frequency resolved tech-

[1]While this may still be challenging, the requisite vapour pressure for the doping of a molecule into a HeD is lower than the pressure required to run it in (for example) and Even-Lavie valve.

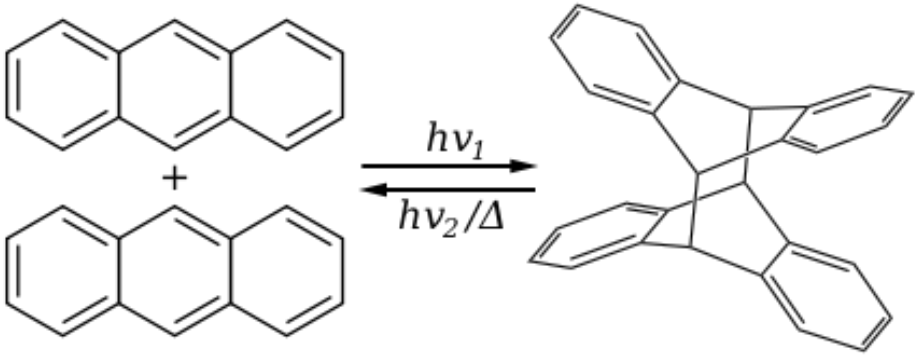

Figure 10.1: A schematic of the UV-induced dimerisation of anthracene (left) into dianthracene (right).

niques. Within Femtolab, it has been shown that it is possible to align and image large polycyclic aromatic hydrocarbons (PAHs), such as tetracene ($C_{18}H_{12}$), inside HeDs - but it has not yet proved possible to undertake a time-resolved study of any intra- or inter-molecular process inside HeDs beyond alignment dynamics.

10.1.1 Anthracene

Anthracene ($C_{14}H_{10}$) is PAH with a mass of 178 Da, consisting of three interlocking benzene rings. Anthracene was chosen for study within HeDs as it readily undergoes photodimersation when irradiated with UV light [174]. A schematic of this photodimerisation is shown in Fig. 10.1. Specifically, when anthracene is irradiated with UV light at a central wavelength of around 350 nm, it undergoes photodimerisation into dianthracene. This dimerisation is reversible, and heating dianthracene to above its melting point (∼553 K), or irradiation of the solution with UV light at a central wavelength of 300 nm or less will result in the dissociation of dianthracene into two anthracene molecules [174, 175].

10.2 Experimental Plan

The anthracene dimer represents a very interesting case for study inside HeDs. It should be possible to first form the vdW dimer of anthracene ($(Anth)_2$), and determine its structure by alignment and imaging as in the previous chapters. Having formed $(Anth)_2$, it may then be possible to induce the photodimerisation shown in Fig. 10.1 using a femtosecond UV laser pulse. In this way, it could be possible to follow the formation of the anthracene photodimer, dianthracene (Dianth- $C_{28}H_{20}$) by monitoring the

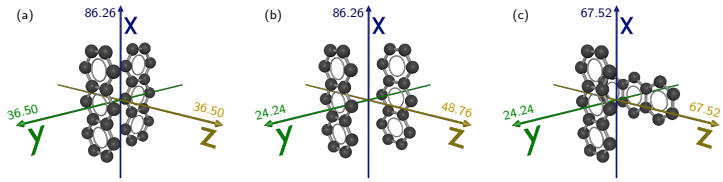

Figure 10.2: T-shaped (a), offset-parallel (b), and cross-shaped (c) structures for $(Anth)_2$. The structures are shown in the molecular frame, with the polarisability elements along each axis annotated in units of $Å^3$.

amount of dianthracene cations ($Dianth^+$) produced as a function of the delay between the UV pump pulse and ionising probe pulse.

10.2.1 The Anthracene vdW Dimer

The ground state structure of $(Anth)_2$ in the gas phase has been a topic of some debate historically. Three possible structures for $(Anth)_2$ are shown in Fig. 10.2. Initial studies by Chakraborty and Lim, and by Matsuoka *et al.* suggested that the ground-state structure was either a T-shaped dimer (panel (a) in Fig. 10.2) or an offset-parallel dimer (panel (b)). These assignments were made based on electronic spectroscopy and LIF [176, 177]. However, a later study by Piuzzi *et al.* showed that these prior studies had misassigned a band from the anthracene trimer as resulting from the anthracene dimer, and therefore claimed that the lowest energy structure was just the T-shaped structure (panel (a)) [178]. However, this study calculated that the lowest energy structure ought to be the cross-shaped structure (panel (c)). Many other theoretical studies of anthracene clusters found that the ground state should be the cross-shaped structure, but that the energy difference between all three structures mentioned was very low. Using the LIA combined with CEI technique described in the preceding chapters, it may be possible to determine the structure of $(Anth)_2$ in HeDs, providing a useful piece of evidence.

The polarisability elements of each dimer structure are annotated on the relevant molecular axes of Fig. 10.2. These were obtained by adding the polarisability tensors of anthracene monomers, rotated as necessary - this is not expected to qualitatively change the polarisability of the dimers, but will not provide an accurate quantitative estimate of the polarisability, as discussed in previous chapters. By considering how each structure will

align under differently polarised laser fields, we then hope to be able to ascertain the structure of the anthracene dimer inside HeDs. It is, of course, plausible that the structure of $(Anth)_2$ in HeDs is different to that in the gas phase, but nevertheless it would be an informative piece of evidence to add to the current discussion. The results from this part of the study are given in section 10.3.

Photodimerisation of Anthracene

If $(Anth)_2$ can be formed in HeDs, then it is also plausible that the photodimerisation of $(Anth)_2$ into Dianth can be initiated in the HeDs by a femtosecond UV laser pulse, as was illustrated schematically in Fig. 10.1. The first step in undertaking this (ambitious) experiment is to ascertain whether or not the final photodimer, Dianth, can be observed using our ionisation processes. This requires that Dianth is synthesised outside the vacuum chamber and doped into HeDs. If it is possible to make and detect Dianth, then the time-resolved photodimerisation can be attempted. A full account of the preliminary attempts at this experiment is given in section 10.4.

10.3 Structural Imaging of $(Anth)_2$

The structural imaging of $(Anth)_2$ was undetaken in a similar way to the structural imaging of $(OCS)_2$ and $(CS_2)_2$. Namely, a number of different possible structures were considered and then compared with the experimental results.

10.3.1 Experimental Setup

The imaging of $(Anth)_2$ was performed in the same way as was presented for $(CS_2)_2$ and $(OCS)_2$, using HeDs produced at a nozzle temperature of 16 K and 25 bar backing pressure. Other aspects of the experimental setup were slightly different to that described for CS_2 and OCS, and are detailed in the following sections.

Oven Doping

Anthracene has a much lower vapour pressure than either CS_2 or OCS. For this reason, it cannot be run in an external reservoir connected to a leak valve (as previously), but must be heated in an oven inside the vacuum chamber. The assembly of the oven and how it is mounted was discussed in subsection 6.1.2. Using an oven rather than a pickup cell

does not give fine, easily tunable control over a range of doping regimes. The oven generally takes some hours to heat up and stabilise at a given temperature (set by a constant current power supply), which adds considerably to the time taken to perform the experiment. Generally, one to three days must be taken initially to find oven currents where sufficient signal is seen, but where clustering is also controlled (i.e. the MDC/DDC is reached). The oven can also not easily be turned down once it is heated (it takes some hours to cool completely) - so care must be taken to ensure that it is not overheated. Despite these considerations, the oven has successfully been used to study large molecules such as tetracene, pentacene, diiodobiphenyl, and tetrabromoindigo in Femtolab, among others.

Anthracene proved an especially difficult molecule to run in the oven, as it has a higher vapour pressure than any other molecule that has been run in the oven before in Femtolab, but is not volatile enough to be run in an external reservoir. In practice, this means that at oven currents below around 900 mA, no usable signal was observable, but at oven currents over around 1200 mA the anthracene sample would be evaporated out of the oven and be rapidly deposited (over a period of around 2 h) onto the cold trap in front of the oven. This was problematic, as the vacuum must be broken to refill the oven and to clean the cold trap. Figure 10.3 shows the face of the cold trap near the oven under normal operation (panel (a)); and panel (b) shows the same face of the cold trap after anthracene has been run. It is clear that large deposits of anthracene form on the cold trap, which must be cleaned off (and the oven refilled) by breaking vacuum. Despite these complications, it is possible to run anthracene in the oven between the two limit currents listed (in general at around 1 A). Running at this oven current provides a usable (but small) level of $Anth^+$ signal for around 1-2 days before deposition onto the cold trap. Running at this current also produces some signal $Anth^+$ signal arising from Coulomb explosion of $(Anth)_2$, but it is difficult to move between a clear MDC and a clear DDC as was shown to be possible for OCS and CS_2.

Truncated Alignment Pulse

Aligning large molecules such as anthracene presents another difficulty that has alluded to at the end of the previous chapter. Namely, the parent cations of such large molecules readily undergo fragmentation due to the presence of the alignment pulse. Specifically, the parent cation can absorb many IR photons from the alignment pulse, resulting in extensive fragmentation - rendering the number of intact parent ions that survive to reach the detector very low. This is problematic if the observation of

(a) **(b)**

Figure 10.3: (a) The face of the cold trap nearest the oven, before anthracene has been run. (b) The same face of the cold trap, after a day of running anthracene in the oven.

intact parent ions from aligned molecules is desired, as is often the case when studying molecular dimers and trimers.

This situation can be ameliorated by using a truncated alignment pulse. As discussed in chapter 6, the alignment pulse is simply the uncompressed pulse coming from the regenerative amplifier of the femtosecond laser system. This pulse is necessarily very strongly chirped, to the extent that the time and frequency domains correspond nearly exactly. This means that by passing this pulse through a commerical long-pass filter (Thorlabs FELH0800), it can be effectively truncated in time - the pulse envelope is no longer a Gaussian, but shows a sharp cutoff at around 800 nm. The temporal profile of the truncated pulse is shown in black (with grey shading) on Fig. 10.4. The pulse 'turns on' slowly, so the molecules align adiabatically as the intensity of the alignment field grows, then the pulse is rapidly turned off - no longer adiabatic. This sharp cutoff has been shown to result in oscillations reminiscent of those seen for non-adiabatic alignment using short laser pulses [179].

The effect of using a truncated pulse to align molecules in HeDs is illustated in Fig. 10.4 (figure adapted from [169]). The grey shaded area (underneath the black line) shows the temporal profile of the truncated pulse. The red curve shows the measured degree of alignment of diiodobiphenyl (DIBP - structure shown in the top right), inside HeDs. The blue curve shows the yield of intact parent ions ($DIBP^+$). It is clear that the measured degree of alignment increases as the alignment field is turned on, as expected, but also that the molecules remain well aligned after the pulse is turned off, for a period of around 10 ps. Additionally, the blue curve shows that the yield of parent cations increases sharply

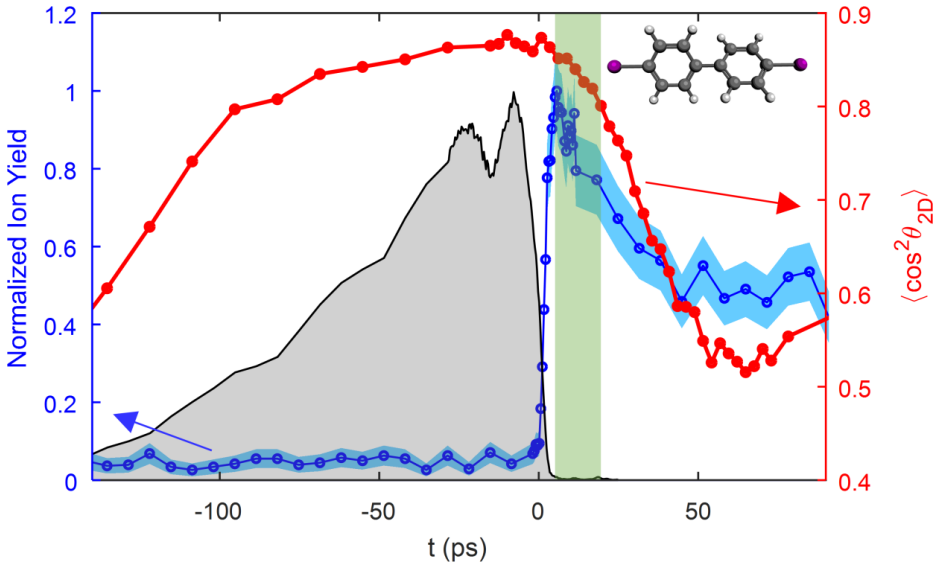

Figure 10.4: Time-dependent yield of intact parent ions from ionisation of diiodobiphenyl (DIBP - structure shown in top right) molecules in HeDs (blue). The DIBP molecules are 1D aligned using a truncated alignment pulse, the temporal profile of which is shown in black with grey shading. The red curve shows the time dependent degree of alignment. The green shaded area represents a region where there is still a reasonable degree of alignment and a large number of intact parent ions detected. Figure adapted from [169].

as the alignment pulse is truncated. The implication of this is that it is possible to perform experiments in a region (shown with a green shaded area), where the molecules are both well-aligned and there are many intact parent ions present.

400nm Probe

The final difference between the experiments described previously and this anthracene experiment was that the probe laser pulse was not centered at 800 nm, but was instead centered at 400 nm. This was done as prior work on tetracene and pentacene suggested that cleaner signals (less fragmentation) would be observed at 400 nm - perhaps at odds with what would be expected from the picture described in section 4.2.1. This will be further explored in subsection 10.3.4.

10.3.2 Potential Structures

The structures considered are the same structures shown in Fig. 10.2. Figure 10.5 shows each of these structures in the molecular frame (row (1)), and shows sketches of how they would align with an alignment pulse present linearly polarised along the X axis (row (2)); linearly polarised along the Z axis (row (3)); and circularly polarised in the XZ plane (row (4)).

As in previous sections, these structures will be compared with the experimental results, to try and narrow down the range of potential structures.

10.3.3 Experimental Results

Figure 10.6 (a1) shows an image of $Anth^+$ ions, recorded with a probe pulse polarised along the X axis, and no alignment pulse. The image shows a clear intense central spot (inside the annotated yellow circle), and some signal at larger radii ($v > 0.3\,\mathrm{km\,s^{-1}}$). The intense signal inside the annotated yellow circle is assigned as resulting from the ionisation of anthracene monomers, and the signal at larger radii is ascribed to resulting from the ionisation of $(Anth)_2$. This assignment is corroborated by the angular covariance map in panel (a2), which is calculated using all ion hits outside the annotated yellow circle in (a1). The covariance map shows a clear signal at $\theta_1 = \theta_2 + 180°$, which is consistent with a two-body break up. Additionally, this signal extends uniformly over the full 360° range, which is expected as the dimers are not aligned. The image (a1) also shows this, as the distribution of ions outside of the yellow circle is circularly symmetric. A small depletion at the top of the image is noticeable, and this arises from a weak area on the detector - this can be removed somewhat by increasing the voltages applied to the detector, but is still visible (as shown in (a1))[2]. This depletion is very slightly visible in the angular covariance map as a slight reduction in the covariance around (0°, 180°) - and the equivalent spot obtained by mirroring in the central diagonal. This image clearly demonstrates that we can form $(Anth)_2$, but does not allow the structure of the dimer to be determined directly.

Figure 10.6 (b1)-(d1) show analogous images to panel (a1), except now alignment pulses are also present. Each image will be analysed in turn below, but it is immediately obvious that there is no dramatic change to the structure of the ion images when the alignment pulse is included. This

[2]The cause of this was discovered in Sep 2018 to be a piece of fluff that had got onto the detector whilst the flight-tube was being removed.

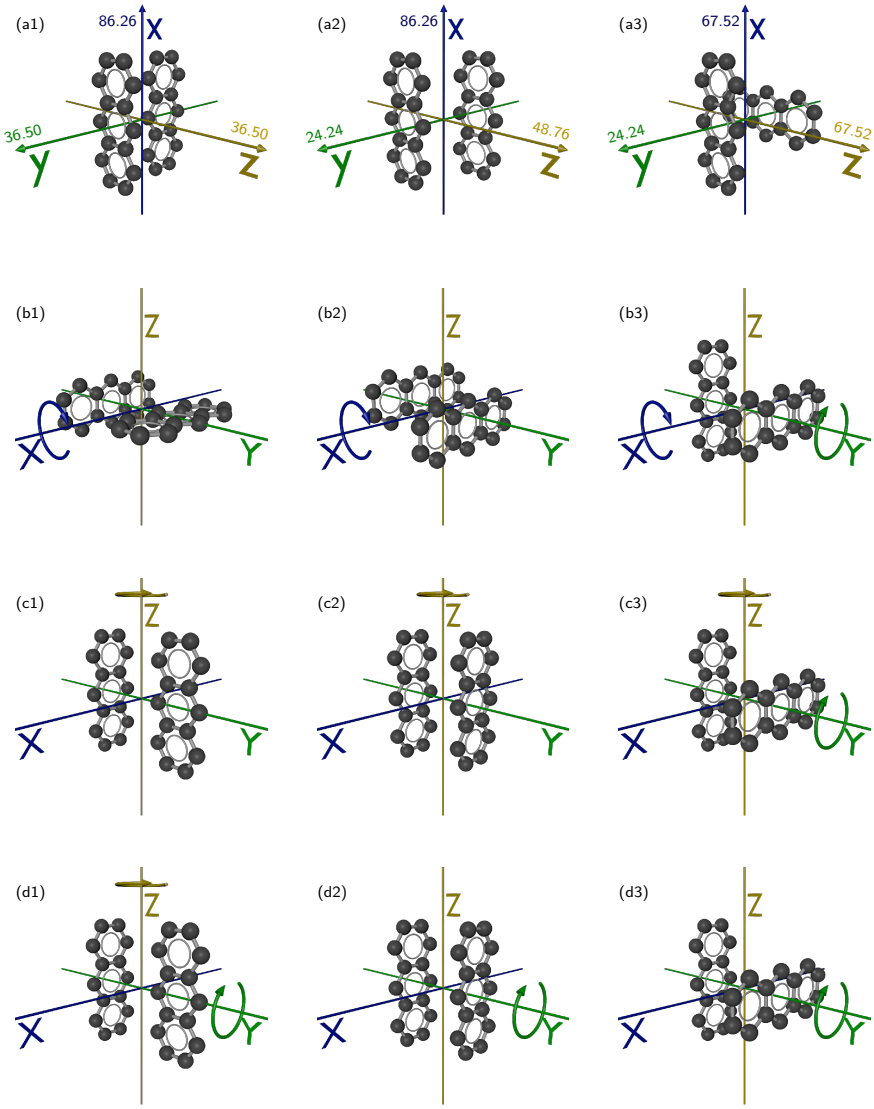

Figure 10.5: Potential structures of $(Anth)_2$ shown in both the molecular (row (1)) and space-fixed (rows (2)-(4)) frames. Each column (a)-(c) corresponds to a specific structure. Rows (2)-(4) show sketches of how each structure would align in the space-fixed frame, under an alignment field linearly polarised along X (2); linearly polarised along Z (3); and circularly polarised in the XZ plane (4). Curved arrows indicate axes around which rotation is possible.

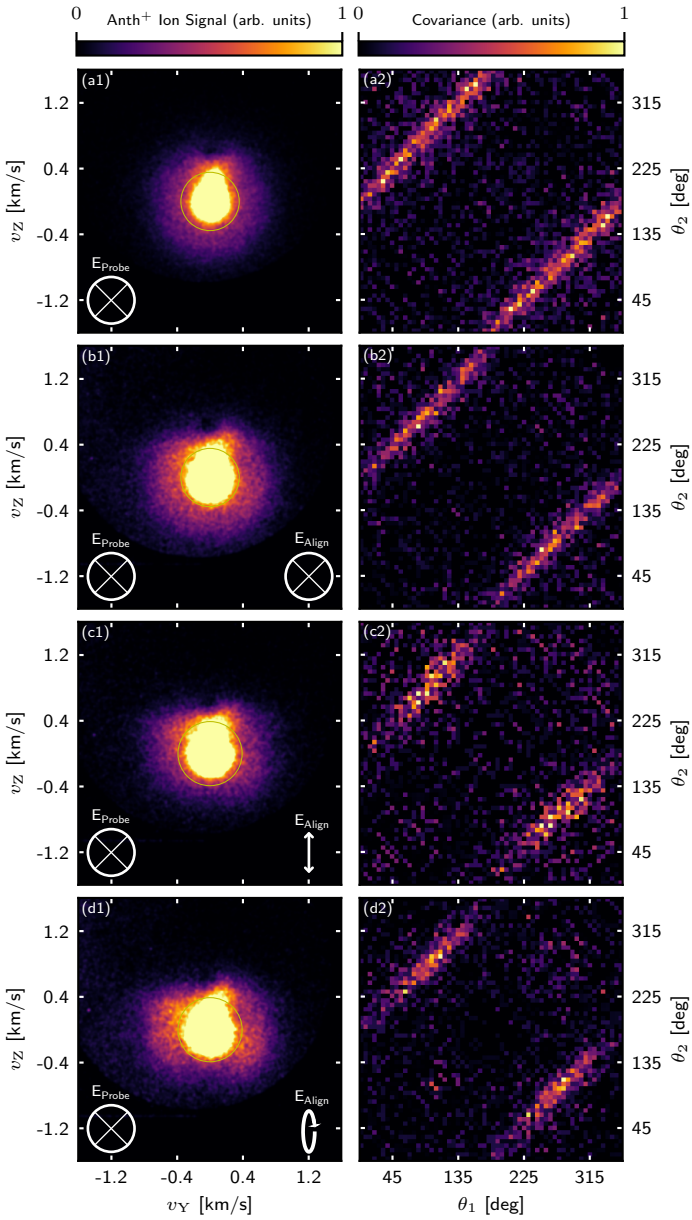

Figure 10.6: (a1)-(d1) $Anth^+$ ion images and (a2)-(d2) corresponding angular covariance maps. The polarisation state of the probe (alignment) pulse is shown in the lower left (right) corner of each ion image. All data was recorded at an oven current of 1.0 A. The area of low sensitivity on the detector is clearly visible directly above the annotated yellow circle.

is at odds with the equivalent images in chapter 9 and chapter 7 (Fig. 7.4 and Fig. 9.4), where generally[3] a stark difference in the structure of the ion images was observed with the introduction of an alignment pulse. This will be further discussed in subsection 10.3.4.

Figure 10.6 (b1) shows an image of $Anth^+$ ions, recorded with a probe and alignment laser pulse both polarised along X. It is not immediately clear if the circular symmetry present in image (a1) is still present. The ion image perhaps looks as if there is more signal along Y than along Z, but the corresponding angular covariance map in panel (b2) seems to show a uniform line at $\theta_1 = \theta_2 + 180°$. The line is perhaps slightly truncated, and shows a weaker signal at (0°, 180°) than at other angles - but this could also arise from the area of low sensitivity on the detector. However, all three of the potential structures shown in Fig. 10.5 would show this covariance map under an alignment field polarised along X, with the IMA free to rotate around the X axis, so none can be ruled out from this image.

Figure 10.6 (c1) shows an analogous image to (b1), but the alignment pulse is now linearly polarised along the Z axis. Here the ion image looks slightly more localised along Y, than in (a1) or (b1), and the corresponding angular covariance map (c2) shows much more localised islands than in (b2) or (a2). This implies that the IMA is now no longer able to freely rotate around X. However, this would be case for all the potential structures under this alignment field, so none of them can be ruled out based on this image and covariance map.

Finally, Fig. 10.6 (d1) shows an analogous image to (c1), but the alignment pulse is now circularly polarised in the XZ plane. The image looks very similar to image (c1), and the corresponding angular covariance map (d2) also looks very similar to (c2), showing two truncated islands centered at (90°, 270°) and (270°, 90°). This again implies that under this alignment field, the IMA is not able to be aligned along Z, as this would produce a covariance signal at (0°, 180°). This is the case for both the cross-shaped and offset-parallel structure, but the T-shaped structure would be expected to produce such a covariance signal under this alignment field. Based on this, we can tentatively conclude that the T-shaped anthracene dimer is not present in HeDs, but there are several unexplained points to discuss.

[3]Except when the alignment pulse was polarised along X, when the circular symmetry is generally maintained.

10.3.4 Discussion

Based on the current experimental findings, we can tentatively state that the T-shaped anthracene dimer is not observed in HeDs. However, we cannot distinguish between the other two potential structures (cross-shaped and offset-parallel) using this data. To further distinguish these, theoretical support would be required to see which of these structures would be more likely to form in a HeD. The initial attempts at finding such theoretical support have recently been undertaken in Femtolab.

It is clear that the above experiment was not a resounding success. However, an unexplained phenomenon has been revealed. Namely, why do the aligned ion images appear to show such a poor degree of alignment compared to those observed for CS_2 and OCS? The polarisability anisotropy of $(Anth)_2$ is very high ($\Delta\alpha \approx 50\,\text{Å}^3$), so the expected degree of alignment should be very high. One explanation could be very severe NAR, but the covariance maps do not show this. Another explanation is that parent ions from the most well aligned dimers are fragmented, and therefore not detected. The best aligned dimers will be present at the center of the focus of the alignment laser beam - this is also at the center of the probe laser beam, such that the best aligned molecules are probed. It is plausible that the intensity at the center of the probe beam is high enough to cause fragmentation of the molecules that are there, so the parent ions that are produced intact do not come from the best aligned dimers, even when using a truncated pulse. However, the probe power used was low enough that the amount of ion signal was on the edge of being unusably low. Further lowering of the probe intensity would require an increase in the number of doped droplets (and an increase in oven temperature). This was problematic for Anth as discussed previously.

This phenomenon of large molecules showing poor degrees of alignment has also been noticed in Femtolab for dimers of tetracene and pentacene. Further study is required to discover the exact cause of it, and these experiments are currently ongoing. Initially, tuning the wavelength of the probe pulse further into the IR may help reduce fragmentation, as this has been observed for anthracene (and other PAHs) previously [180], as well as for larger systems [138]. The rationale for this is similar to that presented in section 4.2 - longer wavelengths result in more tunnelling ionisation, which is a more 'gentle' ionisation process, resulting in fragmentation. This conclusion is supported by experimental evidence [138, 181]. However, a clear question that can be asked is then why the probe wavelength was chosen to be 400 nm and not 800 nm, if moving towards the IR results in less fragmentation?

The initial decision to use 400 nm pulses to probe with was based on prior experiences within Femtolab, where better signals were observed using 400 nm than 800 nm. As it became clear that the observed degree of alignment was poor, a switch to 800 nm was made, to see if moving to a longer wavelength resulted in a better degree of alignment being measured. Surprisingly, the measured degree of alignment when using a 400 nm probe was lower than when using an 800 nm probe ($\langle\cos^2\theta_{2D}\rangle = 0.46$ for 800 nm compared to $\langle\cos^2\theta_{2D}\rangle = 0.39$ for 400 nm). This is at odds with the expectation, so either the fragmentation is greater at 800 nm[4], or there is another explanation. One possibility is that when ionising with a linearly polarised 800 nm pulse there is a larger amount of recollisions, resulting in more fragmentation. If this was the case, it would be expected that this could be ameliorated by using a circularly polarised probe pulse. This was attempted and made no discernible difference.

A second possiblity is that by moving to shorter wavelengths, we are moving into some kind of quasi-resonant regime, where the strong-field picture no longer applies. In this specific case, however, this is unlikely to be the case - as the ionisation potential of anthracene is 7.44 eV, so more than two 400 nm photons would be required to ionise it. However, developing this idea further, moving to a fully-resonant probe may also help to reduce the fragmentation. If explosion of the parent molecules is not desired, then using a resonant probe to efficiently produce singly ionised parent molecules may help to reduce the observed effect. Furthermore, this method may help to increase signal levels as more of the desired parent ions are produced and reach the detector. The difficulty here would be generating laser pulses with the right wavelength to one- or two-photon ionise the molecules, as a laser pulse of wavelength 166 nm would be required to ionise anthracene with one photon. This difficulty notwithstanding, this may be a way to circumvent the current problem, and is currently being considered within Femtolab.

10.4 Photodimerisation of Anthracene

Section 10.2 discussed the possiblity of performing the photodimerisation of anthracene in HeDs. A schematic of this dimerisation was shown in Fig. 10.1. This dimerisation occurs via a photochemically allowed $[4\pi_s + 4\pi_s]$ cycloaddition. It has never been performed in the gas-phase before, but is a widely used technique in organic synthesis [175, 182, 183], where it is generally initiated in solution via irradiation with a UV source

[4]Comparison of the ToF spectra at the two wavelengths to determine the extent of the fragmentation was inconclusive.

centered at 350 nm (typically a high-pressure Hg lamp), or simply by letting the sample sit in a transparent container in sunlight for several hours. The first step in being able to perform this cycloaddition inside HeD is to ascertain whether or not the photoproduct, dianthracene (Dianth), is a good experimental observable. Having established this, the photodimerisation can be attempted.

10.4.1 Synthesis and Detection of Dianthracene

It is important to be able to detect a clear signature of Dianth in the HeDs, and especially one which will allow it to be easily differentiated from Anth. This is especially important, as we are unlikely to be able to photoexcite a large proportion of the molecules in the HeDs (typically around 10% would be excited), so not all will undergo photodimerisation. As such, there will be a large number of non-excited Anth molecules present, so the signal of Dianth must be visible against a large background signal from these non-excited molecules.

The most direct way to see if a signal from dianthracene is visible, is to put the Dianth photoproduct into the oven and dope it directly into the HeDs. It can then be subjected to the probing techniques available and the signal arising from it observed. Ideally, a clear signal of Dianth^+ would be visible in the ToF spectrum at a m/z ratio of 356 Da, as there was no signal visible in the ToF spectrum at this m/z ratio when running $(\text{Anth})_2$. Firstly, however, a sample of Dianth that can be run in the oven must be created.

Synthesis of Dianthracene

It is not possible to buy samples of Dianth commercially, such as through Sigma-Aldrich, or other chemical vendors. As a result, it must be synthesised if a pure sample is desired to be used for study. This synthesis is well documented [174] and simple to perform. A saturated solution of anthracene in benzene is produced in a sample vial, and this vial is left to stand in bright sunlight for a period of 24-48 h. The sunlight initiates the photodimerisation, and the resulting dianthracene is insoluble in benzene, forming a white precipitate which falls to the bottom of the sample vial. Figure 10.7 shows a saturated solution of anthracene in benzene before (a) and after (b) it has been stood in sunlight for 24 h, with a white precipitate being clearly visible.

Having produced this precipitate, it can be easily separated from the solution via vacuum filtration. The crystals are then dried on a rotary

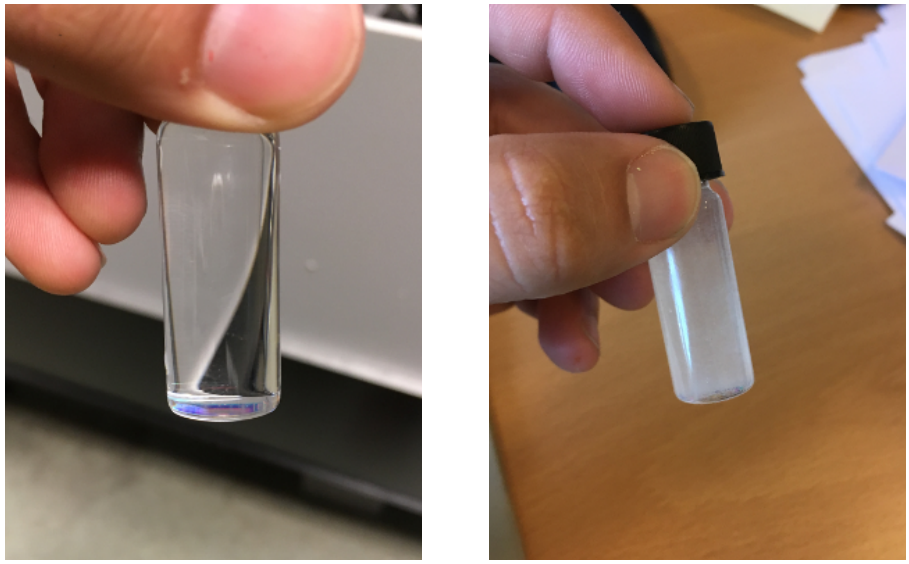

(a) **(b)**

Figure 10.7: (a) A saturated solution of anthracene in benzene, kept in the dark for 24 hours. (b) A saturated solution of anthracene in benzene, left in sunlight for 24 hours.

Sample	^{1}H-NMR (400 MHz, $CDCl_3$)Shifts
Anth	8.44 (s, 1 H), 8.01 (dd, 2 H), 7.47 (dd, 2 H)
Dianth	6.92 (dd, 1 H), 6.81 (dd, 1 H), 4.55 (s, 1 H)

Table 10.1: Table showing ^{1}H-NMR shifts

evaporator, and are then ready to be loaded into the oven and used. To ensure that this synthesis was successful, ^{1}H-NMR spectra were taken of both the anthracene starting material and the dianthracene photoproduct. The results of the ^{1}H-NMR are tabulated in Table 10.1.

The ^{1}H-NMR data shown in Table 10.1 shows that the synthesis has been successful. Considering the ^{1}H-NMR spectrum of the anthracene starting material, it is clear that all the protons have a high chemical shift, expected as they are bound to an aromatic system. The splittings of the three different environments are also entirely consistent with the structure of anthracene. Turning to the ^{1}H-NMR spectrum of the photoproduct, the most striking change is that one proton is no longer aromatic, which is expected for dianthracene. The splittings of each peak are also entirely consistent with what is expected for the dianthracene photoprod-

uct. Additionally, there was no signal consistent with anthracene in the dianthracene sample, showing that our synthesis and purification process was effective. Having shown that it was possible to synthesise and purify the dianthracene photoproduct, it was then run in the vacuum system.

Detection of Dianthracene

Initial attempts at detecting the signal from dianthracene consisted of placing it in the oven and looking to see any signal as the oven current was increased. The variables here were the current applied to the oven, and the wavelength of the ionising laser beam. It was expected that using longer (up to 2 µm) wavelengths to ionise would result in more intact parent ions being ionised, but a variety of wavelengths were attempted in the first instance.

Firstly, an appropriate oven current had to be found at which dianthracene could be observed. Having experienced many problems in finding an appropriate oven current for anthracene, the current was at first increased very conservatively. Eventually, it was found that a current of around 2.3 A gave the best conditions. Running at this oven current over a number of days resulted in the deposition of the dianthracene sample on the cold trap. Recording an ^{1}H-NMR of the deposited sample on the cold trap gave confirmation that it was indeed dianthracene that was deposited. This was important, as it is known that heating of the dianthracene can result in dissociation of it back into two anthracene molecules, so we do not reverse the photodimerisation by heating the anthracene to be doped into droplets.

Initial attempts were made to record a ToF spectrum and see a Dianth^{+} signal using wavelengths ranging from 266 nm to 2000 nm. This tunability was achieved by using the Ti:Sa output to pump a TOPAS Optical Parametric Amplifier (OPA). There was never any clear mass peak at an m/z of 356 Da present in any of the ToF spectra, but this experiment was hindered by time constraints. However, recording ion images using a 400 nm probe pulse, with a gate that would cover this m/z region did show some signal - this image is shown in Fig. 10.8, and the corresponding angular covariance map clearly shows no trace of a dianthracene dimer.

So it is clear that the Dianth^{+} ion is detectable, albeit at low levels. Time constraints prevented a thorough wavelength study, but it is expected that moving further towards the mid-IR would result in stronger signals (less fragmentation of the dianthracene cations).

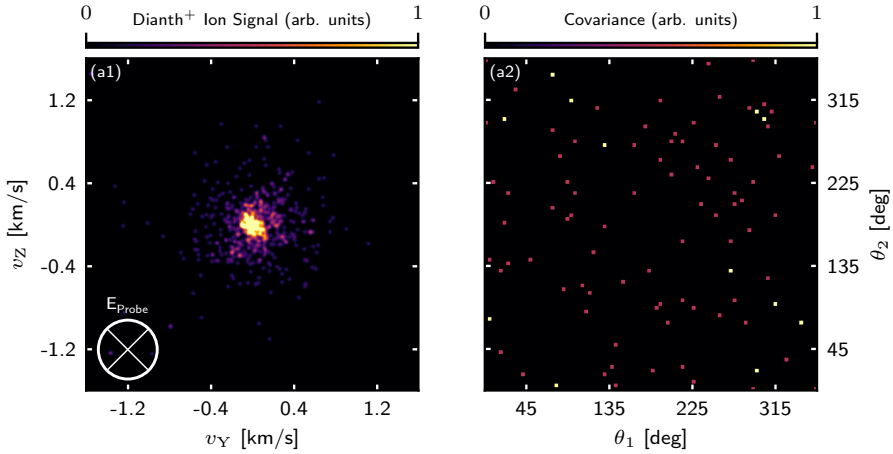

Figure 10.8: (a1) $Anth^+$ ion image with (a2) corresponding angular covariance map. The polarisation state of the probe laser is shown in the lower right corner of the ion image. This image was recorded at an oven current of 2.3 A.

10.4.2 Discussion and Outlook

Thus, we have seen that it is possible to synthesise Dianth, and to detect and image $Dianth^+$ ions. Unfortunately, time constraints prevented further progress with this project, which will be returned to after the completion of this PhD thesis. There is still much further work to do before we would be in a position to undertake the final experiment of performing the time-resolved photodimerisation inside HeDs. Firstly, a thorough study of the wavelength dependence of the $Dianth^+$ ion signal should be completed, together with an analogous study on the $Anth^+$ ion signal. This would ensure that the effect of the wavelength (especially with regards to parent ion fragmentation) is understood, and would ensure that the probe wavelength that gives the largest number of intact parent ions is used.

Secondly, before attempting to perform the photodimerisation in HeDs, it would be instructive to use the UV laser beam to perform the photodimerisation in a solution of anthracene in benzene. By using a NirUVis extension to a TOPAS OPA, the wavelength of of the UV beam can be easily tuned in the 240-400 nm range. Previous experiments have always used non-coherent UV light sources (UV lamps or sunlight), so the exact wavelength at which the photodimerisation occurs is not known. This can be ascertained by simply irradiating the anthracene solutions in the NirUVis beam and observing which wavelengths result in dimerisation.

Having done both of these prerequisite experiments, it would then be possible to attempt to perform the photodimerisation in HeDs. Initially, this would be attempted by irradiating the droplets with a UV pump pulse, and then probing them some few hundred ps later, and seeing if a substantial increase in the amount of $Dianth^+$ ions is observed. If this is successful, then the time-resolved photodimerisation would be attempted, with potentially very exciting results.

10.5 Summary

The first part of this chapter has applied the LIA/CEI technique to a much more complicated system than that which was attempted in previous chapters. It was shown that dimers of anthracene molecules could be made inside HeDs, and that $Anth^+$ ions from their explosion could be imaged. It did not prove possible, however, to unambiguously determine the structure of $(Anth)_2$ inside HeDs using this technique. Some problems were encountered which will be discussed in the following chapter.

The second part of this chapter documented the first steps towards performing the time-resolved photodimerisation of Anth into Dianth inside HeDs. It was shown that it was possible to synthesise Dianth and then to dope it into HeDs, and image intact $Dianth^+$ parent ions. Time constraints prevented further progress with this experiment, and the next steps will be discussed in the following chapter.

CHAPTER 11

Conclusion and Outlook

This thesis has presented experiments concerning the generation, manipulation, and characterisation of weakly-bound molecular complexes solvated in HeDs. This chapter summarises the conclusions from each of the experiments, and presents some potential avenues for further study. I believe that these preliminary experiments on complexes of molecules presage the dawn of a new era of experiments in Femtolab, subject to some considerations. Some ideas for further experiments are given here.

11.1 Complexes of Small Molecules

Chapters 7, 8, and 9 detailed experiments on dimers and trimers of the small triatomic molecules CS_2 and OCS. Small triatomics were chosen in the first instance as their relative simplicity made them ideal candidates for testing the capabilities of our experimental setup. The first experiment was a study of the CS_2 dimer, and was presented in chapter 7. This experiment showed that it was possible to form dimers of CS_2 inside HeDs, and also to control the complexation (to a limited extent) by controlling the partial pressure of CS_2 vapour in the doping cell. More pertinently, it showed that femtosecond-timescale CEI in conjunction with LIA allowed the structure of $(CS_2)_2$ to be unambiguously determined by analysis of the $CS_2{}^+$ ion recoil velocities. This was an important result, as it showed that detailed structural information could be obtained whilst preserving the femtosecond time resolution of the probe process.

Central to the study of $(CS_2)_2$ was the use of a circularly polarised alignment pulse to align the LPA of $(CS_2)_2$ to the propagation axis of

the alignment laser beam. Chapter 8 presented a study of the degree of alignment as a function of alignment intensity was undertaken and compared to simulation. Strictly, the alignment of $(CS_2)_2$ with a circularly polarised laser pulse is 3D alignment - alignment of the MPP of the dimer to the polarisation plane. However, in the limiting case of a circularly polarised pulse, this problem reduces to a 1D problem - the alignment of the LPA of the dimer to the propagation axis of the aligning laser beam. This was shown mathematically in chapter 4, and allows the degree of alignment to be simulated using a 1D alignment calculator. Excellent agreement was obtained between the experimental data and simulated data.

The final experiment concering small triatomic molecules was a study of the dimers and trimers of OCS. OCS was chosen as a candidate to compare to CS_2 as it is polar, so might be expected to form unusual structures inside HeDs. This study was presented in chapter 9 and showed that the structure of $(OCS)_2$ in the HeDs was the same as that observed in the gas phase, a slipped-parallel structure[1]. Extension of the study to $(OCS)_3$ showed that multiple structures of $(OCS)_3$ were annealed inside the HeDs. A barrel-shaped structure (also observed in the gas phase) was unambiguously observed, and a trace of a trigonal planar structure was also visible. Most unexpectedly, a linear-chain structure was observed that is not observed in the gas phase. This is in line with prior studies of polar molecules in HeDs, where it has been shown that polar molecules can form dipole-directed linear chain structures. Interestingly, our evidence suggests that for this to happen, a rearrangement of the parallel-shaped dimer must happen inside the droplet. There is some precedent for this, but more theoretical work may be able to provide a greater insight into these processes.

The aforementioned experiments showed that we have the experimental tools required to study these weakly-bound complexes. Further work on these systems would be possible, and a simple extension would be to study complexes of other small molecules, such as CO_2, N_2O or acetylene. A more complex example may be to study hetero-dimers, such as CS_2-CO_2. However, simply observing the structures of these systems inside HeDs is not the best use of our technique. The true utility of the LIA/CEI technique lies in the fact that it allows structural information to be obtained whilst retaining femtosecond time resolution. Typically, more detailed structural information can be obtained by using frequency-

[1] Although strictly it was not possible to ascertain whether the structure had the S atoms facing inwards or outwards.

resolved techniques, so there is little reason to continue to determine static structures using LIA/CEI[2]. With this in mind, a time-resolved experiment would be the most interesting next step, and one that is within the realms of possibility using the current experimental setup. The most obvious example based on the current work would be a study of the time-resolved torsion of $(CS_2)_2$, as it was shown in chapter 7 that it is possible to manipulate the dihedral angle using the alignment laser pulse. Using then a short 'kick' pulse to initiate this torsion, it should be possible to image the torsional oscillation in real time - with an expected period of 4 ps. Initial attempts were made at this experiment following the $(CS_2)_2$ dimer study, but were not successful.

11.2 Anthracene in Helium Droplets

Chapter 10 detailed initial attempts at a more ambitious experiment, the photodimerisation of anthracene molecules inside HeDs. This experiment consisted of two parts, the formation and imaging of $(Anth)_2$, followed by the attempted photodimerisation and creation of Dianth. Considering the imaging of $(Anth)_2$, it was clear that it is possible to make and detect $Anth^+$ that arises from $(Anth)_2$, but the structure of $(Anth)_2$ in HeDs could not be unambiguously determined. Turning to the photodimerisation, it was possible to perform the photodimerisation *ex vacuo* and then dope the Dianth photoproduct into HeDs. A clear ion signal from $Dianth^+$ was visible. Initial attempts at peforming the photodimerisation *in vacuo* were not successful, but were only very preliminary due to time constraints.

There are several parts of this experiment that would benefit from further study. First examining the reasons behind the failure of this experiment, it was immediately clear that the measured degree of alignment was substantially lower than what would be expected for a highly polarisable molecule like anthracene. The reasons for this are unclear, and could be related to a number of different phenomena. Firstly, the NAR experienced by the $Anth^+$ ions could be severe, despite their high mass. One can imagine an $Anth^+$ ion as acting as a large 'sail' that has to push through a much larger number of He atoms compared to an atomic ion like I^+, leading to a greater degree of NAR. However, this conclusion is not borne out by the angular covariance maps, which suggest that the NAR is not substantially greater than for any other heavy ion recoiling out of a HeD. I think a more likely cause of the observed behaviour is

[2]That said, spectroscopic interrogation of very large molecules can be challenging due to the large number of low frequency vibrational modes that can be populated.

fragmentation of the best aligned anthracene dimers. It has already been established that parent ions of such large molecules are easily fragmented by the presence of the alignment pulse, so it is plausible that ions arising from the best aligned dimers (in the center of the alignment laser focus - at the highest intensity) are also fragmented by the probe pulse, decreasing the observed degree of alignment. It was observed that moving from a probe laser centered at 400 nm to one centered at 800 nm decreased the observed degree of alignment[3], so a thorough wavelength study would be beneficial to ascertain the impact that the probe wavelength has on the fragmentation. Initial attempts at this were made, but were inconclusive and again hampered by time constraints.

Now considering the photodimerisation, this is potentially a very impactful experiment, if it could be performed in HeDs in a time-resolved manner. Having performed the experiment *ex vacuo* using sunlight, the next step would be to determine exactly which UV wavelength intitiates the photodimerisation - this is not clear from the literature as prior experiments have used non-coherent, broadband sources like UV lamps, or the sun. Having established this, and established which probe wavelength is most effective for producing a large number of intact parent ions, the stage would be set for attempting to perform the time-resolved photodimerisation. If this was successful, then many possibilties emerge, not least the potential to perform an analogous experiment on an anthracene derivative substituted with (for example) halogen atoms. It is then plausible that the nascent halide ions following Coulomb explosion would provide a useful 'structural marker' (see, for example [143]), allowing the shape of the dianthracene photoproduct, and progress of the cycloaddition, to be followed in real time.

11.3 Outlook

The preceding sections have given a summary of the experiments presented in this thesis, and have discussed some potential avenues for further study. If the aforementioned obstacles (fragmentation of parent ions, lower than expected degree of alignment) can be surmounted, then there are a great many experiments that can be attempted. Some of these were mentioned in the previous sections, but some more ambitious examples will be discussed here.

Making the 'molecular movie' has been alluded to throughout this

[3]This in itself is surprising as one would expect that longer wavelengths fragment the molecules less.

thesis, and is still a major ambition within Femtolab. Intramolecular dynamics of $(CS_2)_2$, or the intermolecular photodimerisation of Anth would have been (and still may be) ideal candidates for making such a movie. The difficulty with these kinds of experiments is that it is often challenging to find an appropriate molecular candidate. In all cases, to undertake time-resolved imaging requires that the molecular candidate is alignable into a useful geometry; and has a useful observable, or 'structural marker' that can be used to image the dynamics. In addition to this, it must be able to be run in the vacuum system, and (if bimolecular dynamics are desired) form a dimer which is readily manipulated and imaged. These are difficult criteria to fulfil, and the search for an ideal candidate is still ongoing.

A topic of recent interest within Femtolab is singlet fission. Singlet fission refers to the photochemical process where a singlet excited state is converted into two triplet excited states. For this to occur, the energy of the initial singlet state must be greater than twice the energy of the resultant triplet states. Acene dimers, such as those of anthracene, tetracene, and pentacene are therefore ideal candidates for singlet fission, as they tend to satisfy this requirement. Singlet fission is particularly industrially relevant as it has the potential to dramatically enhance the efficiency of organic solar cells, as each absorbed photon could then result in two excited molecules rather than one [171]. Typically these photophysical processes are studied in solution, or on model systems which are then compared with simulation. The chance to study the intrinsic photophysics of these systems in a very weakly perturbing medium HeDs would be a very interesting experiment.

The experiments in this thesis have all relied on ion imaging. An alternative technique, which has recently started to be revisited in Femtolab, is photoelectron imaging. Photoelectron imaging can provide detailed information about the energies of electronic states, far beyond what is possible with ion imaging. Previous studies of photoelectron imaging from molecules in HeDs in Femtolab [96], proved difficult to interpret, and were hampered by suboptimal experimental conditions. However, recent work in the group of Markus Koch has shown that time-resolved photoelectron spectroscopy on photoexcited indium atoms solvated in HeDs is possible [95]. This study followed the formation of a bubble inside the droplet in real time, and show that photoelectrons are a useful observable for studying time-resolved processes in droplets. This potentially opens the door to a wide range of exciting experiments. Discussions of potential systems are currently ongoing - promising ideas include the study of Super Atomic Molecular Orbital (SAMO) states of C_{60} [184]; studying

the alignment dynamics (and intermolecular vibrations) of C_{60} dimers; or attempting to find a model system in which to study the singlet fission processes mentioned previously. Not all of these potential experiments involve using complexes of molecules, but I am confident that our newfound understanding of complexes, combined with recent developments in photoelectron techniques, will produce some very exciting science in Femtolab in the years to come.

APPENDIX A

Calibration of the VMI Spectrometer

The exact position that an ion produced with a specific energy is mapped onto the detector at depends on the voltages applied to the ion optics in the spectrometer, and the kinetic energy of the ion. The speed v ($\mathrm{m\,s^{-1}}$) of an ion of mass m (Da) that is detected at a pixel of radius r (pixels) is given by Eq. A.1.

$$v = \sqrt{\left(\frac{ar^2}{m}\right)} \tag{A.1}$$

The constant a ($\mathrm{m^2\,Da\,s^{-2}\,pixels^{-2}}$) depends on the voltages applied to the ion optics in the spectrometer. This constant is calculated either by analysis of the kinetic energy release of a known species, or via above-threshold-ionisation (ATI) of Ar atoms. ATI is a process where an atom is ionised with more photons than is necessary to reach the continuum. The liberated electrons then gain additional kinetic energy based on the number of additional photons absorbed. A recorded electron image then shows a series of peaks corresponding to different electron energies, and the separation between two adjacent peaks corresponds to the photon energy of the ionising laser. If the photon energy of the laser is known, then this can be used to calibrate the spectrometer.

In either case, the calibration is performed at a series of different voltages applied to the extractor plate in the spectrometer, and the relation between energy and radius is established at the different voltages. This is a linear relationship, so the value of the constant a can be scaled

$V_{\mathrm{Ext.}}$ (V)	a ($\mathrm{m^2\,Da\,s^{-2}\,pixels^{-2}}$)
2000	9.238×10^3
3000	1.382×10^4
5000	2.303×10^4
6500	2.988×10^4

Table A.1: Values of the calibration constant a at different voltages applied to the extractor $V_{\mathrm{Ext.}}$.

up or down, depending on the voltage applied. The calibration constant a is related to the voltage applied to the extractor $V_{\mathrm{Ext.}}$ by Eq. A.2.

$$a = 4.589 V_{\mathrm{Ext.}} + 60.945 \tag{A.2}$$

In this way, the ion images can be used to provide absolute velocities for a specific ion species. Values of the a constant at different extraction voltages used in this thesis are tabulated in Table A.1.

APPENDIX B

Selected Studies of CS_2 Clusters in the Gas Phase

Studies of the CS_2 Dimer in HeDs were presented in chapter 7 and chapter 8. Just after these experiments were performed, attempts were made to perform the same experiments on isolated $(CS_2)_2$ by running CS_2 in the Even-Lavie valve (see subsection 6.1.4). Selected results from these attempts are documented here for reference, but the experimental conditions were not optimal (and experiments may eventually be repeated) - so analysis is limited.

B.1 Background

Performing experiments in both HeDs and the gas phase using identical laser parameters is a major reason behind the current design of the HeD machines in Femtolab. As both the HeD source and Even-Lavie (EL) valve (supersonic source) share a common target chamber, accurate comparisons between studies in HeDs and the same studies on isolated molecules can be quickly obtained. Here some aspects of the experimental setup relevant to the use of the EL valve are documented.

B.1.1 Experimental Setup

Unlike the HeD source, the EL valve is a pulsed valve running at a repetition rate of 200 Hz. The valve opening time is synchronised to the arrival time of the probe laser pulse, using the delay generator discussed

in chapter 6, and the camera shutter is also synchronised to the valve opening time. The exact valve opening time (and the temporal width of the gas pulse - how long the valve is open for) can be adjusted depending on the desired signal. Specifically, the gas density in the middle of the EL valve pulse is often very high, and there can be extensive clustering of the molecules in the beam at this point. Furthermore, ionisation of this part of the gas pulse can result signal levels that are high enough to damage the detector. Thus, adjustment of these parameters gives some degree of control over the clustering and signal level - although the coldest molecules are found at the center of the gas pulse, so moving to the edges may reduce clustering but also result in a warmer ensemble of molecules being probed.

The EL valve is then connected to a a backing line of He gas at 80 bar pressure, to act as a carrier gas. The molecular sample is either loaded into the body of the valve itself (for solids, or less volatile liquids), or can be run in an external reservoir (for volatile liquids), or can be run in an external pressurised gas bottle (gases). For CS_2, the molecular sample is placed in an external reservoir attached to the valve body. As CS_2 is very volatile, this still results in a dangerously high amount of CS_2 signal being registered on the detector. To alleviate this, the reservoir is placed in a bath of dry ice and acetone, to cool the CS_2 down to a temperature of around 195 K (−78 °C). This results in a high, but usable, CS_2^+ signal being detected.

However, there is some difficulty in regulating the vapour pressure of CS_2 in this way. The temperature in the acetone bath must be held constant to ensure a consistent signal, and if the temperature is too high, then the signal level can rapidly increase. Not only is this dangerous for the detector, but also the molecules (and especially any clusters) in the beam are observed to be less efficiently cooled when the temperature in the acetone bath is too high. Difficulty in regulating this meant that it was challenging to obtain consistent conditions from day to day. Thus far, one day has given better data quality than any other day, but we are still unsure as to whether we had truly optimal conditions here. As a result of this, the data here are relegated to this appendix rather than forming part of the thesis proper.

All data shown here comes from the day where the alignment of the CS_2 and CS_2 clusters was observed to be the best, as on other days the measured degree of alignment was markedly lower - which we ascribe to the warmer temperature of the molecules and clusters in the beam. This data should be repeated before truly meaningful analysis is undertaken.

These problems notwithstanding, there are some potentially interesting phenomena shown by these data, which are deserving of further study.

B.2 Results and Discussion

Here some selected experimental images are shown. All images shown were recorded on the day where the conditions seemed to be the best. Unfortunately, there were no images taken using a circularly polarised alignment field on this day, which would have been an interesting comparison to the results shown in chapter 8. However, there were data taken using linearly polarised alignment fields. Furthermore, these images by definition show no NAR due to scattering off He atoms, so illustrate the effect that the NAR has on the ion images presented in the preceding chapters.

With regards to the extent of the clustering, it will be shown that signals arising from Coulomb explosion of CS_2, $(CS_2)_2$, and $(CS_2)_3$ are present in the EL valve pulse. The structures of these clusters are initially assumed to be the same as the literature structures known from gas-phase IR spectroscopy - namely a cross-shaped CS_2 dimer, and a barrel-shaped CS_2 trimer (analogous to $(OCS)_3$) [46]. As a consequence of this, Fig. B.1 shows these two structures in the molecular frame (column (1)), and shows their expected alignment in the laboratory frame under an alignment field linearly polarised along X (column (2)), and Z (column (3)).

B.2.1 CS_2^+ Images

Figure B.2 (a1) shows a CS_2^+ ion image, recorded using a probe laser pulse polarised along the X axis, with no alignment pulse present. The image is dominated by an intense central signal, ascribed to the ionisation of CS_2 monomers in line with previous chapters. Additionally, a narrow ring of signal is visible between the two annotated yellow circles - this is ascribed as arising from the double ionisation of $(CS_2)_2$, which fragments into two correlated CS_2^+ ions. The angular covariance map (a3), calculated between the two annotated yellow circles, also shows a signal at $\theta_1 = \theta_2 + 180°$- consistent with the Coulomb explosion of $(CS_2)_2$. Furthermore, the angular covariance map (a4), calculated outside the outermost annotated yellow circle, shows a signature at $\theta_1 = \theta_2 + 120°$and at $\theta_1 = \theta_2 + 240°$- consistent with the explosion of the CS_2 trimer, $(CS_2)_3$ (in an analogous way to that presented in chapter 9). $(CS_2)_3$ is known to be barrel-shaped in the gas phase (see Fig. B.1 (b1)), and this data is completely consistent with this structure. Ion signal outside the outermost yellow circle is not visible when the ion image is plotted using a

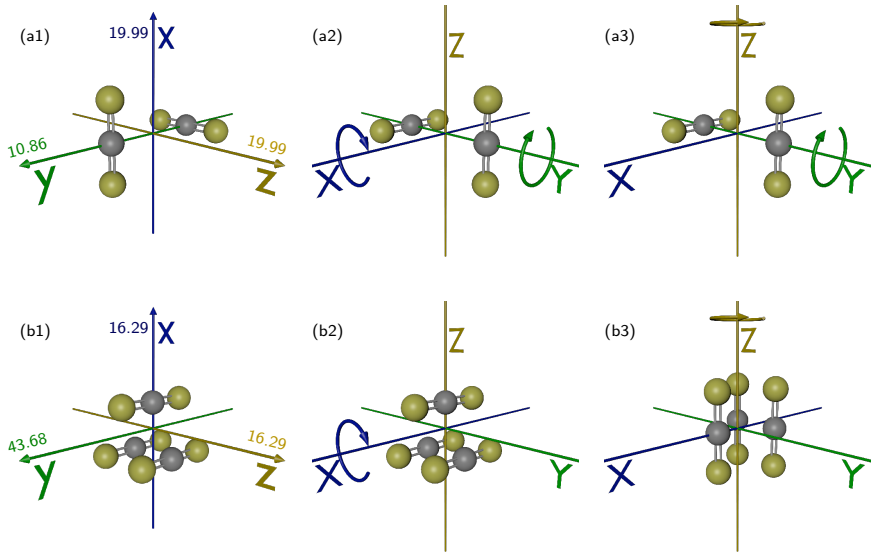

Figure B.1: (a1)-(b1) Sketches of the gas-phase structure of $(CS_2)_2$ (a1) and $(CS_2)_3$ (b1), as determined by IR spectroscopy. Polarisability elements are annotated on each relevant axis, in units of $Å^3$. (a2)-(b2) [(a3)-(b3)] Sketches of how each structure would align in the laboratory frame, when exposed to an alignment laser field linearly polarised along the X [Z] axis. Curved arrows indicate axes around which rotation is possible.

linear colourmap, is clear when the ion image is plotted with a logarithmic colourmap - this is shown in panel (a2) and is indicative of the much lower numbers of trimers present. Finally, in all images and covariance maps the observed signal extends uniformly around the full 360° range, which is expected in the absence of an alignment pulse.

Row (b) of Fig. B.2 shows an analogous set of images and covariances map to those in row (a), but now an alignment and probe pulse are both present, both polarised along the X axis. All images and covariance maps look similar to those in row (a), but there is a depletion of the ion signal in the region between the intense central spot and the sharp ring assigned to explosion of $(CS_2)_2$. This depletion arises due to the presence of the alignment pulse, which will restrict rotation around Z, as shown in Fig. B.1 (a2). This restricted rotation prevents the IMA from rotating into the detector (YZ) plane, resulting in the observed depletion. This depletion is also present between the dimer ring and trimer ring (see

Fig. B.1 (b2)), but is harder to see in the logarithmic ion image (b2). However, it is visible in the angular covariance map (b4), as the covariance signals appear much sharper than in the angular covariance map (a4). All this is consistent with restricted rotation around Z, which is entirely consistent with the alignment of the predicted structures of $(CS_2)_2$ and $(CS_2)_3$ with an alignment field linearly polarised along X.

Finally, row (c) of Fig. B.2 shows analogous images and covariance maps to row (b), but now the alignment pulse is linearly polarised along Z. Firstly, it is immediately clear that the ion signal is now localised along the Y axis, as was observed for $(CS_2)_2$ in chapter 7. This is consistent with the alignment field restricting rotation around X (see Fig. B.1 (a3)). The angular covariance map (c3) no longer shows a line but a short island centered at (90°, 270°) (and the equivalent from mirroring in the central diagonal). The trimer angular covariance map (c4) also shows this more localised signal, but it is broader and weaker - this arises as now there is free rotation around Z but restricted rotation around X, resulting in the truncation of the covariance signal. A final point to note is that the length of the island in the covariance map (c3) is longer than was observed for the equivalent map in HeDs (Fig. 7.4 (b2)). This is indicative of weaker alignment, and will be discussed further later.

To summarise, $CS_2{}^+$ images of CS_2 in the EL valve show clear signatures of CS_2, $(CS_2)_2$, and $(CS_2)_3$. The images and covariance maps are entirely consistent with a cross-shaped structure for $(CS_2)_2$ and a barrel-shaped structure for $(CS_2)_3$- which is consistent with their expected structure from IR spectroscopy [46].

B.2.2 S^+ Images

Figure B.3 (a1) shows an S^+ ion image, recorded using only a probe laser pulse polarised along the X axis, and no alignment pulse. In this case, the intense central signal comes from singly charged molecular oxygen ($O_2{}^+$), which overlaps the S^+ mass channel at $m/z = 32$ Da. Apart from this signal, there is an intense ring of signal between the two annotated yellow circles. This arises from Coulomb explosion of CS_2, creating two correlated S^+ ions. The angular covariance map calculated between the two annotated circles, (a3), shows a weak signal at $\theta_1 = \theta_2 + 180°$, together with a large, unstructured, background signal. Despite the background masking the signal somewhat, the line at $\theta_1 = \theta_2 + 180°$ is consistent with Coulomb explosion of CS_2 into two correlated S^+ ions. The signal in both (a1) and (a3) extends uniformly over the full 360° range, which is expected due to the absence of an alignment pulse. The angular covariance

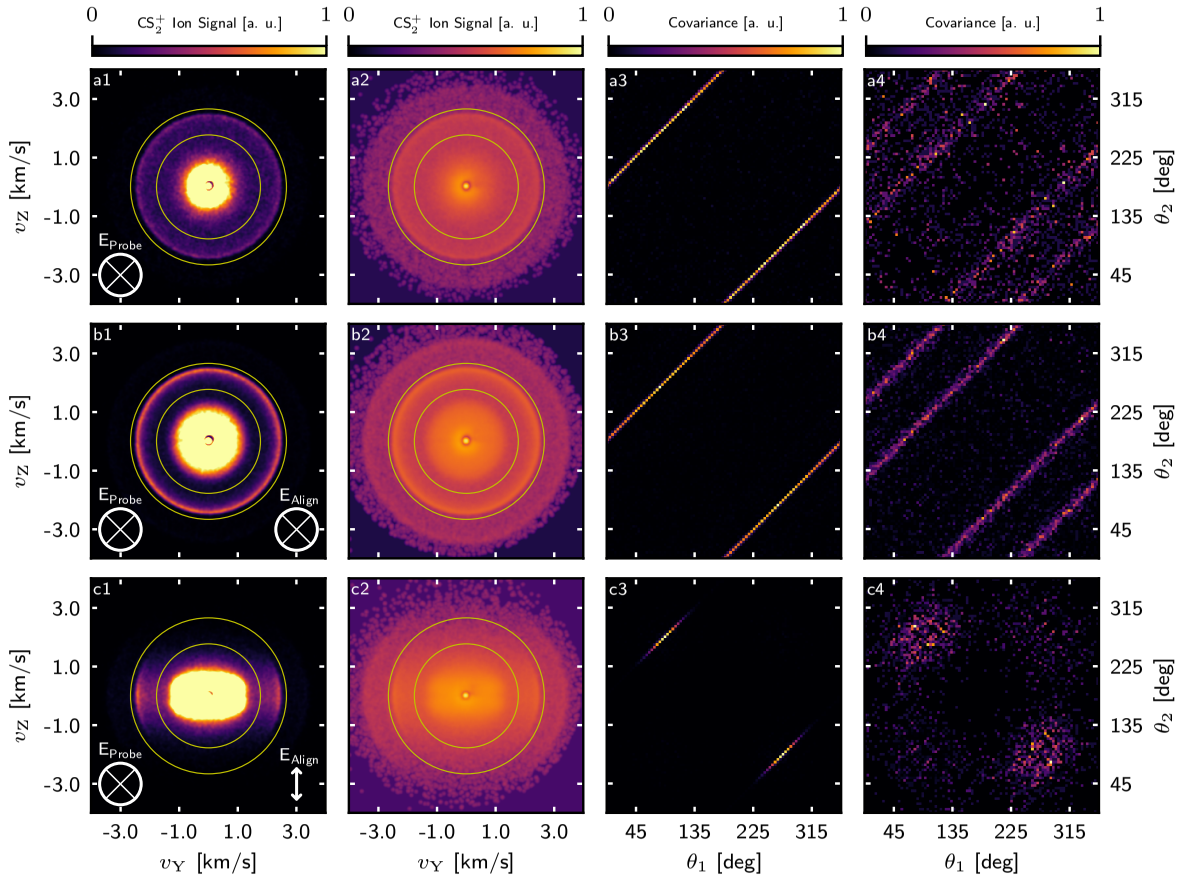

Figure B.2: (a1)-(c1) CS_2^+ ion images, presented on a linear scale. (a2)-(c2) the same ion images as in (a1)-(c1), shown on a logarithmic scale. (a3)-(c3) corresponding angular covariance maps, recorded using ions between the two annotated yellow circles on (a1)-(c1). (a4)-(c4) angular covariance maps, calculated using ions outside the outermost yellow circle. The polarisation state of the probe (alignment) laser is shown in the lower left (right) corner of the images in column (1).

map shown in panel (a4) is calculated using ions outside of the outermost annotated yellow circle, and shows three distinct signals. The central signal corresponds to $\theta_1 = \theta_2 + 180°$, from Coulomb explosion of CS_2. The two signals either side of this are rather broad, and it is difficult to conclusively assign the angles they correspond to, however we tentatively assign them as corresponding to $\theta_1 = \theta_2 + 90°$ and $\theta_1 = \theta_2 + 270°$ - consistent with Coulomb explosion of the cross-shaped $(CS_2)_2$. Finally, panel (a2) shows the same image as (a1), but with a more saturated colourmap - so that signal outside of the outermost annotated yellow circle can be seen.

Row (b) of Fig. B.3 shows analogous images to those in row (a), but now an alignment pulse linearly polarised along Z is present. The ion image (b1) is now localised along Z, which is consistent with alignment of CS_2 to the polarisation direction of the laser field. The angular covariance map (b3) now shows a sharply truncated island centered at (0°, 180°) (and the equivalent obtained by mirroring in the central diagonal), indicative of alignment. The angular covariance map calculated using ions outside of the outermost yellow circle (a4), resembles the equivalent map observed in HeDs (Fig. 7.5 (c2)). Accordingly, it is consistent with explosion of the cross-shaped dimer, but there are some differences that will be more fully explored in subsection B.2.3. Finally, panel (b2) shows the same image as (b1), but with a more saturated colourmap so that the ion signal outside the outermost circle can be seen.

B.2.3 Comparison between Gas Phase and Helium Droplets

Some comparisons will now be drawn between the gas-phase data presented here and the HeD data presented in previous chapters. As stated, the experimental conditions were not optimal when recording the gas-phase data, so detailed analysis will be limited. Despite this, there are perhaps some interesting questions that can be raised, and provide some food for thought.

Firstly, the most obvious difference between the images shown here and those in preceding chapters is the degree of NAR. The gas-phase images show no NAR caused by scattering from He atoms, and as a result the ion images appear much more structured with sharper features. This is clearly an advantage when interpreting such images, and such gas-phase images can be used to extract accurate internuclear distances from the well-defined ion energies following Coulomb explosion. This cannot be achieved in HeDs, due to the NAR caused by scattering off He atoms, and is one area in which there is a distinct advantage to studying molecular

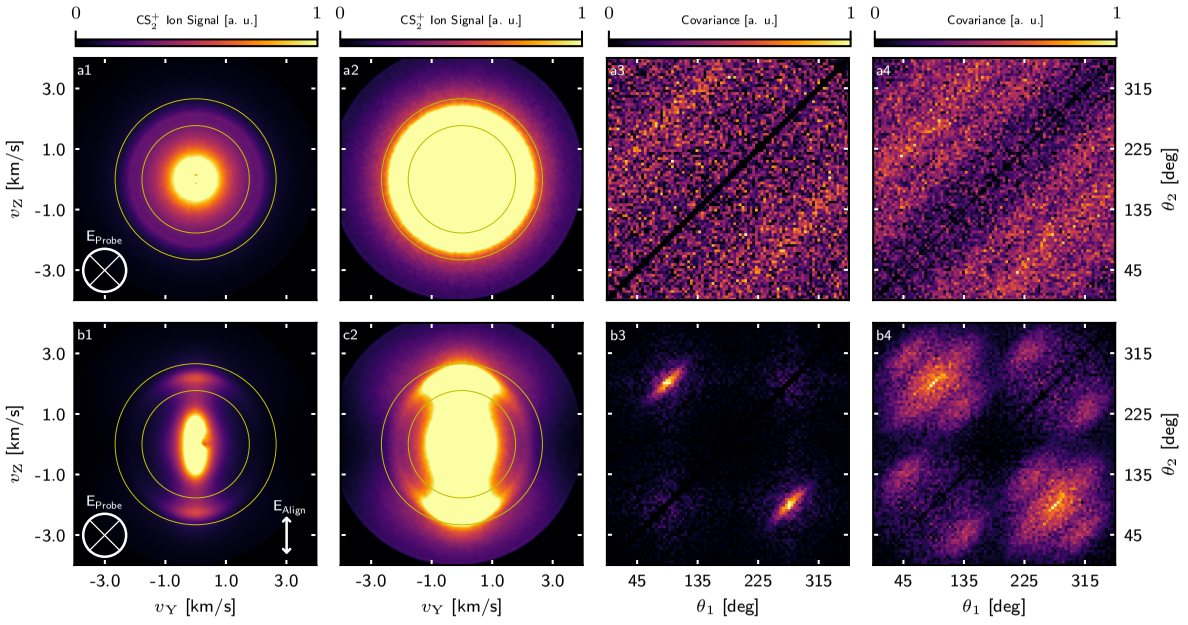

Figure B.3: (a1)-(b1) S^+ ion images, presented on a linear scale. (a2)-(b2) the same ion images as in (a1)-(b1), but with a more saturated colourmap to show outer regions of the image more clearly. (a3)-(b3) corresponding angular covariance maps, recorded using ions between the two annotated yellow circles on (a1)-(c1). (a4)-(b4) angular covariance maps, calculated using ions outside the outermost annotated yellow circle. The polarisation state of the probe (alignment) laser is shown in the lower left (right) corner of the images in column (1).

dynamics in the gas-phase.

A potentially more interesting difference lies in the observed alignment behaviour of the molecules and (especially) the clusters. Comparing, for example, Fig. 7.4 (b1) and (b2) and Fig. B.2 (c1) and (c3), it is clear that while the NAR is worse in the HeDs, the degree of alignment is weaker in the gas phase than in the HeDs. Specifically, the degree of alignment of the $(CS_2)_2$ in the gas phase, measured from the image Fig. B.2 (c1) is $\langle \cos^2 \theta_{2D} \rangle = 0.87$. In contrast, the degree of alignment of $(CS_2)_2$ in HeDs, measured via deconvolution from the covariance map Fig. 7.4 (b2), is $\langle \cos^2 \theta_{2D} \rangle = 0.96$. So the observed degree of alignment is much weaker in the gas phase than in HeDs. The most obvious reason for this would be that the molecules in the gas phase are warmer than those in HeDs. This is known to be the case [162], but the difference between the measured degrees of alignment here is much higher than was observed in previous experiments. Rough calculations of the expected degree of alignment here suggest that the temperature of the $(CS_2)_2$ in the gas-phase is warmer than 4 K, which is much higher than would normally be expected in an EL valve pulse (generally around 1 K). However, whether this is due to intrinsically inefficient cooling of the clusters in the supersonic expansion, or was due to sub-optimal experimental conditions resulting in inefficient cooling is unclear. Data taken on subsequent days using CS_2 in the EL valve showed even worse degrees of alignment, so it is plausible that some experimental problem prevents efficient cooling of the clusters. This would benefit from further study, and is one potential avenue for further exploration.

Bibliography

[1] E. D. Potter, J. L. Herek, S. Pedersen, Q. Liu, and A. H. Zewail, "Femtosecond laser control of a chemical reaction," *Nature*, vol. 355, pp. 66–68, Jan. 1992.

[2] D. Zhong and A. H. Zewail, "Femtosecond Real-Time Probing of Reactions. 23. Studies of Temporal, Velocity, Angular, and State Dynamics from Transition States to Final Products by Femtosecond-Resolved Mass Spectrometry," *J. Phys. Chem. A*, vol. 102, pp. 4031–4058, June 1998.

[3] A. H. Zewail, "Femtochemistry: Atomic-Scale Dynamics of the Chemical Bond," *J. Phys. Chem. A*, vol. 104, pp. 5660–5694, June 2000.

[4] J. G. Stark and H. G. Wallace, *Chemistry Data Book*. Hodder Education, 2 ed., 1982.

[5] C. Grenier, "Thermal conductivity of liquid helium. i.," *Phys. Rev.*, vol. 83, p. 598, Apr. 1951.

[6] L. Landau, "Theory of the superfluidity of helium II," *Phys. Rev.*, vol. 60, pp. 356–358, Aug. 1941.

[7] D. R. Allum, P. V. E. McClintock, and A. Phillips, "The Breakdown of Superfluidity in Liquid ^{4}He: An Experimental Test of Landau's Theory," *Philos. Trans. R. Soc. (London) Ser. A*, vol. 284, pp. 179 –224, Jan. 1977.

[8] M. E. Jacox, "The spectroscopy of molecular reaction intermediates trapped in the solid rare gases," *Chem. Soc. Rev.*, vol. 31, pp. 108–115, Jan. 2002.

[9] J. P. Toennies and A. F. Vilesov, "Superfluid Helium Droplets: A Uniquely Cold Nanomatrix for Molecules and Molecular Complexes," *Angew. Chem. Int. Ed.*, vol. 43, p. 2622, May 2004.

[10] F. Stienkemeier and K. K. Lehmann, "Spectroscopy and dynamics in helium nanodroplets," *J. Phys. B: At. Mol. Opt. Phys.*, vol. 39, no. 8, p. R127, 2006.

[11] J. P. Toennies and A. F. Vilesov, "Spectroscopy of Atoms and Molecules in Liquid Helium," *Annual Review of Physical Chemistry*, vol. 49, no. 1, pp. 1–41, 1998.

[12] D. M. Brink and S. Stringari, "Density of states and evaporation rate of helium clusters," *Z. Phys. D: At. Mol. Clusters*, vol. 15, no. 3, pp. 257–263, 1990.

[13] F. Ancilotto, P. B. Lerner, and M. W. Cole, "Physics of solvation," *J. Low. T. Phys.*, vol. 101, p. 1123, Sept. 1995.

[14] N. B. Brauer, S. Smolarek, E. Loginov, D. Mateo, A. Hernando, M. Pi, M. Barranco, W. J. Buma, and M. Drabbels, "Critical Landau Velocity in Helium Nanodroplets," *Phys. Rev. Lett.*, vol. 111, p. 153002, Oct. 2013.

[15] M. Rosenblit and J. Jortner, "Dynamics of the Formation of an Electron Bubble in Liquid Helium," *Phys. Rev. Lett.*, vol. 75, pp. 4079–4082, Nov. 1995.

[16] S. Grebenev, J. P. Toennies, and A. F. Vilesov, "Superfluidity Within a Small Helium-4 Cluster: The Microscopic Andronikashvili Experiment," *Science*, vol. 279, pp. 2083 –2086, Mar. 1998.

[17] E. L. Andronikashvili, "A direct observation of two kinds of motion in helium ii," *J. Phys. USSR.*, vol. 10, p. 201, 1946.

[18] P. Hobza and K. Dethlefs-Müller, *Non-covalent Interactions, Theory and Experiment.* RSC Publishing, 2010.

[19] K. Dethlefs-Müller and P. Hobza, "Noncovalent interactions: A challenge for experiment and theory," *Chem. Rev.*, vol. 100, pp. 142–167, Dec. 1999.

[20] J. N. Israelachvili, *Intermolecular and Surface Forces.* Academic Press Ltd, 1991.

[21] J. Voigtsberger, S. Zeller, J. Becht, N. Neumann, F. Sturm, H. K. Kim, M. Waitz, F. Trinter, M. Kunitski, A. Kalinin, J. Wu, W. Schöllkopf, D. Bressanini, A. Czasch, K. Williams, J. B. amd Ullmann-Pfleger, L. P. H. Schmidt, M. S. Schöffler, R. E. Grisenti, T. Jahnke,

and R. Dörner, "Imaging the structure of the trimer systems $^4He_3$ and $^3He^4He_2$," *Nat. Commun.*, vol. 6765, Dec. 2014.

[22] BBC, "Bbc bitesize: Intermolecular forces of attraction."

[23] C. LibreTexts, "Chemistry libretexts: Van der waals interactions."

[24] M. D. Wheeler, D. T. Anderson, and M. I. Lester, "Probing reactive potential energy surfaces by vibrational activation of H_2-OH entrance channel complexes," *Int. Rev. Phys. Chem.*, vol. 19, p. 501, Oct. 2000.

[25] W. T. Yip and D. H. Levy, "Excimer/Exciplex Formation in van der Waals Dimers of Aromatic Molecules," *J. Phys. Chem.*, vol. 100, p. 11539, Jan. 1996.

[26] A. Zehnacker and M. A. Suhm, "Chirality recognition between neutral molecules in the gas phase," *Angew. Chem. Int. Ed.*, vol. 47, pp. 6970–6992, 2008.

[27] M. Becucci and S. Melandri, "High-Resolution Spectroscopic Studies of Complexes Formed by Medium-Size Organic Molecules," *Chem. Rev.*, vol. 116, p. 5014, May 2016.

[28] E. R. Johnson, S. Keinan, P. Mori-Sanchez, J. Contreras-Garcia, A. J. Cohen, and Y. Weitao, "Revealing noncovalent interactions," *J. Am. Chem. Soc.*, vol. 132, pp. 6498–6506, Feb. 2010.

[29] M. Broyer, R. Antoine, I. Compagnon, D. Rayane, and P. Dugourd, "From clusters to biomolecules: electric dipole, structure and dynamics," *Phys. Scr.*, vol. 76, pp. C135–C139, Oct. 2007.

[30] J. E. Ladbury, "Just add water! the effect of water on the specificity of protein-ligand binding sites and its potential application to drug design," *Chemistry & Biology*, vol. 3, pp. 973–980, Dec. 1996.

[31] I. D. Kuntz, "Structure-based strategies for drug design and discovery," *Science*, vol. 257, pp. 1078–1082, Aug. 1992.

[32] Z. Simon, "Specific interactions, intermolecular forces, steric requirements, and molecular size," *Angew. Chem. Int. Ed.*, vol. 13, pp. 719–727, Nov. 1974.

[33] E. C. H. Sykes, P. Han, S. A. Kandel, K. F. Kelly, G. S. McCarty, and P. S. Weiss, "Substrate-mediated interactions and intermolecular forces between molecules adsorbed on surfaces," *Acc. Chem. Res.*, vol. 36, pp. 945–953, Dec. 2003.

[34] M. Lafrance, C. N. Rowley, T. K. Woo, and K. Fagnou, "Catalytic intermolecular direct arylation of perfluorobenzenes," *J. Am. Chem. Soc.*, vol. 128, pp. 8754–8756, June 2006.

[35] H. Fenniri, B.-L. Deng, A. E. Ribbe, K. Hallenga, J. Jacob, and P. Thiyagarajan, "Entropically driven self-assembly of multichannel rosette nanotubes," *Proc. Natl. Acad. Sci. USA*, vol. 99, pp. 6487–6492, Apr. 2002.

[36] G. V. Gibbs, T. D. Crawford, A. F. Wallace, D. F. Cox, R. M. Parrish, E. G. Hohenstein, and C. D. Sherrill, "Role of long-range intermolecular forces in the formation of inorganic nanoparticle clusters," *J. Phys. Chem. A*, vol. 115, pp. 12933–12940, Sept. 2011.

[37] E. R. Bernstein, "Dynamics and photochemistry of neutral van der waals clusters," *Annu. Rev. Phys. Chem*, vol. 46, pp. 192–222, Aug. 1995.

[38] M. R. Topp, "Dynamics and structure of aromatic molecular van der waals complexes," *Int. Rev. Phys. Chem.*, vol. 12, pp. 149–204, Aug. 2008.

[39] A. A. Vigasin, "Structure and molecular spectroscopy of gas-phase complexes," *Zhurnal Strukturnoi Khimii*, vol. 28, pp. 120–147, Feb. 1986.

[40] V. G. Stavros and J. R. R. Verlet, "Gas-phase femtosecond particle spectroscopy: A bottom-up approach to nucleotide dynamics," *Annu. Rev. Phys. Chem.*, vol. 67, pp. 212–232, Mar. 2016.

[41] Z. Bacic and R. E. Miller, "Molecular clusters: Structure and dynamics of weakly bound systems," *J. Phys. Chem.*, vol. 100, pp. 12945–12959, Apr. 1996.

[42] B. L. Blaney and G. F. Ewing, "Van der waals molecules," *Annu. Rev. Phys. Chem.*, vol. 27, pp. 553–586, 1976.

[43] K. R. Leopold, G. T. Fraser, S. E. Novick, and W. Klemperer, "Current themes in microwave and infrared spectroscopy of weakly bound complexes," *Chem. Rev.*, vol. 94, pp. 1807–1827, Jan. 1994.

[44] A. Dell'Erba, S. Melandri, A. Millemaggi, W. Caminati, and P. G. Favero, "Rotational spectra and dynamics of the van der waals adducts of neon and argon with 1,1-difluoroethylene," *J. Chem. Phys.*, vol. 112, p. 2204, Jan. 2000.

[45] C. Kang, T. M. Korter, and D. W. Pratt, "Experimental measurement of the induced dipole moment of an isolated molecule in its ground and electronically excited states: Indole and indole-H_2O," *J. Chem. Phys.*, vol. 122, p. 174301, Feb. 2005.

[46] N. Moazzen-Ahmadi and A. R. W. McKellar, "Spectroscopy of dimers, trimers and larger clusters of linear molecules," *Int. Rev. Phys. Chem.*, vol. 32, p. 611, Dec. 2013.

[47] J. George, A. R. W. McKellar, and N. Moazzen-Ahmadi, "Infrared spectra of He-, Ne-, and Ar-C_6D_6," *Chem. Phys. Lett.*, pp. 121–124, 2014.

[48] A. M. Morrison, T. Liang, and G. E. Douberly, "Automation of an "aculight" continuous-wave optical parametric oscillator," *Rev. Sci. Inst.*, vol. 84, p. 013102, Jan. 2013.

[49] R. E. Miller and L. Pedersen, "The infrared spectrum and the structure of the nitrous oxide trimer," *J. Chem. Phys.*, vol. 108, p. 436, 1998.

[50] Y. Matsumoto, Y. Ohshima, and M. Takami, "Mode-specific infrared photodissociation of nitric oxide dimers: High-resolution infrared spectroscopy of $(^14NO)_2$ and $(^15NO)_2$," *J. Chem. Phys.*, vol. 92, p. 937, Sept. 1990.

[51] K. W. Jucks, Z. S. Huang, D. Dayton, and R. E. Miller, "The structure of the carbon dioxide dimer from near infrared spectroscopy," *J. Chem. Phys.*, vol. 86, p. 4341, Jan. 1987.

[52] M. Rezaei, J. Norooz Oliaee, N. Moazzen-Ahmadi, and A. R. W. McKellar, "Spectroscopic observation and structure of CS_2 dimer," *J. Chem. Phys.*, vol. 134, p. 144306, Apr. 2011.

[53] M. Rezaei, J. N. Oliaee, N. Moazzen-Ahmadi, and A. R. W. McKellar, "Infrared spectrum of the CS2 trimer: observation of a structure with D3 symmetry," *Phys. Chem. Chem. Phys.*, vol. 13, pp. 12635–12639, June 2011.

[54] R. S. Walters, T. D. Jaeger, and M. A. Duncan, "Infrared spectroscopy of $Ni^+(C_2H_2)_n$ complexes: Evidence for intracluster cyclization reactions," *J. Phys. Chem. A*, vol. 106, pp. 10482–10487, Oct. 2002.

[55] J. Wu, M. Kunitski, L. P. H. Schmidt, T. Jahnke, and R. Dörner, "Structures of N_2-Ar, O_2-Ar, and O_2-Xe dimers studied by Coulomb explosion imaging," *J. Chem. Phys.*, vol. 137, p. 104308, Sept. 2012.

[56] C. Wu, C. Wu, D. Song, H. Su, X. Xie, M. Li, Y. Deng, Y. Liu, and Q. Gong, "Communication: Determining the structure of the N_2-Ar van der Waals complex with laser-based channel-selected Coulomb explosion," *J. Chem. Phys.*, vol. 140, p. 141101, Apr. 2014.

[57] L. Christensen, J. H. Nielsen, C. B. Brandt, C. B. Madsen, L. B. Madsen, C. S. Slater, A. Lauer, M. Brouard, M. P. Johansson, B. Shepperson, and H. Stapelfeldt, "Dynamic Stark Control of Torsional Motion by a Pair of Laser Pulses," *Phys. Rev. Lett.*, vol. 113, p. 073005, Aug. 2014.

[58] J. Li, B. E. Bursten, B. Liang, and L. Andrews, "Noble gas-actinide compounds: Complexation of the cuo molecule by ar, kr, and xe atoms in noble gas matrices," *Science*, vol. 295, pp. 2242–2245, Mar. 2002.

[59] M. Pettersson, J. Lundell, and M. Rasanen, "Neutral rare-gas containing charge-transfer molecules in solid matrices. i. hxecl, hxebr, hxei, and hkrcl in kr and xe," *J. Chem. Phys.*, vol. 102, p. 6423, Jan. 1995.

[60] A. Lignell, L. Khriachtchev, M. Pettersson, and M. Rasanen, "Interaction of rare-gas-containing molecules with nitrogen: Matrix-isolated and ab initio study of harf-n2, hkrf-n2 and hkrcl-n2 complexes," *J. Chem. Phys.*, vol. 118, p. 11120, Mar. 2003.

[61] A. M. Sadoon, G. Sarma, E. M. Cunningham, J. Tandy, M. W. D. Hanson-Heine, N. A. Besley, S. Yang, and A. M. Ellis, "Infrared spectoscopy of $NaCl(CH_3OH)_n$ complexes in helium nanodroplets," *J. Phys. Chem. A*, vol. 121, pp. 8085–8093, Sept. 2016.

[62] K. Nauta and R. E. Miller, "Infrared spectroscopy and structures of Ar_n–HF in liquid helium nanodroplets," *J. Chem. Phys.*, vol. 115, pp. 10138–10145, Nov. 2001.

[63] E. Latimer, D. Spence, C. Feng, A. Boatwright, A. M. Ellis, and S. Yang, "Preparation of Ultrathin Nanowires Using Superfluid Helium Droplets," *Nano Lett.*, vol. 14, pp. 2902–2906, May 2014.

[64] K. Nauta and R. E. Miller, "Nonequilibrium Self-Assembly of Long Chains of Polar Molecules in Superfluid Helium," *Science*, vol. 283, p. 1895, Mar. 1999.

[65] A. Metzelthin, E. Sanchez-Garcia, O. Birer, G. Schwaab, W. Thiel, W. Sander, and M. Havenith, "Acetylene-furan trimer formation at 0.37k as a model for ultracold aggregation of non- and weakly polar molecules," *Chem. Phys. Chem.*, vol. 12, May 2011.

[66] G. E. Douberly and R. E. Miller, "The isomers of HF-HCN formed in helium nanodroplets: Infrared spectroscopy and ab initio calculations," *J. Chem. Phys.*, vol. 122, p. 024396, Jan. 2005.

[67] J. A. Davies, M. W. D. Hanson-Heine, N. A. Besley, A. Shirley, J. Trowers, S. Yang, and A. M. Ellis, "Dimers of acetic acid in helium nanodroplets," *In Prep.*, 2018.

[68] K. Nauta and R. E. Miller, "Formation of Cyclic Water Hexamer in Liquid Helium: The," *Science*, vol. 287, pp. 293–295, Jan. 2000.

[69] M. Wewer and F. Stienkemeier, "Laser-induced fluorescence spectroscopy of 3,4,9,10-perylenetetracarboxylic-dianhydride in helium nanodroplets.," *J. Chem. Phys.*, vol. 120, p. 1239, Oct. 2003.

[70] M. Hartmann, A. Lindinger, J. P. Toennies, and V. A. F., "Laser-induced fluorescence spectroscopy of van der waals complexes of tetracene-Ar_N (n≤5) and pentacene-ar within ultracold liquid he droplets," *Chem. Phys.*, vol. 239, pp. 139–149, Jan. 1998.

[71] N. Portner, A. F. Vilesov, and M. Havenith, "The formation of heterogeneous van der waals complexes in helium droplets," *Chem. Phys. Lett.*, vol. 343, pp. 281–288, Aug. 2001.

[72] S. Yang and A. M. Ellis, "Helium droplets: a chemistry perspective," *Chem. Soc. Rev.*, vol. 42, p. 472, Dec. 2012.

[73] M. Y. Choi, G. E. Douberly, T. M. Falconer, W. K. Lewis, C. M. Lindsay, J. M. Merritt, P. L. Stiles, and R. E. Miller, "Infrared spectroscopy of helium nanodroplets: novel methods for physics and chemistry," *Int. Rev. Phys. Chem.*, vol. 25, no. 1, p. 15, 2006.

[74] I. Reinhard, C. Callegari, A. Conjusteau, K. K. Lehmann, and G. Scoles, "Single and double resonance microwave spectroscopy in superfluid he clusters," *Phys. Rev. Lett.*, vol. 82, p. 5036, Feb. 1999.

[75] B. Shepperson, J. Tandy, A. Boatwright, C. Feng, D. Spence, A. Shirley, S. Yang, and A. M. Ellis, "Electronic spectroscopy of toluene in helium nanodroplets: Evidence for a long-lived excited state," *J. Phys. Chem. A*, vol. 117, pp. 13591–13595, Sept. 2013.

[76] C. Callegari, K. K. Lehmann, R. Schmied, and G. Scoles, "Helium nanodroplet isolation rovibrational spectroscopy: Methods and recent results," *J. Chem. Phys.*, vol. 115, p. 10090, Nov. 2001.

[77] C. Callegari and W. E. Ernst, "Helium droplets as nanocryostats for molecular spectroscopy - from the vacuum ultraviolet to the microwave regime," *Handbook of High-resolution spectroscopy*, Sept. 2011.

[78] S. Krasnokutski, G. Rouille, and F. Huisken, "Electronic spectroscopy of anthracene molecules trapped in helium nanodroplets," *Chem. Phys. Lett.*, vol. 406, pp. 386–392, May 2005.

[79] D. T. Moore, L. Oudejans, and R. E. Miller, "Pendular state spectroscopy of an asymmetric top: Parallel and perpendicular bands of acetylene-HF," *J. Chem. Phys.*, vol. 110, p. 197, Sept. 1999.

[80] M. Y. Choi and R. E. Miller, "Four tautomers of isolated guanine from infrared laser spectroscopy in helium nanodroplets," *J. Am. Chem. Soc.*, vol. 128, pp. 7320–7328, May 2006.

[81] P. L. Raston, E. I. Obi, and G. E. Douberly, "Infrared spectroscopy of the entrance channel complex formed between the hydroxyl radical and methane in helium nanodroplets," *J. Phys. Chem. A*, vol. 121, pp. 7597–7602, Sept. 2017.

[82] S. Rudic, J. M. Merritt, and R. E. Miller, "Study of the ch3-h20 radical complex stabilized in helium nanodroplets," *Phys. Chem. Chem. Phys.*, vol. 11, pp. 5345–5352, Oct. 2008.

[83] J. M. Merritt, J. Kupper, and R. E. Miller, "Entrance channel x-hf (x = cl, br, and i) complexes studied by high-resolution infrared laser spectroscopy in helium nanodroplets," *Phys. Chem. Chem. Phys.*, vol. 7, pp. 67–78, Jan. 2005.

[84] P. L. Stiles, D. T. Moore, and R. E. Miller, "Infrared spectroscopy of the isomers of magnesium-hcn formed in helium nanodroplets. comparisons with ab initio calculations," *J. Chem. Phys.*, vol. 118, p. 7873, Jan. 2003.

[85] J. M. Merritt, G. E. Douberly, P. L. Stiles, and R. E. Miller, "Infrared spectroscopy of prereactive aluminum-, gallium-, and indium-hcn entrance channel complexes solvated in helium nanodroplets," *J. Phys. Chem. A*, vol. 111, pp. 12304–12316, 2007.

[86] M. Mautner, "The ionic hydrogen bond," *Chem. Rev.*, vol. 105, pp. 213–284, Jan. 2005.

[87] A. Braun and M. Drabbels, "Photodissociation of alkyl iodides in helium nanodroplets. I. Kinetic energy transfer," *J. Chem. Phys.*, vol. 127, p. 114303, Sept. 2007.

[88] A. Braun and M. Drabbels, "Photodissociation of alkyl iodides in helium nanodroplets. II. Solvation dynamics," *J. Chem. Phys.*, vol. 127, p. 114304, Sept. 2007.

[89] A. Braun and M. Drabbels, "Photodissociation of alkyl iodides in helium nanodroplets. III. Recombination," *J. Chem. Phys.*, vol. 127, pp. 114305–114305–6, Sept. 2007.

[90] F. Stienkemeier, J. Higgins, W. E. Ernst, and G. Scoles, "Laser Spectroscopy of Alkali-Doped Helium Clusters," *Phys. Rev. Lett.*, vol. 74, pp. 3592–3595, May 1995.

[91] J. Tiggesbaumker and F. Stienkemeier, "Formation and properties of metal clusters isolated in helium droplets," *Phys. Chem. Chem. Phys.*, vol. 9, pp. 4748–4770, May 2007.

[92] M. Mudrich, P. Heister, T. Hippler, C. Giese, O. Dulieu, and F. Stienkemeier, "Spectroscopy of triplet states of Rb_2 by femtosecond pump-probe photoionization of doped helium nanodroplets," *Phys. Rev. A*, vol. 80, p. 042512, Oct. 2009.

[93] J. von Vangerow, A. Sieg, F. Stienkemeier, M. Mudrich, A. Leal, D. Mateo, A. Hernando, M. Barranco, and M. Pi, "Desorption dynamics of heavy alkali metal atoms (rb, cs) off the surface of helium nanodroplets," *J. Phys. Chem. A*, vol. 118, pp. 6604–6614, 2014.

[94] F. Stienkemeier, F. Meier, A. Hagele, H. O. Lutz, E. Schreiber, C. P. Schulz, and I. V. Hertel, "Coherence and relaxation in potassium-doped helium droplets studied by femtosecond pump-probe spectroscopy," *Phys. Rev. Lett.*, vol. 83, p. 2320, Sept. 1999.

[95] B. Thaler, S. Ranftl, P. Heim, S. Cesnik, L. Treiber, R. Meyer, A. W. Hauser, W. E. Ernst, and M. Koch, "Femtosecond photoexcitation dynamics inside a quantum solvent," *ArXiv e-prints*, Apr. 2018.

[96] L. Christiansen, *Laser Induced Alignment of Molecules Embedded in Helium Droplets: Exploration and Potential Applications*. PhD thesis, Aarhus University, July 2015.

[97] O. Kornilov, C. C. Wang, O. Bünermann, A. T. Healy, M. Leonard, C. Peng, S. R. Leone, D. M. Neumark, and O. Gessner, "Ultrafast

Dynamics in Helium Nanodroplets Probed by Femtosecond Time-Resolved EUV Photoelectron Imaging," *J. Phys. Chem. A*, vol. 114, pp. 1437–1445, Jan. 2010.

[98] O. Kornilov, O. Bunermann, D. J. Haxton, S. R. Leone, D. M. Neumark, and O. Gessner, "Femtosecond photoelectron imaging of transient electronic states and rydberg atom emission from electornically excited he droplets," *J. Phys. Chem. A*, vol. 115, pp. 7891–7900, June 2011.

[99] O. Bunermann, O. Kornilov, S. R. Leone, D. M. Neumark, and O. Gessner, "Femtosecond extreme ultraviolet ion imaging of ultrafast dynamics in electronically excited helium nanodroplets," *IEEE Journal of Selected Topics in Quantum Electronics*, vol. 18, Jan. 2012.

[100] M. P. Ziemkiewicz, D. M. Neumark, and O. Gessner, "Ultrafast electronic dynamics in helium nanodroplets," *Int. Rev. Phys. Chem.*, vol. 34, pp. 239–267, July 2015.

[101] O. Bunermann, O. Kornilov, D. J. Haxton, S. R. Leone, D. M. Neumark, and O. Gessner, "Ultrafast probing of ejection dynamics of rydberg atoms and molecular fragments from electronically excited helium nanodroplets," *J. Phys. Chem.*, vol. 137, p. 214302, Nov. 2012.

[102] D. Rupp, N. Monserud, B. Langbehn, M. Sauppe, J. Zimmermann, Y. Ovcharenko, T. Moller, F. Frassetto, L. Poletto, A. Trabattoni, F. Calegari, M. Nisoli, K. Sander, C. Peltz, M. J. Vrakking, T. Fennel, and A. Rouzee, "Coherent diffractive imaging of single helium nanodroplets with a high harmonic generation source," *Nat. Comm.*, vol. 8, p. 493, Sept. 2017.

[103] M. Brouard, S. D. S. Gordon, A. Hackett Boyle, C. G. Heid, B. Nichols, V. Walpole, F. J. Aoiz, and S. Stolte, "Integral steric asymmetry in the inelastic scattering of NO($X^2\Lambda$)," *J. Chem. Phys.*, vol. 146, p. 014302, Jan. 2017.

[104] F. J. Aoiz, M. Brouard, S. D. S. Gordon, B. Nichols, S. Stolte, and W. V., "A new perspective: imaging the stereochemistry of molecular collisions," *Phys. Chem. Chem. Phys.*, vol. 17, pp. 30210–30228, Aug. 2015.

[105] C. Z. Bisgaard, O. J. Clarkin, G. Wu, A. M. D. Lee, O. Gessner, C. C. Hayden, and A. Stolow, "Time-Resolved Molecular Frame Dynamics of Fixed-in-Space CS2 Molecules," *Science*, vol. 323, pp. 1464–1468, Mar. 2009.

[106] J. Maurer, *Tomographic reconstruction of 3-dimensional photoelectron momentum distributions using aligned molecules.* PhD thesis, Aarhus University, 2012.

[107] N. Kajumba, R. Torres, J. G. Underwood, J. S. Robinson, S. Baker, J. W. G. Tisch, R. d. Nalda, W. A. Bryan, R. Velotta, C. Altucci, I. Procino, I. C. E. Turcu, and J. P. Marangos, "Measurement of electronic structure from high harmonic generation in non-adiabatically aligned polyatomic molecules," *New J. Phys.*, vol. 10, no. 2, p. 025008, 2008.

[108] R. Velotta, N. Hay, M. B. Mason, M. Castillejo, and J. P. Marangos, "High-order harmonic generation in aligned molecules," *Phys. Rev. Lett.*, vol. 87, p. 183901, Oct. 2001.

[109] T. Kanai, S. Minemoto, and H. Sakai, "Quantum interference during high-order harmonic generation from aligned molecules," *Nature*, vol. 435, pp. 470–474, May 2005.

[110] R. Torres, N. Kajumba, J. G. Underwood, J. S. Robinson, S. Baker, J. W. G. Tisch, R. de Nalda, W. A. Bryan, R. Velotta, C. Altucci, I. C. E. Turcu, and J. P. Marangos, "Probing Orbital Structure of Polyatomic Molecules by High-Order Harmonic Generation," *Phys. Rev. Lett.*, vol. 98, p. 203007, May 2007.

[111] C. S. Slater, S. Blake, M. Brouard, A. Lauer, C. Vallance, J. J. John, R. Turchetta, A. Nomerotski, L. Christensen, J. H. Nielsen, M. P. Johansson, and H. Stapelfeldt, "Covariance imaging experiments using a pixel-imaging mass-spectrometry camera," *Phys. Rev. A*, vol. 89, p. 011401, Jan. 2014.

[112] C. S. Slater, S. Blake, M. Brouard, A. Lauer, C. Vallance, C. S. Bohun, L. Christensen, J. H. Nielsen, M. P. Johansson, and H. Stapelfeldt, "Coulomb-explosion imaging using a pixel-imaging mass-spectrometry camera," *Phys. Rev. A*, vol. 91, p. 053424, May 2015.

[113] A. v. Veltheim, B. Borchers, G. Steinmeyer, and H. Rottke, "Imaging the impulsive alignment of noble-gas dimers via Coulomb explosion," *Phys. Rev. A*, vol. 89, p. 023432, Feb. 2014.

[114] S. Ishihara, H. Wakemoto, K. Nakazima, and M. Yoshihiro, "The effect of rubbed polymer films on the liquid crystal alignment," *Liquid Crystals*, vol. 4, pp. 669–675, Sept. 2006.

[115] M. F. Toney, T. P. Russell, J. A. Logan, H. Kikuchi, J. M. Sands, and S. K. Kumar, "Near-surface alignment of polymers in rubbed films," *Nature*, vol. 374, pp. 709–711, Apr. 1995.

[116] F. Filsinger, J. Küpper, G. Meijer, L. Holmegaard, J. H. Nielsen, I. Nevo, J. L. Hansen, and H. Stapelfeldt, "Quantum-state selection, alignment, and orientation of large molecules using static electric and laser fields," *J. Chem. Phys.*, vol. 131, no. 6, pp. 064309–13, 2009.

[117] D. H. Parker and R. B. Bernstein, "Oriented Molecule Beams Via the Electrostatic Hexapole: Preparation, Characterization, and Reactive Scattering," *Annu. Rev. Phys. Chem.*, vol. 40, p. 561, 1989.

[118] H. J. Loesch and A. Remscheid, "Brute force in molecular reaction dynamics: A novel technique for measuring steric effects," *J. Chem. Phys.*, vol. 93, pp. 4779–4790, Oct. 1990.

[119] D. Pentlehner, J. H. Nielsen, L. Christiansen, A. Slenczka, and H. Stapelfeldt, "Laser-induced adiabatic alignment of molecules dissolved in helium nanodroplets," *Phys. Rev. A*, vol. 87, p. 063401, June 2013.

[120] M. Z. Hoque, M. Lapert, E. Hertz, F. Billard, D. Sugny, B. Lavorel, and O. Faucher, "Observation of laser-induced field-free permanent planar alignment of molecules," *Phys. Rev. A*, vol. 84, p. 013409, July 2011.

[121] S. Luo, R. Zhu, L. He, W. Hu, X. Li, P. Ma, C. Wang, F. Liu, W. G. Roeterdink, S. Stolte, and D. Ding, "Nonadiabatic laser-induced orientation and alignment of rotational-state-selected $\{\mathrm{CH}\}_{3}\mathrm{Br}$ molecules," *Phys. Rev. A*, vol. 91, p. 053408, May 2015.

[122] M. D. Poulsen, E. Péronne, H. Stapelfeldt, C. Z. Bisgaard, S. S. Viftrup, E. Hamilton, and T. Seideman, "Nonadiabatic alignment of asymmetric top molecules: Rotational revivals," *J. Chem. Phys.*, vol. 121, pp. 783–791, July 2004.

[123] H. Stapelfeldt, "Laser Aligned Molecules: Applications in Physics and Chemistry," *Phys. Scripta.*, vol. 2004, no. T110, p. 132, 2004.

[124] J. Wu, A. Vredenborg, B. Ulrich, L. P. H. Schmidt, M. Meckel, S. Voss, H. Sann, H. Kim, T. Jahnke, and R. Dörner, "Nonadiabatic alignment of van der Waals–force-bound argon dimers by femtosecond laser pulses," *Phys. Rev. A*, vol. 83, p. 061403, June 2011.

[125] T. Seideman and E. Hamilton, "Nonadiabatic alignment by intense pulses. concepts, theory, and directions.," *Adv. Atm. Mol. Opt. Phys.*, vol. 52, pp. 289–329, Apr. 2006.

[126] H. Stapelfeldt and T. Seideman, "Colloquium: Aligning molecules with strong laser pulses," *Rev. Mod. Phys.*, vol. 75, p. 543, Apr. 2003.

[127] B. Friedrich and D. Herschbach, "Alignment and trapping of molecules in intense laser fields," *Phys. Rev. Lett.*, vol. 74, pp. 4623–4626, June 1995.

[128] B. Friedrich and D. Herschbach, "Polarization of Molecules Induced by Intense Nonresonant Laser Fields," *J. Phys. Chem.*, vol. 99, pp. 15686–15693, Oct. 1995.

[129] P. W. Atkins and R. S. Friedman, *Molecular Quantum Mechanics*. Oxford University Press, 4th ed., Dec. 2004.

[130] R. N. Zare, *Angular Momentum: Understanding Spatial Aspects in Chemistry and Physics*. WileyBlackwell, Aug. 1988.

[131] J. J. Larsen, K. Hald, N. Bjerre, H. Stapelfeldt, and T. Seideman, "Three Dimensional Alignment of Molecules Using Elliptically Polarized Laser Fields," *Phys. Rev. Lett.*, vol. 85, no. 12, p. 2470, 2000.

[132] Z. Vager, R. Naaman, and E. P. Kanter, "Coulomb Explosion Imaging of Small Molecules," *Science*, vol. 244, pp. 426–431, Apr. 1989.

[133] G. Both, E. P. Kanter, Z. Vager, B. J. Zabransky, and D. Zajfman, "Ultrathin foils for coulomb-explosion experiments," *Rev. Sci. Inst.*, vol. 58, p. 424, Nov. 1987.

[134] J. H. D. Eland, R. Singh, J. D. Pickering, C. S. Slater, A. Hult Roos, J. Andersson, S. Zagorodskikh, R. J. Squibb, M. Brouard, and R. Feifel, "Dissociation of multiply charged ICN by coulomb explosion," *J. Chem. Phys.*, vol. 145, p. 074303, Aug. 2016.

[135] J. L. Hansen, J. H. Nielsen, C. B. Madsen, A. T. Lindhardt, M. P. Johansson, T. Skrydstrup, L. B. Madsen, and H. Stapelfeldt, "Control and femtosecond time-resolved imaging of torsion in a chiral molecule," *J. Chem. Phys.*, vol. 136, p. 204310, May 2012.

[136] T. Yatsuhashi and N. Nakashima, "Multiple ionization and Coulomb explosion of molecules, molecular complexes, clusters and solid surfaces," *J. Photochem. Photobiol. C*, vol. 34, pp. 52–84, Mar. 2018.

[137] L. Keldysh, "Ionization in the field of a strong electromagnetic wave," *Soviet Physics JETP*, vol. 20, pp. 1307–1314, May 1965.

[138] V. R. Bhardwaj, P. B. Corkum, and D. M. Rayner, "Recollision during the high laser intensity ionization of c_{60}," *Phys. Rev. Lett.*, vol. 93, p. 043001, July 2004.

[139] A. T. J. B. Eppink and D. H. Parker, "Velocity map imaging of ions and electrons using electrostatic lenses: Application in photoelectron and photofragment ion imaging of molecular oxygen," *Rev. Sci. Instrum.*, vol. 68, no. 9, pp. 3477–3484, 1997.

[140] D. W. Chandler and P. L. Houston, "Two-dimensional imaging of state-selected photodissociation products detected by multiphoton ionization," *J. Chem. Phys.*, vol. 87, pp. 1445–1447, July 1987.

[141] L. Christensen, J. H. Nielsen, C. S. Slater, A. Lauer, M. Brouard, and H. Stapelfeldt, "Using laser-induced Coulomb explosion of aligned chiral molecules to determine their absolute configuration," *Phys. Rev. A*, vol. 92, p. 033411, Sept. 2015.

[142] L. Christensen, L. Christiansen, B. Shepperson, and H. Stapelfeldt, "Deconvoluting nonaxial recoil in Coulomb explosion measurements of molecular axis alignment," *Phys. Rev. A*, vol. 94, p. 023410, Aug. 2016.

[143] M. Burt, K. Amini, J. W. L. Lee, L. Christiansen, R. R. Johansen, Y. Kobayashi, J. D. Pickering, C. Vallance, M. Brouard, and H. Stapelfeldt, "Communication: Gas-phase structural isomer identification by coulomb explosion of aligned molecules," *J. Chem. Phys*, vol. 148, p. 091102, Mar. 2018.

[144] J. D. Pickering, K. Amini, M. Brouard, M. Burt, I. J. Bush, L. Christensen, A. Lauer, J. H. Nielsen, C. S. Slater, and H. Stapelfeldt, "Communication: Three-fold covariance imaging of laser-induced Coulomb explosions," *J. Chem. Phys.*, vol. 144, p. 161105, Apr. 2016.

[145] L. Frasinski, P. Hatherly, and K. Codling, "Multiphoton multiple ionisation of N_2O probed by three-dimensional covariance mapping," *Phys. Lett. A*, vol. 156, pp. 227–232, June 1991.

[146] O. Kornilov, M. Eckstein, M. Rosenblatt, C. P. Schulz, K. Motomura, A. Rouzée, J. Klei, L. Foucar, M. Siano, A. Lübcke, F. Schapper, P. Johnsson, D. M. P. Holland, T. Schlathölter, T. Marchenko, S. Düsterer, K. Ueda, M. J. J. Vrakking, and L. J. Frasinski, "Coulomb

explosion of diatomic molecules in intense XUV fields mapped by partial covariance," *J. Phys. B: At. Mol. Opt. Phys.*, vol. 46, p. 164028, Aug. 2013.

[147] L. J. Frasinski, "Covariance mapping techniques," *J. Phys. B: At. Mol. Opt. Phys.*, vol. 49, no. 15, p. 152004, 2016.

[148] J. Mikosch and S. Patchkovskii, "Coincidence and covariance data acquisition in photoelectron and -ion spectroscopy. I. Formal theory," *J. Mod. Opt.*, vol. 60, no. 17, pp. 1426–1438, 2013.

[149] J. Mikosch and S. Patchkovskii, "Coincidence and covariance data acquisition in photoelectron and -ion spectroscopy. II. Analysis and applications," *J. Mod. Opt.*, vol. 60, no. 17, pp. 1439–1451, 2013.

[150] W. J. Krzanowski, "Principles of multivariate analysis," ch. 7.1, New York: Oxford University Press, 1998.

[151] V. Zhaunerchyk, L. J. Frasinski, J. H. D. Eland, and R. Feifel, "Theory and simulations of covariance mapping in multiple dimensions for data analysis in high-event-rate experiments," *Phys. Rev. A.*, vol. 89, p. 053418, May 2014.

[152] L. J. Frasinski, K. Codling, and P. A. Hatherly, "Covariance Mapping: A Correlation Method Applied to Multiphoton Multiple Ionization," *Science*, vol. 246, pp. 1029–1031, Nov. 1989.

[153] R. Dörner, V. Mergel, O. Jagutzki, L. Spielberger, J. Ullrich, R. Moshammer, and H. Schmidt-Böcking, "Cold Target Recoil Ion Momentum Spectroscopy: a 'momentum microscope' to view atomic collision dynamics," *Phys. Rep.*, vol. 330, pp. 95–192, June 2000.

[154] J. D. Pickering, B. Shepperson, B. A. K. Hübschmann, F. Thorning, and H. Stapelfeldt, "Alignment and imaging of the CS_2 dimer inside helium nanodroplets," *Phys. Rev. Lett.*, vol. 120, p. 1121321, Mar. 2018.

[155] G. A. Garcia, L. Nahon, and I. Powis, "Two-dimensional charged particle image inversion using a polar basis function expansion," *Rev. Sci. Instrum.*, vol. 75, pp. 4989–4996, Nov. 2004.

[156] G. M. Roberts, J. L. Nixon, J. Lecointre, E. Wrede, and J. R. R. Verlet, "Toward real-time charged-particle image reconstruction using polar onion-peeling," *Review of Scientific Instruments*, vol. 80, p. 053104, May 2009.

[157] D. Dimitrovski, J. Maurer, H. Stapelfeldt, and L. B. Madsen, "Strong-field ionization of three-dimensionally aligned naphthalene molecules: orbital modification and imprints of orbital nodal planes," *J. Phys. B: At. Mol. Opt. Phys.*, vol. 48, no. 24, p. 245601, 2015.

[158] C. Smeenk, L. Arissian, A. Staudte, D. M. Villeneuve, and P. B. Corkum, "Momentum space tomographic imaging of photoelectrons," *J. Phys. B: At. Mol. Opt. Phys.*, vol. 42, p. 185402, Sept. 2009.

[159] C. R. Gebhardt, T. P. Rakitzis, P. C. Samartzis, V. Ladopoulos, and T. N. Kitsopoulos, "Slice imaging: A new approach to ion imaging and velocity mapping," *Rev. Sci. Instrum.*, vol. 72, pp. 3848–3853, Oct. 2001.

[160] K. Amini, S. Blake, M. Brouard, M. B. Burt, E. Halford, A. Lauer, C. S. Slater, J. W. L. Lee, and C. Vallance, "Three-dimensional imaging of carbonyl sulfide and ethyl iodide photodissociation using the pixel imaging mass spectrometry camera," *Review of Scientific Instruments*, vol. 86, p. 103113, Oct. 2015.

[161] B. J. Whitaker, *Imaging in Molecular Dynamics - Technology and Applications*. Cambridge University Press, 1 ed., 2003.

[162] B. Shepperson, A. S. Chatterley, A. A. Søndergaard, L. Christiansen, M. Lemeshko, and H. Stapelfeldt, "Strongly aligned molecules inside helium droplets in the near-adiabatic regime," *J. Chem. Phys.*, vol. 147, p. 013946, June 2017.

[163] A. A. Søndergaard, *Understanding Laser-Induced Alignment and Rotation of Molecules Embedded in Helium Nanodroplets*. Thesis, Aarhus University, Dec. 2016.

[164] T. Seideman, "On the dynamics of rotationally broad, spatially aligned wave packets," *J. Chem. Phys.*, vol. 115, pp. 5965–5973, Oct. 2001.

[165] R. G. A. Bone, "An investigation of the structure of weakly bound $(OCS)_2$," *Chem. Phys. Lett.*, vol. 206, Apr. 1993.

[166] K. Nauta and R. E. Miller, "Nonequilibrium Self-Assembly of Long Chains of Polar Molecules in Superfluid Helium," *Science*, vol. 283, p. 1895, Mar. 1999.

[167] National Institute of Standards and Technology, "Computational Chemistry Comparison and Benchmark DataBase."

[168] M. D. Esrafili and F. Mohammadian-Sabet, "Ab initio calculations of cooperativity effects on chalcogen bonding: Linear clusters of $(OCS)_{2-8}$ and $(OCSe)_{2-8}$," *Struct. Chem.*, vol. 26, pp. 199–206, Aug. 2014.

[169] A. S. Chatterley, C. Schouder, L. Christiansen, B. Shepperson, M. H. Rasmussen, and H. Stapelfeldt, "Long-lasting field-free alignment of large molecules inside helium nanodroplets," *ArXiv e-prints*, July 2018.

[170] J. Clayden, N. Greeves, S. Warren, and P. Wothers, *Organic Chemistry*. Oxford University Press, 1 ed., 2012.

[171] P. M. Zimmerman, F. Bell, D. Casanova, and M. Head-Gordon, "Mechanism for singlet fission in pentacene and tetracene: From single exciton of two triplets," *J. Am. Chem. Soc.*, vol. 133, pp. 19944–19952, Nov. 2011.

[172] M. Goulart, F. Zappa, A. M. Ellis, P. Bartl, S. Ralser, and S. P., "Electron ionization of helium droplets containing c_60 and alcohol clusters.," *Phys. Chem. Chem. Phys.*, vol. 19, p. 24197, July 2017.

[173] V. Mozhayskiy, M. N. Slipchenko, V. K. Adamchuk, and A. F. Vilesov, "Use of helium nanodroplets for assembly, transport, and surface deposition of large molecular and atomic clusters," *J. Chem. Phys.*, vol. 127, p. 094701, June 2007.

[174] G. W. Breton and X. Vang, "Photodimerization of anthracene," *J. Chem. Educ.*, vol. 75, p. 81, Jan. 1998.

[175] P. G. Frank, B. T. Tuten, A. Prasher, D. Chao, and E. B. Berda, "Intra-chain photodimerization of pendant anthracene units as an efficient route to single-chain nanoparticle fabrication," *Macromolecular Rapid Communications*, vol. 35, pp. 249–253, Oct. 2013.

[176] T. Chakraborty and E. C. Lim, "Study of van der waals clusters of anthracene by laser-induced fluorescence in a supersonic jet: evidence for two structurally different dimers," *J. Phys. Chem.*, vol. 97, pp. 11151–11153, Oct. 1993.

[177] T. Matsuoka, K. Kosugi, K. Hino, M. Nishiguchi, K. Ohashi, N. Nishi, and H. Sekiya, "Electronic spectra of jet-cooled anthracene dimer: Evidence of two isomers in the electronic ground state," *J. Phys. Chem. A*, vol. 102, pp. 7598–7602, Sept. 1998.

[178] F. Piuzzi, I. Dimicoli, M. Mons, P. Millie, V. Brenner, Q. Zhao, B. Soep, and A. Tramer, "Spectroscopy, dynamics and structures of jet formed anthracene clusters," *Chem. Phys.*, vol. 275, pp. 123–147, July 2001.

[179] A. S. Chatterley, E. T. Karamatskos, C. Schouder, L. Christiansen, A. V. Jørgensen, T. Mullins, J. Küpper, and H. Stapelfeldt, "Communication: Switched wave packets with spectrally truncated chirped pulses," *J. Chem. Phys*, vol. 148, p. 221105, June 2018.

[180] R. Johansen, *Generation of Few-Cycle, Mid Infrared Laser Pulses: Ionization of aligned and Oriented Molecules.* PhD thesis, Aug. 2016.

[181] M. Tanaka, M. Kawaji, T. Yatsuhashi, and N. Nakashima, "Ionization and fragmentation of alkylphenols by 0.8-1.5μm femtosecond laser pulses," *J. Phys. Chem. A*, vol. 113, pp. 12056–12062, Sept. 2009.

[182] Z.-A. Huang, C. Chen, X.-D. Yang, X.-B. Fan, W. Zhou, C.-H. Tung, L.-Z. Wu, and H. Cong, "Synthesis of oligoparaphenylene-derived nanohoops employing an anthracene photodimerization-cycloreversion strategy," *J. Am. Chem. Soc.*, vol. 138, pp. 11144–11147, Aug. 2016.

[183] Y. Zheng, M. Micic, S. V. Mello, M. Mabrouki, F. M. Andreopoulos, V. Konka, S. M. Pham, and R. M. Leblanc, "Peg-based hydrogel synthesis via the photodimerization of anthracene groups," *Macromolecules*, vol. 35, pp. 5228–5234, May 2002.

[184] J. O. Johansson, E. Bohl, and E. E. B. Campbell, "Super-atom molecular orbital excited states of fullerenes," *Philos. Trans. A Math. Phys. Eng. Sci.*, vol. 374, p. 2076, Sept. 2016.